

Polarization manipulation in femtosecond laser direct written waveguides in fused silica



Dissertation
zur Erlangung des akademischen Grades
doctor rerum naturalium (Dr. rer. nat)

vorgelegt dem Rat der Physikalisch-Astronomischen Fakultät
der Friedrich-Schiller-Universität Jena

von M. Sc. Kim Alina Lammers
geboren am 01. Dezember 1994 in Düsseldorf

Gutachter:

1. : Prof. Dr. Stefan Nolte (Friedrich-Schiller-Universität Jena)
2. : Prof. Dr. Uwe Morgner (Leibniz Universität Hannover)
3. : Prof. Dr. Robert R. Thomson (Heriot-Watt University Edinburgh)

Tag der Disputation: 18. Januar 2022, Jena

Dedication

To my beloved husband, my parents and my family. You mean the world to me.

Contents

Chapter 1. Introduction	3
Chapter 2. Fundamentals	5
2.1. Polarization	5
2.2. Optical dielectric waveguides	13
2.3. Volume modifications in transparent dielectric materials by means of ultrashort laser pulses	15
2.4. Optical quantum computing	21
2.5. Liquid crystals	24
2.6. State of the art	30
Chapter 3. Experimental Setups	34
3.1. The writing setup	34
3.2. The characterization setup	35
Chapter 4. Femtosecond Laser Direct Written Waveguides	38
4.1. Loss measurements	38
4.2. Waveguide writing using a Gaussian beam	39
4.3. Waveguide writing with elliptically shaped beams	42
4.4. Suitable parameters for writing waveguides with a cylindrical Galilean telescope	47
4.5. Improved waveguide performance using an anamorphic zoom system	51
Chapter 5. Polarization Control Based on Nanogratings	54
5.1. Scanning electron microscope images of modifications	54
5.2. Parameter dependencies	56
5.3. Single qubit quantum gates made of nanogratings	67
5.4. Novel beam shapes for nanograting inscription	76
Chapter 6. Adaptive Polarization Control Using Liquid Crystals	86
6.1. Sample preparation and waveguide inscription	86
6.2. Electro-optical modulation of the output polarization	88
Chapter 7. Conclusion and Outlook	95
Bibliography	99

Zusammenfassung	110
Ehrenwörtliche Erklärung	112
List of publications and conference contributions	114
Acknowledgements	115

CHAPTER 1

Introduction

The information age has fundamentally changed our world. Information technology has become such an indispensable part of our lives that many people would not leave their home without their cell phone or smartphone. The further advancement of novel technologies for data transmission, acquisition, and processing is considered essential for social and economical progress.

To improve and expand our capability of information processing, new technologies have to be developed. One interesting approach is to replace or expand existing electrical devices with devices that use optical signals as information carriers, ultimately leading to a photonic computer that performs all calculations optically. Optical data transmission yields many benefits over electronic data transmission, like enabling higher bandwidths or the ability of light beams to travel through one another without affecting each others properties [1]. Additionally, since single photons can be used to encode quantum information, quantum computing at room temperature could be possible on a photonic computer [2]. A first milestone in this direction has recently been achieved by demonstrating quantum computational advantage using photons [3]. For reasons of practicability, a photonic computer should be based on integrated optics, not on free beam optics [4]. Integrated photonic circuits offer better performance compared to bulk optical setups in terms of stability and compactness of the structures. Furthermore, when integrated circuits are fabricated from transparent materials, it becomes possible to embed sensing functionalities and signal processing into displays [5], windshields [6], or augmented reality headsets [7]. Various techniques to fabricate integrated photonic circuits have been established so far. In this thesis, the focus will be on circuits created by femtosecond laser direct writing (FLDW) in fused silica, which is a technique that enables rapid, on-demand prototyping of complex three-dimensional integrated photonic devices in a single step procedure [8].

To achieve the highest possible data rate when transmitting information with light, the data must be encoded into as many degrees of freedom of the photon as possible [9]. These degrees of freedom are, for example, the path of the photon or also the polarization. The path of a photon is easily manipulated in integrated platforms using waveguides that determine the direction of the light. This thesis will

focus on the second degree of freedom mentioned, namely polarization. The goal of this work is to demonstrate novel methods for introducing polarization control in FLDW integrated photonic circuits. This is done in two steps. In the first step, the fabrication of fused silica waveguides with low birefringence and minimal losses must be mastered. The task of these waveguides is to transmit light while maintaining its polarization state. In the second step, the possibility of using compact, birefringent structures to achieve a targeted polarization change is demonstrated. Two approaches are pursued. One is to induce this polarization change by so-called nanogratings. This is a type of modification that can be produced by FLDW. The other is to embed liquid crystals in waveguides as switchable polarization-modifying elements. Both approaches have their own advantages and disadvantages, which will be discussed.

This thesis is divided into seven chapters, starting with this introduction. Chapter 2 (“fundamentals”) covers the basics needed to understand the material in this thesis, including a description of the polarization of light, the process of modifying the volume of transparent materials that then enables FLDW, the properties of laser induced modifications in fused silica that are relevant to this thesis, a brief introduction to quantum computing, and finally an overview of the properties that liquid crystals exhibit. The chapter concludes with an overview of the state of the art. In chapter 3 (“Experimental Setups”), the setups used to create and characterize structures are presented. The method how to determine the polarization dependent properties of a studied modification from the characterization data is derived. Chapter 4 (“Femtosecond Laser Direct Written Waveguides”) describes the steps taken to realize waveguides with minimal birefringence at maximum transmission. Different beam shaping options are explored and their influence on waveguide formation are discussed. In chapter 5 (“Polarization Control Based on Nanogratings”), the formation of nanogratings under different writing conditions is investigated. The possibility of varying the properties of this type of modification by the laser parameters is demonstrated, in particular the orientation and strength of the birefringence. By combining nanogratings with the waveguides from the previous chapter, integrated waveplates are created, that find application as quantum gates. For further improvements, a new beam shaping technique with conical phase fronts is also presented, and its influence on the nanogratings is described. In chapter 6 (“Adaptive Polarization Control Using Liquid Crystals”), the ability to use liquid crystals as tuneable waveplates is demonstrated. Evidence for electro-optical modulation is given. Finally, the results are summarized and discussed in the conclusion.

CHAPTER 2

Fundamentals

In this chapter the basic physical concepts required to understand this thesis are revised and summarized. The chapter will cover the fundamentals of polarization, followed by a recap of waveguide basics, an overview on the current state of knowledge in the femtosecond laser direct writing field, and a review of the fundamentals on optical quantum computing. Finally, the state of the art of the research most relevant to this thesis will be presented.

2.1. Polarization

Since polarization is a degree of freedom of photons that can be used to encode quantum information, it is important to understand this light property in depth. To do so, this section will focus on the classical description of polarization. Light is referred to as polarized when its field vector \vec{E} oscillates in a clearly defined direction with respect to the wave vector \vec{k} . The direction of polarization is given by the direction of \vec{E} . There are several so-called states of polarization that light can have, i.e., linearly polarized light, when \vec{E} oscillates in a fixed direction and only the magnitude changes, or circular polarized light, when the magnitude of \vec{E} stays constant, but the direction rotates at a constant rate with time. The most general polarization state is elliptical polarization, when both amplitude and direction of \vec{E} change over time [10]. The polarization state can change, for example, if light passes through a birefringent or dichroic medium. The following subsections will summarize the material properties related to polarization change, as well as the mathematical framework used to describe and compute polarization.

2.1.1. Birefringence. If the speed of light in a homogeneous medium is dependent on the propagation direction and the polarization plane of the light, this medium is called optically anisotropic, also known as birefringent [11]. Birefringence is usually characterized in terms of a refractive index difference Δn for two polarization components. This refractive index difference will lead to an optical path difference *OPD* between the polarization components along the propagation direction (here denoted as x -coordinate), which is given by the integral

$$OPD = \int \Delta n(x) dx. \quad (2.1)$$

2.1. POLARIZATION

The according phase difference δ of the polarization components on the other hand can be calculated by

$$\delta = \frac{2\pi \cdot OPD}{\lambda}, \quad (2.2)$$

where λ denotes the wavelength of the light. The optical path difference will be used frequently in this thesis to quantify the retardation effect of a structure. In the following subsections the cause for birefringence will be explained first on a molecular level for dielectrics and then for gratings.

2.1.1.1. *Birefringence of dielectric media.* An electric field \vec{E} exerts a force \vec{F} on a charge q given by [12]

$$\vec{F} = \vec{E} \cdot q. \quad (2.3)$$

Assuming that an external electric field \vec{E}_{ext} of limited strength (i.e., $|\vec{E}_{ext}|$ smaller than 1×10^5 V/cm [12]), for example, in the form of an electromagnetic wave, is applied to a medium, the medium will react by moving its charges according to that force. In conductive materials, the charge carriers will move to the surface, creating their own electric field, until that electric field is strong enough to compensate for the external field. The resulting internal electric field is zero. This is known as electrostatic induction. In insulators (i.e., dielectrics), however, the charge carriers are bound to the molecules. Therefore, each molecule will reorientate its charge carriers within the field. Hereby, each molecule turns into a dipole. The dipole moment \vec{p} of each of these dipoles is proportional to the applied electric field, with the proportionality constant given by the molecule's characteristic polarizability tensor $\overline{\alpha}_p$ [12]:

$$\vec{p} = \overline{\alpha}_p \vec{E}_{ext}. \quad (2.4)$$

The resulting electric field inside the dielectric will be given by $\vec{E}_{in} = (\mathbf{1} - \overline{\epsilon}_r^{-1}) \vec{E}_{ext}$, with $\overline{\epsilon}_r$ being the material specific relative dielectric constant. It can be expressed in terms of polarizability, the dielectricity constant ϵ_0 and the number N of induced dipoles as [12]

$$\overline{\epsilon}_r = \mathbf{1} + N \overline{\alpha}_p / \epsilon_0. \quad (2.5)$$

The polarizability of a material can be interpreted as a measure of how far the positive and negative charges in the molecule can be separated. For the simplified case of non-magnetic, homogeneous materials (magnetic permeability of the material $\mu_r = 1$) the polarizability is connected to the refractive index \overline{n} via

$$\overline{n}^2 = \overline{\epsilon}_r = \mathbf{1} + N \overline{\alpha}_p / \epsilon_0. \quad (2.6)$$

Hereby it can be seen, that if the polarizability changes with the direction (i.e., electrical anisotropy [13]), also the refractive index of the material will be directional dependant, so the material will be birefringent [12]. The directional dependency of polarizability can have various causes, for example, external fields (such as the Pockels effect [14], the Kerr effect [15] or Cotton-Mouton effect [16]), the arrangement of atoms in the medium (like in birefringent crystals) or strain [11].

2.1.1.2. *Birefringence of one-dimensional dielectric subwavelength gratings.* One-dimensional subwavelength gratings are structures where the refractive index is modulated in one direction at a period Λ which is smaller than the wavelength of light λ interacting with it. These structures typically exhibit form birefringence. For sufficiently small grating periods ($\lambda \gg \Lambda$) and sufficiently large grating depths d ($\lambda \ll d$), the macroscopic optical properties of the grating can be described using effective-medium theory of the zeroth-order grating problem [17]. Here, a grating consisting of alternating homogeneous dielectric slabs with scalar refractive indices n_1 and n_2 is assumed. The dielectric constants $\epsilon_{r1/r2}$ of these slabs are given by $n_{1/2} = \sqrt{\epsilon_{r1/r2}}$. The thickness of the slabs of refractive index n_1 shall be t_1 , and the thickness of the slabs with refractive index n_2 will therefore be $t_2 = \Lambda - t_1$. From this, the filling factors of the grating can be defined as $f_1 = t_1/\Lambda$ and $f_2 = t_2/\Lambda$, respectively.

Monochromatic light of wavelength λ hits this grating with the electric field vector parallel to the slabs, as sketched in figure 2.1.

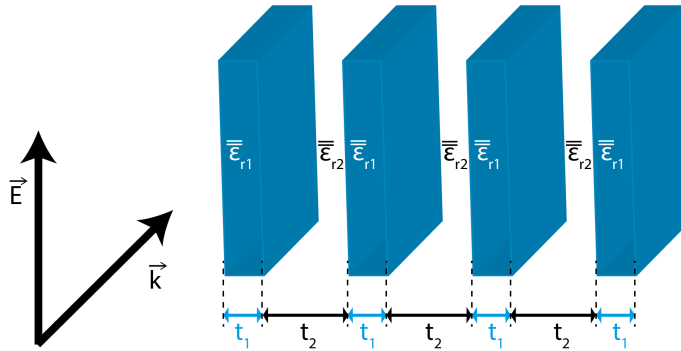


FIGURE 2.1. Schematic sketch of the one-dimensional dielectric subwavelength grating when light polarized parallel to the grating slabs hits the grating.

In this case the electric field only has a component that is tangential and which must be continuous across the grating bars, so its value is the same for both the slabs with refractive indices n_1 and n_2 . The electric displacement $\vec{D}_{1/2}$ in each of the regions is then given by $\vec{D}_{1/2} = \epsilon_{r1/r2}\vec{E}$. When averaging this displacement over the whole

2.1. POLARIZATION

grating

$$\vec{D}_{avg} = \frac{\vec{D}_1 \cdot t_1 + \vec{D}_2 \cdot t_2}{t_1 + t_2} = \vec{E} \cdot \frac{\epsilon_{r1} \cdot t_1 + \epsilon_{r2} \cdot t_2}{\Lambda}, \quad (2.7)$$

an average dielectric constant ϵ_{\parallel} can be computed as [18]:

$$\epsilon_{\parallel} = \frac{|\vec{D}_{avg}|}{|\vec{E}|} = (\epsilon_{r1} \cdot t_1 + \epsilon_{r2} \cdot t_2)/\Lambda. = f_1 \epsilon_{r1} + f_2 \epsilon_{r2}. \quad (2.8)$$

Next, consider the case of monochromatic light of wavelength λ hitting this grating with an electric field vector orthogonal to the slabs, as sketched in figure 2.2.

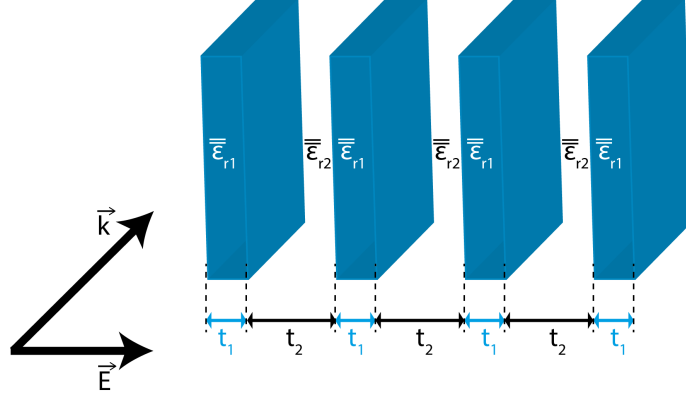


FIGURE 2.2. Schematic sketch of the one-dimensional dielectric subwavelength grating when light polarized perpendicular to the grating slabs hits the grating.

Since the normal component of the electric displacement is always continuous across an interface in the absence of surface charges, the electric fields $\vec{E}_{1/2}$ in the different materials of the grating are given by $\vec{E}_{1/2} = \vec{D}/\epsilon_{r1/r2}$. The averaged dielectric constant ϵ_{\perp} for this case is [18]:

$$\epsilon_{\perp} = \frac{|\vec{D}|\Lambda}{|\vec{E}_1|t_2 + |\vec{E}_2|t_1} = \frac{\epsilon_{r1}\epsilon_{r2}\Lambda}{\epsilon_{r1} \cdot t_2 + \epsilon_{r2} \cdot t_1} = \frac{\epsilon_{r1}\epsilon_{r2}}{f_2\epsilon_{r1} + f_1\epsilon_{r2}}. \quad (2.9)$$

Since the refractive index is related to the dielectric constant, the existence of two different dielectric constants means the existence of optical anisotropy, i.e., birefringence. From the above equations a resulting birefringence Δn can be calculated as follows:

$$\Delta n = |\sqrt{\epsilon_{\perp}} - \sqrt{\epsilon_{\parallel}}|. \quad (2.10)$$

2.1.2. Dichroism. Dichroism, also known as diattenuation, refers to the property of a medium to transmit more of one polarization state compared to

the orthogonal one. The term dichroism (literally meaning “two colours”) originally comes from crystals that appear to change colour when viewed under light of different polarization orientations [10]. This effect can be understood in similar ways to the above discussed birefringence, i.e., by considering equation (2.5) and assuming $\bar{\epsilon}_r$ to be complex. This way, also the complex value of the refractive index will be anisotropic, giving rise to polarization dependant absorption. Let us consider light of the polarization state that has minimal losses to pass through a dichroic medium. The transmission value will be maximal in this case, and it shall be called T_{max} . The transmission for light of the orthogonal polarization on the other hand will be minimal and shall be named T_{min} , making the average transmission

$$T_{ave} = \frac{T_{max} + T_{min}}{2}, \quad (2.11)$$

and the transmission difference

$$\Delta T = T_{max} - T_{min}. \quad (2.12)$$

The dichroism D of the sample under test is then typically quantified by [19]

$$D = \frac{T_{max} - T_{min}}{T_{max} + T_{min}} = \frac{\Delta T}{2T_{ave}}. \quad (2.13)$$

2.1.3. Matrix Methods for Polarization Computations. A convenient way to calculate the change of polarization state caused by birefringent and/or dichroic media is using the so-called Jones calculus, developed by Robert Clark Jones from 1941 to 1956 [20–27], which will be introduced in this subsection. This calculus uses 2×1 vectors known as Jones vectors to represent the polarization of light via its field components. Additionally, it uses 2×2 matrices, so-called Jones matrices, to describe the change of polarization when light passes through an optical element. The calculus mathematically corresponds to the representation of qubits in quantum optical systems. However, it was developed for classical light and can only be applied when the degree of polarization is 1. The normalized representation of horizontal light \vec{H} in this framework is

$$\vec{H} = \begin{pmatrix} 1 \\ 0 \end{pmatrix}, \quad (2.14)$$

2.1. POLARIZATION

while of vertical light \vec{V} is

$$\vec{V} = \begin{pmatrix} 0 \\ 1 \end{pmatrix}, \quad (2.15)$$

and any other polarization state is a superposition of the two, for example, right circularly polarized light \vec{R}_C is

$$\vec{R}_C = \frac{1}{\sqrt{2}} \left[\begin{pmatrix} 1 \\ 0 \end{pmatrix} - i \begin{pmatrix} 0 \\ 1 \end{pmatrix} \right] = \frac{1}{\sqrt{2}} \begin{pmatrix} 1 \\ -i \end{pmatrix} \quad (2.16)$$

and antidiagonally polarized light \vec{A} is

$$\vec{A} = \frac{1}{\sqrt{2}} \left[\begin{pmatrix} 1 \\ 0 \end{pmatrix} - \begin{pmatrix} 0 \\ 1 \end{pmatrix} \right] = \frac{1}{\sqrt{2}} \begin{pmatrix} 1 \\ -1 \end{pmatrix}. \quad (2.17)$$

To change the state of this polarization, for example, when going through an optical element like a waveplate, the optical element's matrix $\overset{\leftrightarrow}{J}$ must be multiplied to the original Jones vector \vec{v} representing the initial polarization state. The resulting Jones vector \vec{v}' describing the final polarization state can be obtained by $\vec{v}' = \overset{\leftrightarrow}{J}\vec{v}$. For instance, the Jones matrix of a phase shifter $\overset{\leftrightarrow}{J}_{ph}$ with a phase retardation between fast and slow axis of η and the fast axes in direction of the horizontal axis is defined as [28]

$$\overset{\leftrightarrow}{J}_{ph}(\eta) = \begin{pmatrix} e^{i\eta/2} & 0 \\ 0 & e^{-i\eta/2} \end{pmatrix}. \quad (2.18)$$

To describe the rotation of an optical element by the angle θ , the rotational transformation using the rotational matrix $\overset{\leftrightarrow}{R}$ is applied. The rotational matrix is defined as:

$$\overset{\leftrightarrow}{R}(\theta) = \begin{pmatrix} \cos \theta & \sin \theta \\ -\sin \theta & \cos \theta \end{pmatrix}. \quad (2.19)$$

A rotated element, for example, a phase retarder rotated by θ , is obtained via

$$\overset{\leftrightarrow}{J}'_{ph}(\eta, \theta) = \overset{\leftrightarrow}{R}(-\theta) \overset{\leftrightarrow}{J}_{ph}(\eta) \overset{\leftrightarrow}{R}(\theta) \quad (2.20)$$

The matrix of a dichroic element $\overset{\leftrightarrow}{J}_{dichroic}$ with maximal transmission T_{max} for horizontally polarized light and minimal transmission T_{min} for vertically polarized

light is

$$\vec{J}_{dichroic}^{\leftrightarrow} = \begin{pmatrix} T_{max} & 0 \\ 0 & T_{min} \end{pmatrix}. \quad (2.21)$$

A different option of representing polarization states is through the Mueller-Stokes matrix calculus. In this mathematical framework, polarization states are represented in terms of 4-dimensional vectors, so-called Stokes vectors [29]. The Stokes vector has four entries (S_0, S_1, S_2 and S_3), known as the Stokes parameters. S_0 corresponds to the intensity of the light. In many applications, normalized Stokes parameters are used, which means all Stokes parameters are divided by the intensity of the light, leading to S_0 always amounting to unity. A list of examples for common normalized Stokes vectors is given in table 2.1.

TABLE 2.1. Some typical Stokes vectors.

Vertically polarized:	$\begin{pmatrix} 1 \\ -1 \\ 0 \\ 0 \end{pmatrix}$		Horizontally polarized:	$\begin{pmatrix} 1 \\ 1 \\ 0 \\ 0 \end{pmatrix}$
Anti-diagonally polarized:	$\begin{pmatrix} 1 \\ 0 \\ -1 \\ 0 \end{pmatrix}$		Diagonally polarized:	$\begin{pmatrix} 1 \\ 0 \\ 1 \\ 0 \end{pmatrix}$
Left-circularly polarized:	$\begin{pmatrix} 1 \\ 0 \\ 0 \\ -1 \end{pmatrix}$		Right-circularly polarized:	$\begin{pmatrix} 1 \\ 0 \\ 0 \\ 1 \end{pmatrix}$

S_1, S_2 and S_3 form coordinates of a position P on or inside the so-called Poincaré sphere (see fig. 2.3) [30, 31]. This sphere is centered around the origin of its coordinate system and represents all possible polarization states of fully polarized light, while the origin of the coordinate system corresponds to unpolarized light. The radius of the sphere corresponds to S_0 , so when representing normalized Stokes vectors, the radius of the sphere is 1. The coordinate system in which the Poincaré sphere is positioned has three axes. The abscissa ranges from purely vertically polarized light V to purely horizontally polarized light H , its coordinate is the Stokes parameter S_1 . The ordinate ranges from purely anti-diagonally polarized light A to purely diagonally polarized light D and its coordinate is the Stokes parameter S_2 . The applicate ranges from purely left circular polarized light L to purely right circular

2.1. POLARIZATION

polarized light R and its coordinate is the Stokes parameter S_3 . Two opposing points on the Poincaré sphere correspond to orthogonal polarization states. The distance of P to the origin of the sphere yields the degree of polarization.

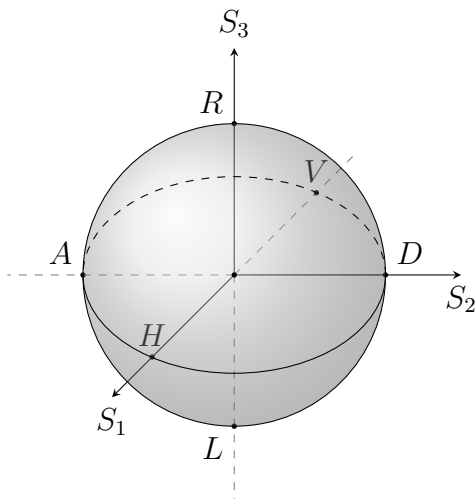


FIGURE 2.3. Poincaré sphere.

The influence of optical elements on the polarization of light is represented via 4 x 4 Mueller matrices. The change of a Stokes vector is performed by multiplication with such a matrix. Examples of some important Mueller matrices for this work are listed in table 2.2. The list includes matrices for polarizers, linear retarders, linear diattenuators and neutral density filters. Since the commutator of the matrix for a linear retarder and the matrix for a linear diattenuator is zero, these two can be multiplied together to account for polarization dependent losses in the linear diattenuating retarder. The resulting matrix is also listed in table 2.2. All matrices in that table are given for a fixed orientation of the optical element. To rotate an element by a given angle θ the rotational matrix $\overset{\leftrightarrow}{R}(\theta)$ must be introduced:

$$\overset{\leftrightarrow}{R}(\theta) = \begin{pmatrix} 1 & 0 & 0 & 0 \\ 0 & \cos(2\theta) & -\sin(2\theta) & 0 \\ 0 & \sin(2\theta) & \cos(2\theta) & 0 \\ 0 & 0 & 0 & 1 \end{pmatrix} \quad (2.22)$$

The Mueller matrix $\overset{\leftrightarrow}{M}'(\theta)$ of the rotated element with unrotated matrix $\overset{\leftrightarrow}{M}$ is then given by [19]

$$\overset{\leftrightarrow}{M}'(\theta) = \overset{\leftrightarrow}{R}(\theta)\overset{\leftrightarrow}{M}\overset{\leftrightarrow}{R}(-\theta). \quad (2.23)$$

TABLE 2.2. Selected Mueller matrices [19]. Diattenuation denotations correspond to the definitions given in section 2.1.2.

Polarizer transmitting vertically polarized light	$\frac{1}{2} \begin{pmatrix} 1 & -1 & 0 & 0 \\ -1 & 1 & 0 & 0 \\ 0 & 0 & 0 & 0 \\ 0 & 0 & 0 & 0 \end{pmatrix}$
Linear retarder with retardance δ and fast axis at 0° to horizontal axis	$\begin{pmatrix} 1 & 0 & 0 & 0 \\ 0 & 1 & 0 & 0 \\ 0 & 0 & \cos(\delta) & \sin(\delta) \\ 0 & 0 & -\sin(\delta) & \cos(\delta) \end{pmatrix}$
Linear diattenuator with maximal transmission for horizontally polarized light	$\begin{pmatrix} T_{ave} & \frac{\Delta T}{2} & 0 & 0 \\ \frac{\Delta T}{2} & T_{ave} & 0 & 0 \\ 0 & 0 & \sqrt{T_{max}T_{min}} & 0 \\ 0 & 0 & 0 & \sqrt{T_{max}T_{min}} \end{pmatrix}$
Neutral density filter with transmission T [32]	$\begin{pmatrix} T & 0 & 0 & 0 \\ 0 & T & 0 & 0 \\ 0 & 0 & T & 0 \\ 0 & 0 & 0 & T \end{pmatrix}$
Linear diattenuating retarder with retardation δ and both maximal transmission and optical axis at 0°	$\begin{pmatrix} T_{ave} & \frac{\Delta T}{2} & 0 & 0 \\ \frac{\Delta T}{2} & T_{ave} & 0 & 0 \\ 0 & 0 & \sqrt{T_{max}T_{min}} \cos(\delta) & \sqrt{T_{max}T_{min}} \sin(\delta) \\ 0 & 0 & -\sqrt{T_{max}T_{min}} \sin(\delta) & \sqrt{T_{max}T_{min}} \cos(\delta) \end{pmatrix}$

A Jones matrix $\overset{\leftrightarrow}{J}$ can be converted into a Mueller matrix $\overset{\leftrightarrow}{M}$ via

$$\overset{\leftrightarrow}{M} = \overset{\leftrightarrow}{A} (\overset{\leftrightarrow}{J} \otimes \overset{\leftrightarrow}{J}^*) \overset{\leftrightarrow}{A}. \quad (2.24)$$

Here, the asterisk is used to denote the complex conjugate, \otimes denotes the tensor product and matrix $\overset{\leftrightarrow}{A}$ is given by [33]

$$\overset{\leftrightarrow}{A} = \begin{pmatrix} 1 & 0 & 0 & 1 \\ 1 & 0 & 0 & -1 \\ 0 & 1 & 1 & 0 \\ 0 & i & -i & 0 \end{pmatrix}. \quad (2.25)$$

2.2. Optical dielectric waveguides

Optical waveguides are structures with a refractive index profile that confines the propagation of light to a specific region, thereby allowing a controlled transport of light [34]. Waveguides are used in optical circuits to connect different optical devices, analogously to wires in an electronic circuit [4]. Different types of waveguides exist, varying in geometry and material. The waveguides that are used in this thesis are non-planar, dielectric waveguides with graded refractive index profiles. This means

2.2. OPTICAL DIELECTRIC WAVEGUIDES

that in a Cartesian coordinate system, assuming a propagation direction x , the refractive index of the waveguide is a gradually varying function of both y and z in the core of the waveguide, and a constant value in the surrounding cladding. The refractive index may therefore be written as $n(y, z) = n_0 + \Delta n_{core}(y, z)$, with the maximum value of $n(y, z)$ being n_{max} . The propagation of light in the waveguide is governed by the wave equation. If the relative variation of the refractive index is sufficiently small, the wave equation can be written in scalar approximation as [35]

$$\frac{\partial^2 E(x, y, z)}{\partial x^2} + \frac{\partial^2 E(x, y, z)}{\partial y^2} + \frac{\partial^2 E(x, y, z)}{\partial z^2} + k^2 n^2(y, z) E(x, y, z) = 0. \quad (2.26)$$

Here, $E(x, y, z)$ is the electric field and k denotes the wave number of the transmitted light. Using the ansatz

$$E(x, y, z) = E_0(y, z) \exp(i\beta x), \quad (2.27)$$

this equation can be simplified to [36]

$$\frac{\partial^2 E(x, y, z)}{\partial y^2} + \frac{\partial^2 E(x, y, z)}{\partial z^2} + (k^2 n^2(y, z) - \beta^2) E(x, y, z) = 0. \quad (2.28)$$

In this equation, the eigenvalue β is known as the propagation constant. The solutions of the wave equation are the modes of the waveguide. There are radiative and guided modes, which are classified depending on the value of β/k . For the continuous spectrum of $\beta/k < n_0$, the modes are radiative modes, which oscillate outside of the waveguide's core. For a finite number of eigenvalues which fulfill $n_0 < \beta/k < n_{max}$, the according eigenfunctions are guided modes, which have evanescent tails outside of the waveguide's core [37]. A waveguide will be referred to as multi-mode, single-mode or not guiding at a certain wavelength, depending on the number of guided modes existing for that wavelength. The largest wavelength for which a mode is guided is referred to as the cut-off wavelength. Therefore, the spectrum in which single-mode operation of a waveguide is possible, is framed on the one end by the cut-off wavelength of the fundamental mode, and on the other end by the cut-off wavelength of the next higher mode. When light with an electric field $E_{in}(x, y, z)$ is launched into a waveguide at the waveguides input facet (position $x = x_0$), it will be distributed between the modes of that waveguide. The amount of power, that is launched into each guided mode $E_{mode}(y, z)$ can be calculated using

the overlap integral, defined as [38]

$$\eta = \frac{|\int \int_{-\infty}^{\infty} E_{in}(x_0, y, z) * E_{mode}(y, z) dy dz|^2}{\int \int_{-\infty}^{\infty} |E_{in}(x_0, y, z)|^2 dy dz \int \int_{-\infty}^{\infty} |E_{mode}(y, z)|^2 dy dz}. \quad (2.29)$$

Light which does not resemble any of the guided mode fields will excite radiation modes, dissipating away [39].

2.3. Volume modifications in transparent dielectric materials by means of ultrashort laser pulses

Inducing modifications in the volume of transparent dielectric materials by means of ultrashort laser pulse irradiation is fundamental to the creation of structures used in this thesis. Generally, this process is separated into three steps that may overlap in time. These three steps are firstly the excitation of the electrons, secondly the relaxation of the electrons, and finally the deposition of energy in the atomic lattice, enabling the creation of permanent structural changes [40–42]. A sketch of the process is given in figure 2.4. The three stages will be explained in detail in the following.

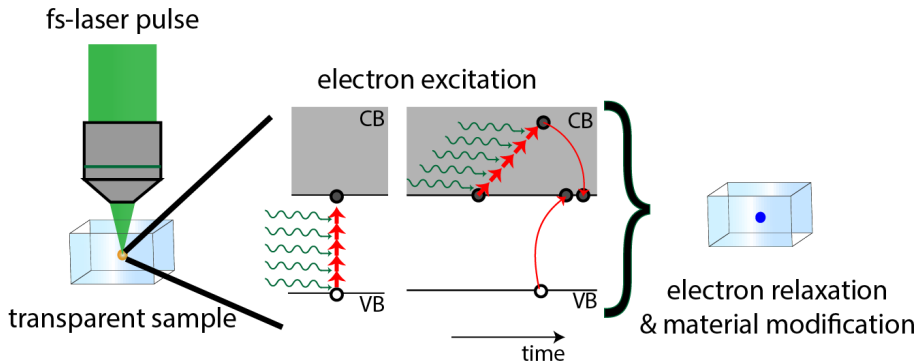


FIGURE 2.4. Sketch of the processes leading to material modifications in transparent dielectric materials like fused silica. CB stands for conduction band, VB stands for valence band. Figure is in the style of [42].

2.3.1. Physical mechanisms leading to volume modifications. According to the band model, in dielectrics the highest occupied electron energy band (also referred to as valence band) and the next higher possible energy state an electron can occupy, are separated by a significant energy difference, known as the band gap [43]. This band gap has to be bridged, if an electron is to be excited, i.e., by the irradiation of a laser. Should the photon energy be large enough, this can be achieved using linear absorption. For the material used in this thesis (fused silica, bandgap of 9.0 eV [44]), and the photon energy of the laser used to modify the material (515 nm

2.3. VOLUME MODIFICATIONS IN TRANSPARENT DIELECTRIC MATERIALS BY MEANS OF ULTRASHORT LASER PULSES

wavelength, corresponding to 2.4 eV photon energy), this is not the case. Therefore, nonlinear absorption processes are required to excite the electrons. The probability of these processes increases with the intensity I of the laser light [45]. One type of nonlinear absorption is the so-called tunneling ionization [46]. This absorption mechanism is characterized by an overlap of the Coulomb field of the atomic nucleus with the electric field of the laser, causing a deformation of the potential wall that holds the electrons in place. This deformation enables electrons to tunnel out of the potential barrier. An alternative nonlinear absorption process is the multiphoton absorption [46], where so many photons are simultaneously absorbed that the sum of their energies surpasses the bandgap of the material.

Which ionization type dominates the nonlinear absorption process, is given by the Keldysh parameter γ , defined as [47]

$$\gamma = \omega t_p = \omega \frac{\sqrt{2m_e I_p}}{eE}. \quad (2.30)$$

Here, t_p denotes the time an electron needs to tunnel through its potential barrier, ω is the angular frequency of the laser, I_p is the ionization-potential, m_e and e denote the electron's charge and mass, respectively, and E is the electric field. If $\gamma \ll 1$, tunneling ionization dominates, whilst if $\gamma \gg 1$, multiphoton ionization dominates, which is often the case for material processing with dielectrics [48].

All electrons that have entered the conduction band can linearly absorb further incoming photons, moving to higher energy states. When these electrons thereby have absorbed sufficient energy, the electron may raise other electrons to the conduction band via impact ionization. The number of electrons may then increase exponentially, since each new electron in the conduction band can excite further electrons, giving rise to so-called avalanche ionization. An electron plasma is formed, which is locally confined to the focal area of the irradiation laser, and which consists of an accumulation of freely movable, excited electrons in a lattice of positively charged atomic nuclei [48]. The change with time t of the free electron density n_e can be modelled by [49]

$$\frac{dn_e}{dt} = \alpha I(t)n_e(t) + \sigma_k I(t)^k. \quad (2.31)$$

The parameter α in this equation is called avalanche coefficient and is used to scale the influence avalanche ionization has on the process. The parameter σ_k is the k -photon absorption cross section of the multiphoton absorption. During the presence of the femtosecond-laser pulse, the electrons do not have the time to couple to the atomic lattice [50], so all energy is absorbed by the electrons only.

When no further energy is deposited into the electron plasma, the electrons then start to relax. Excess energy of the relaxing electrons can be deposited into the atomic lattice by means of a shockwave, and by heating the atomic lattice [45]. Phase transitions may occur within the material due to the deposited heat, which cause permanent structural changes in the form of material modifications and defects.

2.3.2. Femtosecond laser direct writing technique. The method used to fabricate light-guiding structures in this thesis is the so-called femtosecond laser direct writing technique, which uses volume modifications that are created as explained in section 2.3.1 as the “ink” for inscribing structures into a transparent sample. The inscription is classified into transverse or longitudinal writing, depending on in which direction (with respect to the inscription laser propagation) the sample is translated during inscription, as sketched in figure 2.5. If the sample is mainly translated in the plane perpendicular to the laser propagation direction, as depicted in figure 2.5a, this is called transverse writing. If the structure is mainly inscribed in laser propagation direction, as depicted in figure 2.5b, this is known as longitudinal writing.

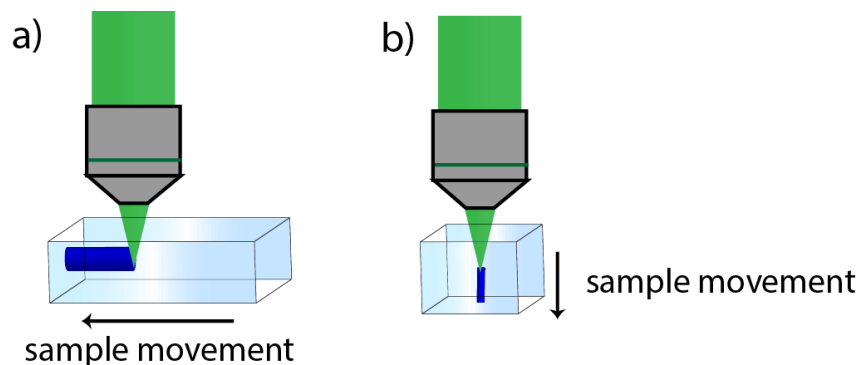


FIGURE 2.5. Classification of writing geometries for creating FLDW waveguides: a) transverse writing, b) longitudinal writing. Figure in the style of [51].

FLDW has been widely applied in various materials, including glasses [52–55], crystals [56–60], and polymers [61–63]. It is especially known for its three-dimensional processing capability, which has enabled the fabrication of, for example, waveguide splitters and fanouts [64–68], microfluidic devices [69], or optical data storage [70].

The first demonstration of femtosecond laser direct writing goes back to a publication in 1996 by Davis et al. [52], where femtosecond laser inscribed waveguides were presented in various glasses, including wet and dry silica. The group observed photo-induced permanent refractive index increases where the laser focus had been translated through the sample. This type of modification is generally referred to as type I. In the same year, the possibility to form voids in transparent materials was also reported [71]. This modification was later classified as type III. Three years

2.3. VOLUME MODIFICATIONS IN TRANSPARENT DIELECTRIC MATERIALS BY MEANS OF ULTRASHORT LASER PULSES

later, another type of modification showing birefringence was reported [72]. The underlying mechanism was found to be a self-organized, periodic material structure causing a refractive index modulation [73], which is why the modification was named “nanograting.” It is also often referred to as type II modification. For this work, mainly the modification types I and II are relevant. A summary of their properties will be given in the following subsections.

2.3.2.1. *Type I modification formation and properties.* After Davis et al. had published their results on writing waveguides into glass [52], researchers focused on finding the molecular cause for this behaviour. An answer was found in fused silica using Raman measurements: Fused silica in its original form predominantly contains 5- and 6-order silicon-oxygen ring structures. Raman measurements of modified fused silica after laser exposure, however, revealed an increased amount of 4-order ring structures [74, 75]. The decreased bond angle of these rings causes a densification of the material, which causes a refractive index increase. Similar structural changes in fused silica are known when the material is heated and then rapidly quenched [76]. Additionally, defects like non-bridging oxygen hole center and E'-centers are created during the inscription process [52, 77]. They also contribute to the refractive index change, although not as the main cause [53].

Today, the influence of several laser writing parameters on the modification properties in glass are known: With increasing **pulse energy**, the induced refractive index change increases [78]. Typical refractive index changes of waveguides are on the order of 10^{-4} to 10^{-3} . If the pulse energy is too high, however, nanogratings or void structures are created instead [79]. Typical pulse energies are on the order of a few hundred nanojoule [78, 79]. With decreasing **pulses per spot**, given by an increase of scanning velocity at a constant repetition rate, the induced refractive index change drops exponentially [80]. The choice of **numerical aperture** of the writing objective that is suitable depends on the available pulse energy, which then determines the intensity in the focal volume. Lower numerical apertures have the advantage that they are typically paired with longer working distances, which otherwise limits the flexibility of the writing process [81]. Additionally, very high numerical apertures can lead to a change in polarization [82]. At short **pulse durations** (≤ 50 fs), the processing parameter window for type I modifications widens, while for pulse durations above 200 fs, achieving type I modifications can become more difficult due to a narrower processing window [79]. However, smooth refractive index modifications have also been reported for pulse durations of 375 fs. For these longer pulse durations, green **wavelengths** seem to produce lower loss waveguides than infrared wavelengths [81]. Waveguides are considered “high quality” in literature when their loss is below 1 dB cm^{-1} [81]. The main loss mechanisms in

FLDW waveguides are Rayleigh and Mie scattering [83]. Waveguide writing in fused silica has been reported at various **repetition rates**, ranging, for example, from 1 MHz [81] to 1 kHz [84]. In borosilicate glasses it has been shown that using high repetition rates can trigger heat accumulation effects, which help in creating smooth and low-loss waveguides. In fused silica, however, the bandgap and the working temperature are significantly higher, making it harder to achieve heat accumulation and leaving the morphology independent of the repetition rate for a wide range of parameters suitable for waveguide fabrication [85, 86]. Instead of using the laser parameters to thermally alter the modification properties, the samples can also be annealed after inscription. Some groups have reported reduced losses and birefringence after annealing fused silica for 60 min at 570 °C [87]. However, at a similar temperature of 600 °C other groups have observed waveguide erasing and less guiding [88]. Both temperatures are higher than the 150 °C required to anneal color centers in fused silica [87], so defects do not contribute to the guiding after the annealing process.

Femtosecond laser direct written waveguides typically exhibit a certain amount of birefringence, even if they are purely made from type I modifications. Reasons for this are the elliptic waveguide cross section and asymmetry in the stress around the waveguide [87]. The elliptic waveguide cross section can be avoided when changing from transverse to longitudinal waveguide writing [89], however, this limits the length of the waveguides due to the working distance of the inscription objective. Instead, beam shaping methods can be employed to limit the ellipticity of the waveguide [54, 90, 91].

2.3.2.2. *Type II modification formation and properties.* Focused ultrafast laser pulses can induce periodic nanostructures acting as birefringent refractive index modifications if the laser parameters are suitable [72, 92, 93]. One of the first reported observations of these periodic structures in fused silica was in 1999, when Sudrie et al. published their observation of birefringence in femtosecond laser inscribed structures [72]. In 2002, Mills et al. reported on femtosecond direct written structures in fused silica with anisotropic reflection in the direction of the writing laser's polarization [73]. In their publication, Mills et al. considered the existence of self-organized periodic nanostructures as a cause of the previously reported effects. Subsequently, Shimotsuma et al. published their examinations of such femtosecond laser direct written structures using scanning electron microscopy and Auger electron spectroscopy [92]. To describe the morphology of the modification structures, they introduced the term "self-organized nanogratings". A decade later, Zimmermann et al. confirmed the existence of actual void structures in the modified material by

2.3. VOLUME MODIFICATIONS IN TRANSPARENT DIELECTRIC MATERIALS BY MEANS OF ULTRASHORT LASER PULSES

combined focused ion beam milling and scanning electron microscopy with X-ray scattering [94].

Since their first discovery, many efforts have been made to understand the development of nanogratings. When Shimotsuma et al. discovered the morphology of nanogratings in 2003 [92], they also proposed an early model for the formation, in which the interference between the incident laser light and plasma waves is the cause for nanograting formation. However, the implications this model had for the parameter dependencies of nanograting formation, like a strong dependency of the nanograting period on the inscription pulse energy, could not be confirmed. Other theories soon followed. Another model by Taylor et al. [95, 96], the so-called nanoplasmonic model, proposes the formation and growth of anisotropic plasma hotspots under laser irradiation. These plasma hotspots exhibit quasi-metallic properties when their electron density is high enough and will therefore act as waveguides for further incoming pulses. The position of these waveguides will then dictate the shape of the nanogratings. This model predicts the periodicity of nanograting structures to be $\lambda/(2n)$, given by the width of the lowest order mode supported by the electron plasma. However, experiments have shown, that even lower periodicities can be achieved [97].

Recently, Rudenko et al. demonstrated that the initial formation of nanogratings has the same electromagnetic origin as the formation of subwavelength surface nanoripples [98]. Both cases require some type of inhomogeneities or defects of the material, which seed the formation of nanopores. At these nanopores, local field enhancements perpendicular to the laser polarization occur, causing ionization processes to take place. The ionized volume can turn into a void during relaxation of the material, causing the nanopores to grow into nanoplanes. The directionality of the field enhancement causes the growth to occur perpendicular to the laser polarization. When nanoplanes are then further irradiated by laser pulses, they will scatter the incoming light, leading to interference of the scattered light with the incident light. This process will establish the grating periodicity of $\lambda/(2n)$. If other scattering centers are in the surrounding material, a superposition of multiple scattering waves can occur, allowing even smaller periodicities to form. This model only holds true if the expansion of the nanovoids is small enough, so when hydrodynamic expansion can be neglected. Otherwise hydrodynamic expansion can lead to an erasure of the structure. Therefore, prerequisites for the formation of in-volume nanogratings according to [98] are a high viscosity, a low thermal expansion coefficient and sufficiently low temperatures of the material during the inscription process.

Today, the following dependencies of nanograting properties on inscription parameters are known: Nanogratings consist of nanoscopic oxygen filled voids surrounded by

densified material [94, 99]. The grating planes arrange perpendicular to the writing **polarization** and evolve from random nanostructures, requiring enough overlapping laser pulses per volume element to develop into a well-ordered grating. The period p of the grating is roughly given by the inscription laser's **wavelength** λ and the materials refractive index n via $p = \lambda/(2n)$. However, even lower periods occur when the number of **applied pulses per volume element** is high enough [100]. Additionally, a second periodicity along the writing laser's propagation direction can arise for certain parameters [101]. Due to the subwavelength index modulations, nanogratings exhibit form birefringence for sufficiently long probing wavelengths (see section 2.1.1.2). The amount of birefringence can be tuned using suitable laser parameters [102, 103]: The **repetition rate** of the inscription laser should be smaller than 1MHz for highly birefringent nanogratings to form in fused silica, with lower repetition rates leading to higher birefringences. The highest optical retardations per inscription layer can be achieved with **pulse durations** of 0.25 ps to 2.5 ps. In this range, nanogratings fabricated with pulses above 1 ps show significantly higher retardations than modifications created with shorter pulse durations, but the processing window for fabricating nanogratings with pulse durations above 1 ps is narrower [103]. Nanogratings require higher **pulse energies** than waveguides to form. Typical thresholds for nanograting formation are at a few hundred nanojoule pulse energy. With increasing pulse energy, the modified volume increases, leading to a higher total optical retardation of the nanogratings [103]. Smaller numerical apertures of the focussing objective lead to a higher pulse energy threshold of nanograting formation. The maximum energy for nanograting formation is also dependant on the focussing conditions and is typically found at a few microjoule pulse energy. At these high pulse energies, microcracks start forming [103]. Several applications of nanogratings have been demonstrated, for example, using them as Bragg gratings [104], phase elements [105], polarizers [106] or as optical memories [70]. Nanogratings in fused silica also exhibit a higher etching rate than unmodified fused silica, making them useful for, e.g., fabricating microfluidic channels with smooth side walls [107]. In this work, nanogratings will be used to implement integrated wave plates operating as quantum gates.

2.4. Optical quantum computing

Quantum computing in general uses any quantum mechanical effects (for example, entanglement, superposition or quantum tunnelling [108]) to create a platform that can solve selected problems faster than a classical computer would [109]. In this thesis the usability of created structures for optical quantum computing is demonstrated. Optical quantum computing is based on encoding quantum information in photons. This section will summarize the basics of optical quantum computing, beginning

with using the photon to encode qubits (short for 'quantum bit' [108], the smallest unit of quantum information), and then concluding with single qubit quantum gates.

2.4.1. Photons as qubits. In optical quantum computing, single photons are used to encode the quantum information units known as qubits. A qubit can be any two-state quantum system, which can be represented by many degrees of freedom of photons, for example, path and polarization [2]. In the case of path-encoding, a photon used for qubit encoding may be in an arbitrary superposition of two paths 1 and 2:

$$|10\rangle_{12} = \begin{pmatrix} 1 \\ 0 \end{pmatrix} \text{ and } |01\rangle_{12} = \begin{pmatrix} 0 \\ 1 \end{pmatrix}. \quad (2.32)$$

In the case of orthogonal polarization states, the qubit may instead be in a superposition of two polarization states, for example, for horizontal and vertical polarization

$$|H\rangle = \begin{pmatrix} 1 \\ 0 \end{pmatrix} \text{ and } |V\rangle = \begin{pmatrix} 0 \\ 1 \end{pmatrix} \quad (2.33)$$

or for left and right circular polarization

$$\begin{aligned} |L\rangle &= \frac{1}{\sqrt{2}} \begin{pmatrix} 1 \\ i \end{pmatrix} = \frac{1}{\sqrt{2}}(|H\rangle + i|V\rangle) \\ \text{and } |R\rangle &= \frac{1}{\sqrt{2}} \begin{pmatrix} 1 \\ -i \end{pmatrix} = \frac{1}{\sqrt{2}}(|H\rangle - i|V\rangle). \end{aligned} \quad (2.34)$$

Path-encoding and polarization-encoding can be converted into each other using polarizing beam splitters [110]. To carry as much information as possible with a single photon, ideally multiple degrees of freedom are used contextually [9]. For simplicity reasons, the descriptions in this section will be given only in path encoding.

The quantum state for a single qubit in path encoding can be written as

$$|\Psi_1\rangle = \alpha_1 |10\rangle_{12} + \beta_1 |01\rangle_{12} = \begin{pmatrix} \alpha_1 \\ \beta_1 \end{pmatrix}, \quad (2.35)$$

with $|\alpha_1|^2 + |\beta_1|^2 = 1$. When measuring the state of the qubit $|\Psi_1\rangle$, the result will be $|10\rangle_{12}$ with probability $|\alpha_1|^2$ and $|01\rangle_{12}$ with probability $|\beta_1|^2$. A Poincaré sphere, like the one introduced in section 2.1.3, can be used to represent the Hilbert space of a qubit, for example, with abscissa ranging from $|01\rangle_{12}$ to $|10\rangle_{12}$, the

ordinate from $(|10\rangle_{12} - |01\rangle_{12})/(\sqrt{2})$ to $(|10\rangle_{12} + |01\rangle_{12})/(\sqrt{2})$, and the applicate from $(|10\rangle_{12} - i|01\rangle_{12})/(\sqrt{2})$ to $(|10\rangle_{12} + i|01\rangle_{12})/(\sqrt{2})$ [2]. If a second qubit $|\Psi_2\rangle$ in paths 3 and 4 is added, the combined quantum state can be given by the tensor product [108]

$$\begin{aligned} |\Psi_1\rangle \otimes |\Psi_2\rangle &= (\alpha_1 |10\rangle_{12} + \beta_1 |01\rangle_{12})(\alpha_2 |10\rangle_{34} + \beta_2 |01\rangle_{34}) \\ &= \alpha_1\alpha_2 |1010\rangle_{1234} + \alpha_1\beta_2 |1001\rangle_{1234} + \beta_1\alpha_2 |0110\rangle_{1234} + \beta_1\beta_2 |0101\rangle_{1234} \\ &= \begin{pmatrix} \alpha_1\alpha_2 \\ \alpha_1\beta_2 \\ \beta_1\alpha_2 \\ \beta_1\beta_2 \end{pmatrix} \equiv |\Psi_1, \Psi_2\rangle. \end{aligned} \quad (2.36)$$

Not all combinations of two qubits can be expressed using a tensor product, though. If the two-qubit state cannot be expressed by a tensor product, the two qubits are entangled. Well-known examples of entangled states are the so-called Bell-states, which can be written as [111]

$$|\Phi^{+, -}\rangle = \frac{1}{\sqrt{2}}(|00\rangle_{12} \pm |11\rangle_{12}) \text{ and} \quad (2.37)$$

$$|\Psi^{+, -}\rangle = \frac{1}{\sqrt{2}}(|01\rangle_{12} \pm |10\rangle_{12}). \quad (2.38)$$

2.4.2. Single qubit quantum gates. To change the quantum state of a photon, i.e., to implement a single qubit quantum gate, conventional optical elements like beam splitters and delay lines (in case of path encoding) or waveplates (in case of polarization encoding) can be used. With polarizing beam splitters, a conversion between polarization and path encoding can be made [2]. Single qubit quantum gates can be represented using 2 x 2 unitary matrices. Some typical quantum gates are those represented by the three Pauli matrices:

$$X = \begin{pmatrix} 0 & 1 \\ 1 & 0 \end{pmatrix}, Y = \begin{pmatrix} 0 & -i \\ i & 0 \end{pmatrix}, Z = \begin{pmatrix} 1 & 0 \\ 0 & -1 \end{pmatrix}. \quad (2.39)$$

Of these three operators, the Z operator acts as a phase flip and the X operator acts as a bit flip, making the X gate the quantum analogue of the classical NOT gate [108]. The Y gate can be constructed using a phase shift and a combination of the X and Z gate like so [112]: $Y = \exp(i\pi/4)\mathbb{1}XZ$. Other well-known gates are

2.5. LIQUID CRYSTALS

the Hadamard gate H and the Pi/8th gate T :

$$H = \frac{1}{\sqrt{2}} \begin{pmatrix} 1 & 1 \\ 1 & -1 \end{pmatrix}, T = \begin{pmatrix} 1 & 0 \\ 0 & \exp(i\pi/4) \end{pmatrix}. \quad (2.40)$$

For single qubit quantum computations, the Hadamard and the Pi/8th gate form a set of universal gates together [113].

To determine how close two quantum gates M_1 and M_2 are to each other, a common measure is the so-called fidelity, which is defined as $F^{|\psi\rangle} = |\langle \psi | M_1^* M_2 | \psi \rangle|^2$ [114]. M_1^* denotes the conjugate transpose of M_1 . The fidelity will have values ranging from 0 to 1, with a fidelity of 1 occurring when $M_1 = M_2$. In this thesis, this fidelity will be used to evaluate how well a desired quantum gate was fabricated.

2.5. Liquid crystals

One of the media used in this work to control the polarization properties of light in integrated circuits are liquid crystals. These are materials with a state of order ranging higher than the state of order of liquids, but lower than the state of order of crystals [115], as sketched in figure 2.6. The following section will discuss the discovery and the properties of this material type.

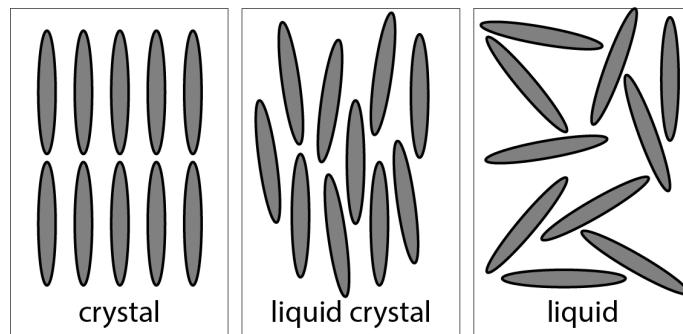


FIGURE 2.6. State of order of crystals, liquid crystals, and liquids. Figure is in the style of [116].

2.5.1. Phases of thermotropic calamitic liquid crystals. Liquid crystals occur in different states of order, known as phases. The way a transition between these phases is achieved is one way to categorize liquid crystals. There are thermotropic liquid crystals, lyotropic liquid crystals, or liquid crystals that show properties of both. In lyotropic liquid crystals, the phase transition is achieved by adding or removing a solvent, while in thermotropic liquid crystals, the phase transition is achieved by changing the temperature [117]. Additionally, liquid crystals

may be divided by the shape of their molecules, i.e., rod-like (“calamitic”) or plate-like (“discotic”) [115]. Furthermore, some liquid crystals exhibit multiple preferred axes [118]. In this work, only uniaxial thermotropic calamitic liquid crystals are used, which is why only their properties will be discussed here.

The most common phases of liquid crystals with rod-like molecules are nematic, smectic and cholesteric phases, which are sketched in figure 2.7.

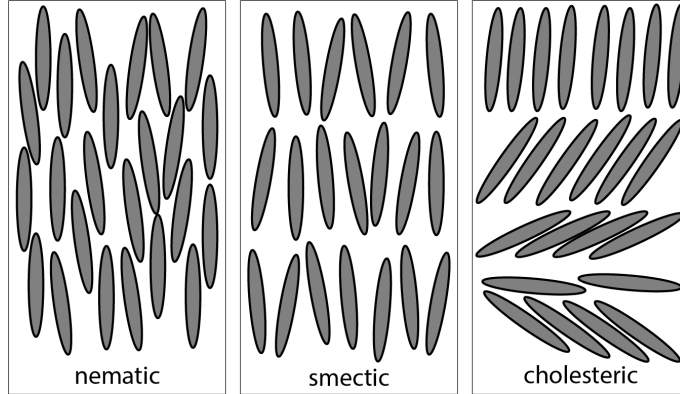


FIGURE 2.7. Common phases of liquid crystals with rod-like molecules. Figure is in the style of [119].

Of these, the nematic phase is the most simple one: the long axes of the molecules are aligned so that they all show in one direction. This direction is known as the director [115]. Apart from this orientation, the molecules are statistically distributed, in other words there is no long-range order of their position. The molecules can move around freely and rotate around the molecule’s axis. In the smectic phase on the other hand, the molecules not only have a common director, but additionally they are also arranged in planes. Lastly, in the cholesteric phase, each plane of molecules has a common director, but from layer to layer this director rotates helically [120].

2.5.2. Anisotropy of liquid crystals. The anisotropic ordering of liquid crystal gives rise to several interesting anisotropic properties. Among these, two well-known properties are the optical and the dielectric anisotropy. Both shall be discussed here.

2.5.2.1. *Dielectric anisotropy.* For liquid crystals, the polarizability changes in different directions along the molecular structure. The dielectric constant of the liquid crystal along the director of the molecule is $\epsilon_{\parallel LC}$, and the dielectric constant perpendicular to the director is $\epsilon_{\perp LC}$. Together this yields a dielectric anisotropy of $\Delta\epsilon = \epsilon_{\parallel LC} - \epsilon_{\perp LC}$.

If an electric field \vec{E} is applied to the liquid crystals, it will induce a dipole in the molecules. In effect, the molecules will align in a way that the induced molecular

2.5. LIQUID CRYSTALS

dipoles will face in the direction of the field, to minimize the interaction energy. Depending on the sign of the dielectric anisotropy, this can mean, that the directors of the molecules face in the direction of the electric field, or otherwise perpendicular to it. This can be understood by looking at the electrostatic energy density

$$U = \frac{1}{2} \vec{D} \vec{E} \quad (2.41)$$

with \vec{D} being the electric displacement field vector. Without loss of generality, it can be assumed that the electric field is in z -direction ($\vec{E} = E_z \vec{e}_z$) and that the director of the liquid crystals is at an angle θ with respect to the z -axis. The z -component of \vec{D} is given by

$$D_z = (\epsilon_{\parallel LC} \cos^2 \theta + \epsilon_{\perp LC} \sin^2 \theta) E_z. \quad (2.42)$$

Rearranging this equation yields

$$E_z = \frac{D_z}{(\epsilon_{\parallel LC} \cos^2 \theta + \epsilon_{\perp LC} \sin^2 \theta)}. \quad (2.43)$$

Knowing this, the electrostatic energy density can be rewritten as

$$U = \frac{D_z^2}{2(\epsilon_{\parallel LC} \cos^2 \theta + \epsilon_{\perp LC} \sin^2 \theta)}. \quad (2.44)$$

When the dielectric anisotropy is positive ($\Delta\epsilon = \epsilon_{\parallel LC} - \epsilon_{\perp LC} > 0$, so $\epsilon_{\parallel LC} > \epsilon_{\perp LC}$), the electrostatic energy density is minimized when $\theta = 0$, corresponding to a parallel alignment of liquid crystal to the electric field [121]. Vice versa, the energetically most beneficial orientation for negative anisotropy is an alignment perpendicular to the electric field.

2.5.2.2. Optical anisotropy. As described in section 2.1.1, any material with dielectric anisotropy will also exhibit optical anisotropy, i.e., birefringence. However, for optical anisotropy in contrast to dielectric anisotropy, the polarizability of the molecule at optical frequencies has to be considered, which might differ from the polarizability at the frequencies with which an external field is driven [122]. In the case of uniaxial nematic liquid crystals, the optical axis is in the direction of the director. Therefore, when rotating a liquid crystal in an electric field, also the optical axis of the system is rotated. The amount of birefringence of liquid crystals Δn is wavelength and temperature dependant. Typical values of Δn are in the range of 0.05 to 0.5 [122]. Considering a liquid crystal layer, where the liquid crystals have

an ordinary and an extraordinary refractive index of n_o and n_e , respectively, and where the director of the liquid crystals is at a varying angle $\theta(x)$ with respect to the x -axis. The thickness of the layer in x -direction is L . Assuming light propagating in x -direction through this liquid crystal layer, the local refractive index of this layer will be given by

$$n(x) = \frac{n_e n_o}{\sqrt{n_e^2 \sin^2(\theta(x)) + n_o^2 \cos^2(\theta(x))}} \quad (2.45)$$

The birefringence of this liquid crystal layer depending on the orientation of the directors along x will then be given by the integral along the propagation direction [123]

$$\Delta n = \frac{1}{L} \int_0^L |n(x) - n_o| dx. \quad (2.46)$$

2.5.3. Geometry of liquid crystal cells. Generally, a liquid crystal cell consists of two glass plates separated by a specific distance using spacers. The gap between the glass plates is filled with liquid crystals. On the glass plates, there are electrodes, often made out of indium tin oxide, which is transparent for visible light. On top of the electrodes, some kind of alignment layer follows. This could, for example, be a layer that causes homogeneous alignment of the molecules, meaning parallel to the alignment layer, or homeotropic alignment, i.e., perpendicular to the alignment layer, or otherwise an intermediate alignment [124]. A popular way of achieving homogeneous alignment is, for example, by rubbing polyimide with a cotton swab. The rubbing will reorient the polymer chains, giving rise to micro grooves in the polyimide. It is energetically more advantageous for the liquid crystals to align parallel to the grooves than perpendicular to them, resulting in a homogeneous alignment [124–126]. The in-plane orientation of the rods is given by the rubbing direction. For homogeneous alignment, the liquid crystals typically point up from the surface by a few degrees. The angle between the surface and the liquid crystal is commonly referred to as the pretilt angle. This pretilt angle is important for the liquid crystal device to function properly. Without any pretilt angle, each liquid crystal could tilt forwards or backwards when an external field is applied, causing the formation of reverse tilt domains. In between these domains, the orientation of the liquid crystals would then be ill defined. The pretilt angle breaks the symmetry between forwards and backwards tilting, causing a favoured tilting direction [125]. The sign of the pretilt angle is given by the rubbing direction [124]. Homeotropic alignment on the other hand is achieved by treating the glass with coupling agents, most commonly lecithin [127]. This is a molecule with hydrophobic and hydrophilic portions. The hydrophilic part of the molecule attaches to the glass, while the liquid crystals attach to the hydrophobic portion of the molecule, which is sticking up

2.5. LIQUID CRYSTALS

from the glass surface [124]. Similar alignment mechanics can also be achieved with silanes [128]. Both homeotropic and homogeneous alignment are possible, determined by the type of silane used.

The alignment layer of liquid crystal cells causes the molecules at the boundary of the cell to prefer a certain orientation, defining the ordering of nematic liquid crystals in that cell. If an external field (electric or magnetic) is now applied to this cell, the field exerts a torque on the molecule that counteracts the anchoring. Only when the torque of the external field reaches a critical strength, it is able to overcome the torque caused by the anchoring of the liquid crystals, enabling a reorientation. This is known as the Fréedericksz transition. For any voltage above the Fréedericksz threshold voltage, the resulting liquid crystal orientation is an interplay between the torque of the external field and the torque of the alignment. This results in a varying orientation of the director along the liquid crystal cell, giving rise to a birefringence that can be calculated according to equation 2.46 [123].

Depending on the operation scheme, several liquid crystal cells exist, of which four popular ones for nematic liquid crystals will be discussed here. These liquid crystal cell types are sketched in figure 2.8.

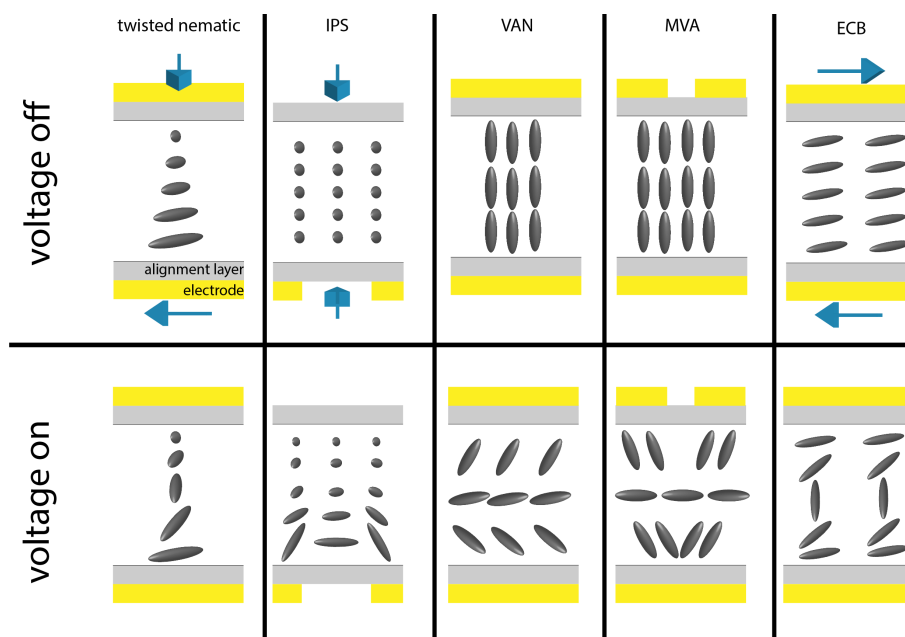


FIGURE 2.8. Selected liquid crystal cell types with and without an applied voltage (IPS –in plane switching, VAN –vertical aligned nematic, MVA –multi-domain vertical alignment, ECB –electrically controlled birefringence). The blue arrows denote the rubbing direction for the cells with homogeneous alignment.

The first type is the twisted nematic cell. In the twisted nematic cell, the rubbing of one glass plate is rotated by 90° with respect to the other glass plate, causing the

director of the liquid crystals to rotate by 90° along the cell. This cell requires liquid crystals with positive dielectric anisotropy [129]. When adding a voltage to this cell, the molecules of the liquid crystal will unwind according to the orientation of the electric field. When two crossed polarizers are put around the cell, this can be used to block light when a voltage is applied or else let light pass when there is no voltage applied [130]. Another configurations of liquid crystal cells is the in-plane switching (IPS) cell. In this cell configuration the two electrodes are not on opposing glass plates, but instead both on the same glass plate, with a certain space in between. This cell is also often operated between two crossed polarizers, that block the light when no voltage is applied. When a voltage is added to the IPS cell and the liquid crystals start to rotate in the direction of the resulting inhomogeneous electric field, light can pass through the crossed polarizers. IPS cells may have either parallel or antiparallel rubbing [124]. In figure 2.8 parallel rubbing is sketched. A third example of a liquid crystal cell type is the vertical aligned nematic (VAN) cell [124], which only works for liquid crystals with negative dielectric anisotropy [131]. Here, a homeotropic alignment of nematic liquid crystals is chosen. This liquid crystal cell is then typically placed between two crossed polarizers. When no voltage is applied, the optical axes of the liquid crystals are perpendicular to the transmission orientation of the polarizer in front of the liquid crystal cell. Therefore, no light is transmitted through the crossed polarizer behind the cell. When a voltage is applied, the liquid crystals rotate, and due to their birefringence, light will be transmitted through the polarizers [132]. Further developments of this type of cell are the multi-domain vertical alignment (MVA) by Fujitsu or the patterned vertical alignment (PVA) by Samsung. In these technologies the electrode on one side of the glass is split and shifted apart to achieve slants of the liquid crystal alignment across the cell when a voltage is applied [133]. Finally, the liquid crystal cell used in this thesis is known as zero-twisted electrically controlled birefringence (ECB) cell [134, 135], or also Freédericksz cell operated in ECB mode [124]. In this cell, the rubbing of the alignment layer is anti-parallel, leading to a homogeneous alignment of the liquid crystals when no voltage is applied. If a sufficiently high voltage is applied, the liquid crystal molecules rotate. Thus, the retardance of the cell can be controlled using the applied voltage. It is maximum, when no voltage is applied, and decreases with increasing applied voltage.

2.5.4. The E7 liquid crystal mixture. To widen the temperature range in which liquid crystals are nematic, they may be mixed together [121]. The properties of such mixtures differ from the properties of their constituents and change with the concentration of the constituents. This allows the tailoring of physical and optical properties [136]. However, it can be challenging to find a composition which

is thermodynamically stable [137]. One widely used liquid crystal mixture is E7, which is also used in this thesis. For this work, E7 was obtained from the company Synthron Chemicals. According to their web catalog, the constituents are 5CB, 7CB, 8OCB and 5CT [138]. Table 2.3 lists the molecule lengths. The product data sheet reads that the water content of the mixture is at 0.01 % and the ordinary refractive index n for light of wavelength $\lambda = 589$ nm lies at $n = 1.5240$. The clearing point is at $T_c = 58.6$ °C. Typical birefringences Δn of mixtures of this type are around $\Delta n = 0.225$ for light of wavelength $\lambda = 589$ nm and dielectric anisotropies $\Delta\epsilon$ at 1 kHz voltage frequency are around $\Delta\epsilon = 13.8$ (all values obtained at 20 °C) [115].

TABLE 2.3. Molecule lengths and formulas of constituents of the E7 liquid crystal mixture.

Constituent	Formula	Molecule length [Å]
5CB	$C_{18}H_{19}N$	16.3 [139]
7CB	$C_{20}H_{23}N$	18.7 [139]
8OCB	$C_{21}H_{25}NO$	23 [140]
5CT	$C_{24}H_{23}N$	22 [140]

2.6. State of the art

To place this thesis in the current research field, the latest relevant achievements in the field of femtosecond laser direct writing of photonic waveguides will be briefly reviewed here. Today, FLDW is a well-established technique for fabricating optical devices [141, 142]. Compared to bulk optical setups, integrated photonic circuits can be more compact, less noisy, more stable, and easier scalable [110]. These features are especially relevant for quantum computing, which has received pronounced attention in recent years. Both single and two-qubit gates have been demonstrated for FLDW integrated photonic circuits: In the case of path-encoding, single qubit gates are realized by directional couplers [143], whilst multiple directional couplers with specific splitting ratios can be used to create two-qubit gates [144, 145]. More interesting for this thesis, however, is the demonstration of quantum gates in polarization encoding, since this requires polarization control in the circuit. On the one hand, this concerns the waveguides, where not only low losses are required [146], but also low birefringence, to avoid decoherence. On the other hand, adding localized polarization manipulation is required to achieve quantum gates. Early classical demonstrations of adding polarization control to FLDW circuits included using nan gratings as waveguides [147]. While this approach makes a wide variety of delays available, it is limited in that the optical axis of the structures cannot be changed. Furthermore, the ability of adjacent waveguides to influence each others birefringence due to their surrounding stress fields has been demonstrated [148].

Two-qubit polarization encoded quantum gates have been demonstrated by using multiple partially and/or fully polarizing directional couplers [149, 150]. Polarization-encoded single qubit quantum gates were demonstrated, for example, by using birefringent FLDW waveguides as retardation elements [151]. These were inscribed through a high numerical aperture objective, where the objective's aperture was only partially filled. By changing the position, where the inscription laser hits the objective, a tilting of the inscription focus can be achieved, which results in tilting of the waveguide and thereby also a tilt of the optical axis of the waveguide, as shown in figure 2.9.

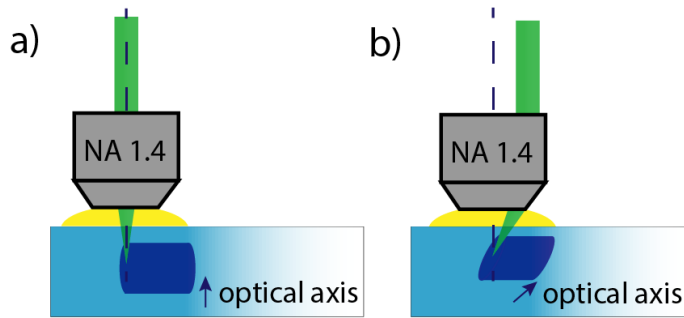


FIGURE 2.9. Inscription scheme using an underfilled high NA immersion objective to create tilted waveguides that are used as retardation elements in [151].

A laser beam passing through the objective on axis would lead to a waveguide with the optical axis being perpendicular to the sample's surface. A laser beam passing through the objective off-axis, on the other hand, leads to a rotation of the optical axis, with the amount of rotation given by how far off-axis the laser was. The strongest tilt achieved with this method were 45° , however, the authors reported that the results were less reliable for this strong tilt, because the displaced inscription laser reached the edge of the objective's aperture, leading to beam distortions. The birefringence of the waveguides was on the order of 2×10^{-5} . A half-waveplate for 800 nm light therefore requires a 2 cm long waveguide. The authors validated their approach by creating an integrated quantum state tomography device [151].

A second approach for achieving integrated single qubit quantum gates was demonstrated by writing defect tracks next to waveguides [152]. The stress field around the defect track interacts with the stress field of the waveguide, inducing birefringence in the waveguide, with the orientation of the birefringence given by the relative position between the defect track and the waveguide. The required length to achieve half-waveplate orientations with this approach were on the order of centimeters. To demonstrate the functionality of the structures, single qubit quantum gates were created and characterized using single photons [152].

2.6. STATE OF THE ART

All of these approaches to functionalize FLDW waveguides share one significant downside: the missing tunability of the fabricated circuit. The most prominent approach so far to allow reconfiguration of FLDW circuits is using thermal phase shifting. A lot of work has been published on demonstrations of thermal shifters in Mach-Zehnder interferometers [153–156]. A resistor acting as a heater is added to one arm of the interferometer, so that a phase shift depending on the thermal power dissipated by the heater is achieved. This has been implemented in a photonic circuit for dynamic quantum state preparation [157]. In later designs of this approach, to avoid thermal cross-talk, the samples were structured so that there were insulating air gaps between the waveguides [158, 159]. A different approach to the one using a thermal shift, is to use the Kerr effect to tune the refractive index in one arm of a directional coupler, thereby tuning the coupling ratio [160, 161].

The typical material of choice for many of the above mentioned quantum gates is borosilicate glass (for example, Corning EAGLE 2000) [9, 144, 145, 149, 151, 162]. In fact, only in a few selected works the material fused silica is used [143, 150, 152]. An explanation for this is given in [162]: The material choice is made to avoid birefringence. Unwanted birefringence in waveguides can become problematic because it can destroy indistinguishability of two photons and cause decoherence for photons with small coherence times. In fused silica, exposure to femtosecond laser pulses under certain irradiation conditions can lead to the formation of birefringent nanogratings [92, 163, 164]. These are less likely to form in borosilicate glasses [98, 165], so by opting for borosilicate glasses the risk of additional birefringence caused by nanogratings is avoided. Additionally, heat accumulation at high repetition rates can be exploited to create cylindrical symmetric waveguides for borosilicate. Attempts to use heat accumulation for waveguide writing in fused silica have failed [85], probably due to its higher bandgap (9 eV in fused silica compared to 4 eV in borosilicate), higher thermal diffusivity ($8.1 \times 10^{-7} \text{ m}^2/\text{s}$ for fused silica vs. $6.1 \times 10^{-7} \text{ m}^2/\text{s}$ for Borofloat 33 [103], a kind of borosilicate) and higher working point (1800 °C for fused silica vs. roughly 1300 °C for borosilicate). Despite all these technical differences, the reported losses and birefringence of waveguides created in fused silica and borosilicate are rather similar. Reported losses range from 0.2 dB cm^{-1} to 2 dB cm^{-1} depending on the transmitted wavelength for either borosilicate [166, 167] or fused silica [168, 169]. Some groups have even reported losses as low as 0.1 dB cm^{-1} in fused silica [170]. The reported birefringences range on the order of 1×10^{-5} to 1×10^{-6} in either fused silica [148, 152] or borosilicate [162, 171].

To conclude, the following approaches for creating polarization encoded single qubit quantum gates in glass-based FLDW waveguides exist: The addition of stress tracks next to waveguides [152] or the use of tilted, birefringent waveguides as

retarders [151]. Due to the low birefringence of the structures in both approaches, the fabricated retarders required lengths in the range of centimeters. Also, several approaches of using either thermal effects [153–156] or the Kerr-effect [160, 161] to add reconfigurable elements to FLDW circuits have been demonstrated before. However, none of these were designed to change the polarization state inside the waveguides. In the case of the thermal reconfiguration, typical heat elements have widths of at least $45\ \mu\text{m}$ [156].

Therefore, the following objectives are derived for this work: It will be shown that fused silica still is a useful material for creating integrated optical quantum circuits for polarization-encoded photons. To do so, it will be shown that low birefringence waveguides are possible in fused silica by a careful choice of parameters and beam shaping. Furthermore, it will be shown that nanogratings are not a hindrance to quantum computing but instead can be used to create integrated waveplates with arbitrary orientation and a thickness on the order of $1 \times 10^2\ \mu\text{m}$, which is orders of magnitude shorter than the approaches for polarization-encoded single qubit quantum gates mentioned in this section. These waveplates will be characterized with single photons, to demonstrate their usability as quantum gates. Furthermore, reconfigurable polarization changing elements will be demonstrated, using an $8\ \mu\text{m}$ thick liquid crystal sheet embedded into an FLDW waveguide.

CHAPTER 3

Experimental Setups

In this chapter, the setup used to inscribe structures into the fused silica samples (writing setup) and the setup to inspect the modifications after inscription (characterization setup) are presented. Sketches are included for clarification.

3.1. The writing setup

The inscription setup is shown in figure 3.1. The laser used in this work was an Amplitude Satsuma laser producing pulses of 1030 nm wavelengths, which were frequency doubled using second harmonic generation to 515 nm wavelength. The shortest pulse duration achievable using this system is 300 fs. This was the pulse duration chosen for all inscriptions because type I modifications have a larger fabrication parameter window when fabricated with this pulse duration compared to longer pulse durations. The pulse energy of the laser is set using a combination of a half-waveplate and a polarizer.

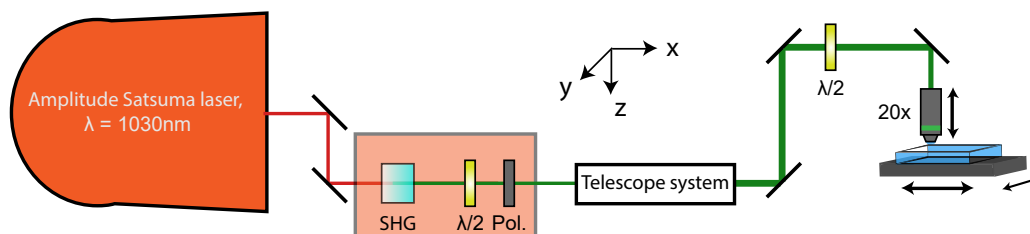


FIGURE 3.1. Inscription setup (SHG = second harmonic generation, $\lambda/2$ = half-waveplate, Pol. = polarizer).

The laser beam is widened using a telescope system (initially a spherical Galilean telescope with a ratio of 1:3, with focal lengths of -50 mm and 150 mm , which widened the beam to fill the inscription objective's aperture; other types of telescopes are explained in the text whenever they are applied). A second rotating half-waveplate is used to set the polarization of the laser. The widened laser beam is then focused through a 20x objective. For some parts of this thesis, this was an Olympus plan objective ($NA = 0.4$). Later, this was changed to a Mitutoyo long focal distance objective, to allow focussing deeper into the sample ($NA = 0.42$). The $1/e^2$ -focal spot size of the beam using these focussing conditions was measured via calibrated camera images to be $(2.8 \pm 0.2)\ \mu\text{m}$ in both cross sections for both objectives. The sample is positioned on an x-y-stage (Aerotech ANT130-XY), while the objective

is mounted on a z-stage (Aerotech ANT130-060-L). These axes allow ultra-precise positioning of the objectives' focus in the sample (1 nm resolution, $\leq 5 \mu\text{m}$ accuracy, 100 nm bi-directional repeatability). By translating the sample through the focus of the objective while the inscription laser is running, modifications are created. If not otherwise specified, the material of choice for the experiments in this thesis was UV-grade fused silica, with an OH-content of 1200 ppm and an impurity content of 5 ppm.

3.2. The characterization setup

Once a structure has been inscribed using the setup in figure 3.1, the resulting modifications should be optically characterized. For a first visual impression a microscope in transmission can be used. For investigations of further properties, like losses, birefringence, the mode field profile of waveguides or the dichroism of nanogratings, a characterization setup was built, that included several characterization options. The basic setup is given in figure 3.2a. There are two sources available for the setup, the first one being a continuous wave titanium-sapphire laser that was usually operated at 808 nm wavelength (Spectra-Physics 3900S), and the second one a tuneable helium-neon laser with 5 discrete wavelengths available from 543 nm to 633 nm (Research Electro-Optics, Inc.). Each laser has its own advantages. The titanium-sapphire laser allows the characterization of structures with wavelengths that are readily available as single photon sources. This is of special interest for any structures which are to be used for quantum photonics. The helium-neon laser has a high stability, whilst offering several wavelength options in the visible regime.

The laser of choice is focused into the sample using a 4x Olympus plan objective, either to couple the light into the waveguide of interest or to confine the light to the region of interest in the sample. Behind the sample, a 20x Olympus plan objective is then used to image the light transmitted through the sample onto the detector. An iris diaphragm between objective and detector can be used to filter out any background around the region of interest. Depending on the desired characterization, various kinds of detectors can be used. To measure losses, the detector will be a powermeter, to image mode fields, a camera will be used, and to monitor the change of Stokes parameters, a polarimeter will be employed.

For characterizing the birefringence and dichroism of the structures, the characterization setup is equipped by a set of crossed polarizers and a half-waveplate, as depicted in figure 3.2b. All wavelength-sensitive components of the setup are exchanged when the source is changed. The laser light is transmitted through a polarizer and a half-waveplate to set the input polarization before entering the sample. Behind the sample, an analyzer is positioned. Both the half-waveplate and the analyzer are

3.2. THE CHARACTERIZATION SETUP

mounted on rotating stages, which allow the measurement of the transmitted light in both crossed polarizer configuration and parallel polarizer configuration. The detector of choice for this kind of setup is a powermeter.

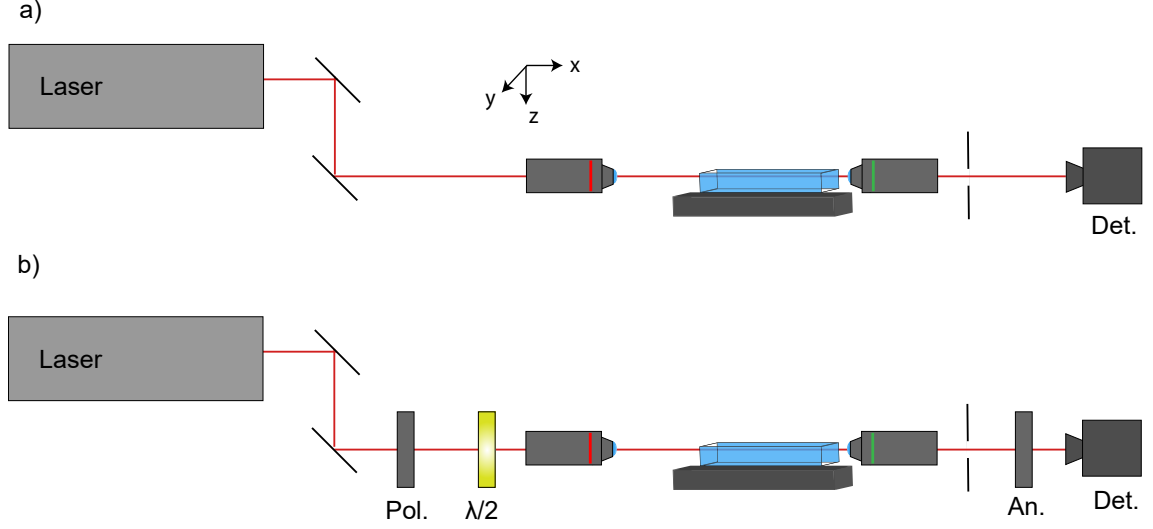


FIGURE 3.2. Characterization setup in a) the basic configuration and in b) equipped for birefringence and dichroism measurements ($\lambda/2$ = half-waveplate, Pol. = polarizer, An. = analyzer, Det. = detector).

To understand how this setup can be used to retrieve birefringence and dichroism properties, the Mueller matrix calculus introduced in section 2.1.3 has to be employed. For simplicity, the reference system for this calculation will be chosen in such a way that the sample appears to be rotating by an angle θ , while the input polarization is fixed at horizontal and the analyzer will be transmitting vertical polarization. The rotation of the sample is expressed in mathematical terms using the rotational matrices $\overset{\leftrightarrow}{R}(\theta)$. The sample $\overset{\leftrightarrow}{M}_{sample}$ will be modelled as a linear diattenuating retarder with diattenuation D as defined in table 2.2.

The overall transmission $T_{all}(\theta)$ of the setup is obtained by adding together the transmission values $T_{cross}(\theta)$ when the polarizer is crossed to the input polarization and the transmission values $T_p(\theta)$ when the polarizer is parallel to the input polarization for various input polarization angles θ . This transmission is only dichroism dependent and not birefringence dependent and given by:

$$\begin{aligned}
 T_{all}(\theta) &= \left[\left(\left(\begin{pmatrix} \frac{1}{2} & -\frac{1}{2} & 0 & 0 \\ -\frac{1}{2} & \frac{1}{2} & 0 & 0 \\ 0 & 0 & 0 & 0 \\ 0 & 0 & 0 & 0 \end{pmatrix} + \begin{pmatrix} \frac{1}{2} & \frac{1}{2} & 0 & 0 \\ \frac{1}{2} & \frac{1}{2} & 0 & 0 \\ 0 & 0 & 0 & 0 \\ 0 & 0 & 0 & 0 \end{pmatrix} \right) \overset{\leftrightarrow}{R}(\theta) \overset{\leftrightarrow}{M}_{sample} \overset{\leftrightarrow}{R}(-\theta) \begin{pmatrix} 1 \\ 1 \\ 0 \\ 0 \end{pmatrix} \right]_{S_0} \\
 &= T_{ave} + \frac{\Delta T}{2} \cos(2\theta) = T_{ave}(1 + D \cos(2\theta)). \quad (3.1)
 \end{aligned}$$

The mean value of $T_{all}(\theta)$ yields T_{ave} , while the difference between the maximum and the minimum value of $T_{all}(\theta)$ yields ΔT . According to equation (2.13), this is sufficient to find the dichroism of the observed modification.

The transmitted power through the system when the polarizers are crossed is then given by the first Stokes parameter S_0 as

$$T_{cross}(\theta) = \left[\begin{pmatrix} \frac{1}{2} & -\frac{1}{2} & 0 & 0 \\ -\frac{1}{2} & \frac{1}{2} & 0 & 0 \\ 0 & 0 & 0 & 0 \\ 0 & 0 & 0 & 0 \end{pmatrix} \overset{\leftrightarrow}{R}(\theta) \overset{\leftrightarrow}{M}_{sample} \overset{\leftrightarrow}{R}(-\theta) \begin{pmatrix} 1 \\ 1 \\ 0 \\ 0 \end{pmatrix} \right]_{S_0} = \frac{T_{ave}}{2} \sin^2(2\theta) \cdot (1 - \sqrt{1 - D^2} \cos(\delta)). \quad (3.2)$$

Afterwards, this measurement is divided by the average overall transmittance through the sample, which results in a sine square curve with a diattenuation and retardation dependant amplitude:

$$\frac{1 - \sqrt{1 - D^2} \cos(\delta)}{2} \sin^2(2\theta). \quad (3.3)$$

By fitting equation (3.2) to the data retrieved using the crossed polarizer setup, while applying the retrieved value for the dichroism, the birefringence of the sample can be found. Variations of either the retardation or the dichroism along the propagation direction of the laser cannot be resolved using this setup.

An alternative to this setup is a commercial polarimeter (ilis StrainMatic M4/60.13 zoom) that can be used to quickly measure the retardation of large areas. The resolution of the device is limited to $5 \mu\text{m}$, which is too low for reasonable waveguide characterizations. Nevertheless, it allows quick and comfortable measurements of the retardations of nan gratings. The operating wavelength of the device is 587 nm . Unfortunately, this device does not account for dichroism, which can cause inaccuracies in the results. To estimate these inaccuracies, nan gratings were measured with both the characterization setup and the StrainMatic polarimeter. The results are presented and compared in chapter 5.

CHAPTER 4

Femtosecond Laser Direct Written Waveguides

Waveguides in this thesis serve the purpose of transporting photons from one place to the other without changing the photon's polarization. This means that the waveguides ideally have as little birefringence and losses as possible. To achieve this, suitable inscription parameters have to be found, and their influence on birefringence and losses of waveguides have to be determined. In this section different effects playing into measuring the losses will be discussed. Subsequently, the influence of different parameters on waveguide birefringence and losses will be shown.

4.1. Loss measurements

Measuring losses of waveguides is more tricky than just measuring the transmitted power with and without the sample in the setup, due to various additional loss mechanisms that decrease the transmission. This includes Fresnel reflection at the surfaces of the sample, mode overlap with the input light, and the Fabry-Perot-effect. These three effects will be explained here.

Assuming that the waveguides were well-positioned so that the input light of intensity I_{in} and wavelength $\lambda = 808$ nm hits the fused silica sample with refractive index $n_{fusi} = 1.45$ [172] at a 90° angle, then the Fresnel losses are given by

$$R_{fres} = \left(\frac{n_{fusi} - n_{air}}{n_{fusi} + n_{air}} \right)^2 = 3.4\%, \quad (4.1)$$

where $n_{air} = 1$ [173] denotes the refractive index of air. Fresnel losses don't count as waveguide losses because they are not determined by the waveguide, but by the refractive index of the surrounding of the waveguide. They occur twice, both at the input and at the output of the sample.

The overlap integral is a measure of how well the input light fits to the mode of the waveguide. It doesn't count as a waveguide loss, because it is determined by the input light source. Theoretically, if the input light source has an intensity distribution that matches the waveguide's mode field perfectly, this loss could be avoided. The waveguides investigated in this thesis were single-mode with a graded index modification. For these types of waveguides, it is a common approach to approximate the fundamental mode using Gaussian functions [174]. By taking one

camera image of the output mode field of the waveguide under inspection and another camera image of the focal spot of the objective that is used to launch light into the waveguide, the overlap integral can be found: Elliptical Gaussian functions of the shape

$$I_i(x, y) = |E_i(x, y)|^2 = A_i \cdot \exp\left(-\left(\frac{x}{w_{xi}}\right)^2 - \left(\frac{y}{w_{yi}}\right)^2\right), i \in \{1, 2\} \quad (4.2)$$

are fitted to both images, yielding widths w_{x1} , w_{x2} , w_{y1} and w_{y2} . Based on the fit results, the overlap integral can be calculated via [38]

$$\eta = \frac{|\int \int_{-\infty}^{\infty} E_1(x, y, z)^* E_2(x, y) dx dy|^2}{\int \int_{-\infty}^{\infty} |E_1(x, y, z)|^2 dx dy \int \int_{-\infty}^{\infty} |E_2(x, y)|^2 dx dy} = \frac{4w_{x1}w_{x2}w_{y1}w_{y2}}{(w_{x1}^2 + w_{x2}^2)(w_{y1}^2 + w_{y2}^2)}. \quad (4.3)$$

Here, E_1 is the input light distribution and E_2 is the mode field. Another effect which can change the transmission measurement is the Fabry-Pérot effect. For this effect to occur, the light launched into the waveguide has to be coherent, with a coherence length of at least twice the waveguide's length. To estimate the coherence length of the main laser used for characterizing the waveguides, its spectral widths was measured using a spectrometer. The laser's wavelength is 808 nm. By fitting a Gaussian curve to the measured data, the spectral full width at half maximum was determined to be $\Delta\lambda = (0.5 \pm 0.2)$ nm. The coherence length is then given by [175] $\Delta s_c = \frac{\lambda^2}{n_{fusi} \cdot \Delta\lambda} = \frac{(808 \text{ nm})^2}{1.45 \cdot (0.5 \pm 0.2) \text{ nm}} \leq 1.5$ mm. Since the sample of the waveguide is typically 4 cm long, the Fabry Perot effect was neglected in this thesis.

To finally determine the losses of the waveguide, the ratio of the transmitted power through the waveguide to the input power has to be measured, followed by removing losses caused by Fresnel reflection at the input and output of the waveguide, and mode mismatch at the waveguide facet (quantified by the overlap integral). The birefringence of the waveguides on the other hand is measured using the same setup as is used for the nanograting characterization. The setup is depicted in figure 3.2 and explained in section 3.2.

4.2. Waveguide writing using a Gaussian beam

In this section the investigations on waveguide writing with a Gaussian beam will be described. Since the creation of waveguide using FLDW is a highly nonlinear process, even small variations of parameters have a significant impact on the inscription process, making it necessary to optimize inscription parameters for every inscription setup individually, even though the general dependencies of waveguide properties on laser parameters are already known (and listed in section 2.3.2.1). The shortest

4.2. WAVEGUIDE WRITING USING A GAUSSIAN BEAM

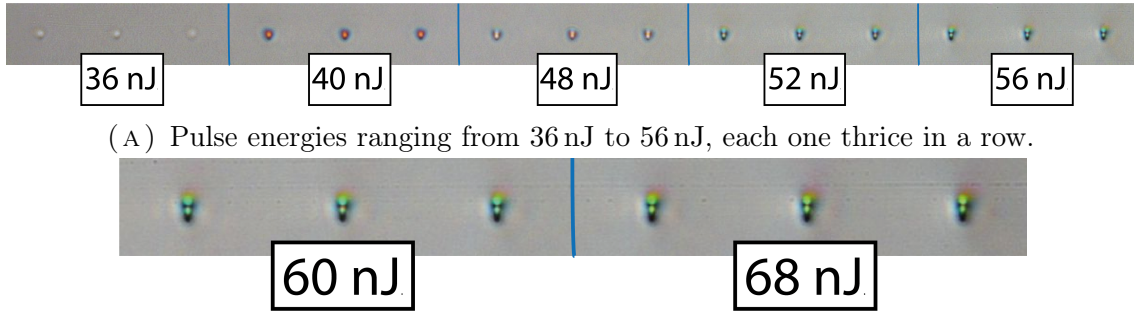
available pulse duration of the laser system used in this thesis is around 300 fs, which (as mentioned in section 2.3.2.1) limits the processing window for creating waveguides. At the same time the produced waveguides shall have a high performance, meaning they should ideally have no losses and no birefringence. It is not imminently clear which combination of parameters at the given pulse duration can fulfill these demands the best, which is why the parameter scans are necessary.

It was previously reported, that for lasers operating in the green wavelength range at roughly 300 fs pulse duration, optimal waveguide writing conditions could be found at a repetition rate of 1000 kHz and scanning speeds of 3 mm min^{-1} to 300 mm min^{-1} , when the focussing lens had a numerical aperture of $NA = 0.4$ [81]. Based on these observations, the parameter set used as a starting point for the first parameter scan was chosen to be 100 mm min^{-1} scanning speed, 1000 kHz repetition rate and 36 nJ to 56 nJ pulse energy. All scans were made at a constant focal depth of $150 \mu\text{m}$ below the surface, so that the influence of aberrations are kept constant. The testing wavelength to determine birefringence and losses of the waveguides was 808 nm. All presented loss and birefringence measurement values are the average over three waveguides written with the same parameters.

It was observed that at 36 nJ, the pulse energy was just above the modification threshold, with the modification barely visible under a transmission microscope, and not guiding light. For pulse energies of 40 nJ and higher, the structures guided light of 808 nm. When looking at the end facets of the waveguides for pulse energies of 52 nJ and higher (figure 4.1), two bright areas appear instead of only one, indicating that the laser might undergo self-focussing and self-phase modulation during inscription. This is a nonlinear propagation effect that occurs at high peak intensities of the laser pulses [176]. It has been reported before that these effects can cause waveguide distortion [177].

The losses and retardation of the waveguides measured with laser light of 808 nm wavelength are plotted in figure 4.2. The losses range between 1.7 dB cm^{-1} to 2.8 dB cm^{-1} , while the retardation shows values between $0.03 \pi/\text{cm}$ and $0.15 \pi/\text{cm}$. It can be seen that the losses are reduced with rising pulse energy, but the waveguide's optical retardation fluctuates with rising pulse energy. This makes optimizing the waveguide for minimum losses at minimal birefringence difficult.

To conclude, the waveguides achieved in this section do not yield satisfactory results. At low pulse energies, the waveguides are very lossy, while at higher pulse energies, nonlinear effects occur, distorting the waveguides. Therefore, in the next section it will be studied whether using beam shaping, waveguides with better properties can be obtained. It has been previously shown, that elliptical beam shaping can help



(A) Pulse energies ranging from 36 nJ to 56 nJ, each one thrice in a row.

(B) Pulse energies of 60 nJ (left) and 68 nJ (right), each one thrice in a row. The size of this figure is increased so that the details of the modification are more readily visible.

FIGURE 4.1. Microscope image of modification/waveguide end facets inscribed with various pulse energies. The distance of two modifications is $100\ \mu\text{m}$. The writing parameters were $100\ \text{mm}\ \text{min}^{-1}$ scanning speed, $1000\ \text{kHz}$ repetition rate, and a focus position of $150\ \mu\text{m}$ below the surface.

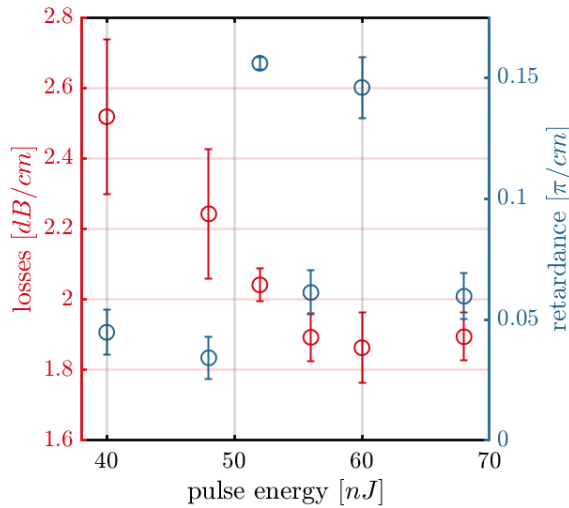


FIGURE 4.2. Losses and optical retardation of waveguides written with various pulse energies at $150\ \mu\text{m}$ below the surface, with $100\ \text{mm}\ \text{min}^{-1}$ scanning speed and $1000\ \text{kHz}$ repetition rate. The probing wavelength for these measurements was $808\ \text{nm}$. The laser was previously expanded by a spherical Galilean telescope and focused through a $20\times$ ($NA = 0.4$) objective lens.

reduce the birefringence of FLDW waveguides [54]. This elliptical beam shaping can be achieved, for example, by using a cylindrical telescope. A positive side effect of this beam shaping technique is the reduction of the peak intensity in the focal volume, which can help mitigate the impact of nonlinear propagation effects on the resulting volume modifications. The influence of using an elliptically shaped laser beam for waveguide inscription will be discussed and demonstrated in the following section.

4.3. Waveguide writing with elliptically shaped beams

To understand why elliptic beam shaping might be useful for reducing the birefringence of waveguides, please refer back to equation (2.31) in section 2.3.1, where the absorption process of electrons in femtosecond laser micro-machining is explained. This equation links the free electron density in the focal volume of the laser pulse with the intensity of the laser pulse. Wherever the free electron density is high enough, a permanent refractive index modification will be left after irradiation. Therefore, the intensity distribution of the laser pulse will determine the geometry of the refractive index modification. In the following considerations, nonlinear propagation effects will be neglected for simplicity reasons. Due to these simplifications, deviations may occur in practice. Nevertheless, these simple considerations help to develop an idea of how elliptical beam shaping affects the laser-induced modifications.

The intensity distribution I_{gauss} of a Gaussian beam with wavelength λ is given by

$$I_{gauss}(x, y, z) = I_0 \frac{w_{0x}}{w_x(z)} \frac{w_{0y}}{w_y(z)} \exp\left(-2 \left[\frac{x^2}{w_x(z)^2} + \frac{y^2}{w_y(z)^2} \right]\right). \quad (4.4)$$

Here, I_0 denotes the intensity at $x = 0$, $y = 0$ and $z = 0$. The beam radii w_x and w_y in x and y are given by

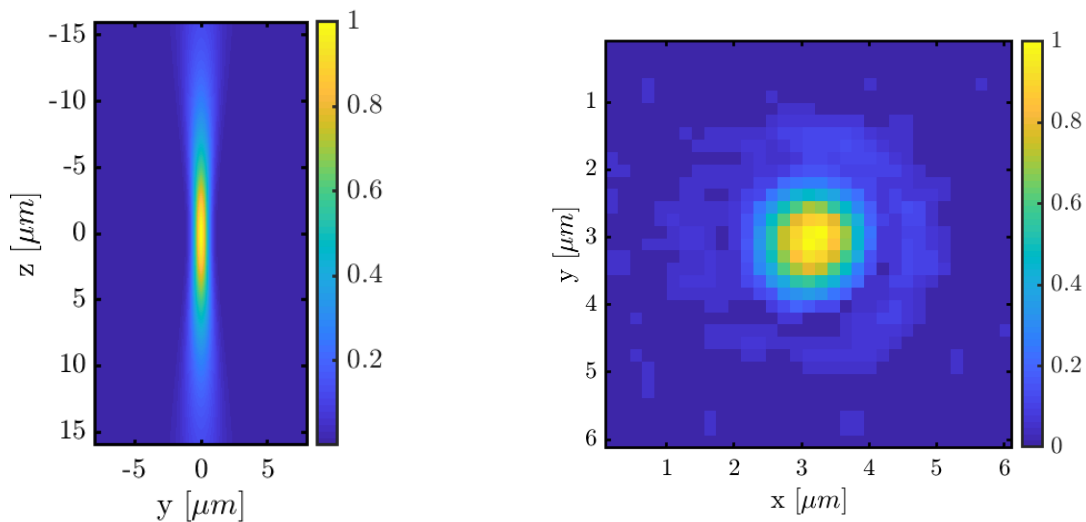
$$w_x = w_{0x} \sqrt{1 + \left(\frac{z}{z_{Rx}}\right)^2} \quad \text{and} \quad w_y = w_{0y} \sqrt{1 + \left(\frac{z}{z_{Ry}}\right)^2} \quad (4.5)$$

with the beam radius at $z = 0$ being w_{0x} and w_{0y} , respectively. The Rayleigh length in both directions is given for a medium of refractive index n by

$$z_{Rx,y} = \frac{n\pi w_{0x,y}^2}{\lambda} \quad (4.6)$$

Typically, the Rayleigh length is significantly larger than the focal beam width. Therefore, the cross section of the focal volume will be elliptically shaped. Since the creation of modifications in fused silica is a threshold process, with modifications occurring wherever the laser intensity is high enough, the shape of the focal volume will determine the shape of the waveguide. If we are assuming that the Gaussian beam is translated in x-direction during inscription, then the cross section of the waveguide will be shaped by the y-z-plane of the intensity distribution, leading to elliptically shaped waveguides. As an example, a calculated intensity distribution for

a typical Gaussian beam for $x = 0$ (y - z -plane) is given in figure 4.3a. The measured focal spot (x - y -plane) is shown in figure 4.3b.



(A) Calculated axial intensity distribution (y - z -plane). (B) Measured focal intensity distribution (x - y -plane).

FIGURE 4.3. Intensity of Gaussian beam of wavelength $\lambda = 515$ nm focused with an NA of 0.4, normalized to 1.

To achieve circular symmetric waveguides, an ideal intensity distribution in the focus would be an ellipsoid with a circular symmetric cross section in the y - z -plane. To come closer to this intensity distribution, a cylindrical telescope is used to increase the inscription beam size in only one direction, creating an elliptical beam. In the given setup, a magnification of 3 is chosen for the cylindrical telescope. Hereby, the inscription objective will be filled in x -direction, which is the scanning direction. The cylindrical telescope replaces the formerly used spherical telescope, which had widened the beam in both the x - and y -direction.

The numerical aperture NA of a system in air is given by [18]

$$NA = \sin(\alpha), \quad (4.7)$$

assuming a refractive index $n \approx 1$ and a half opening angle α . This can be rewritten in small angle approximation ($\sin \alpha \approx \tan \alpha$) using the aperture D and the effective focal length f of the objective via [178]

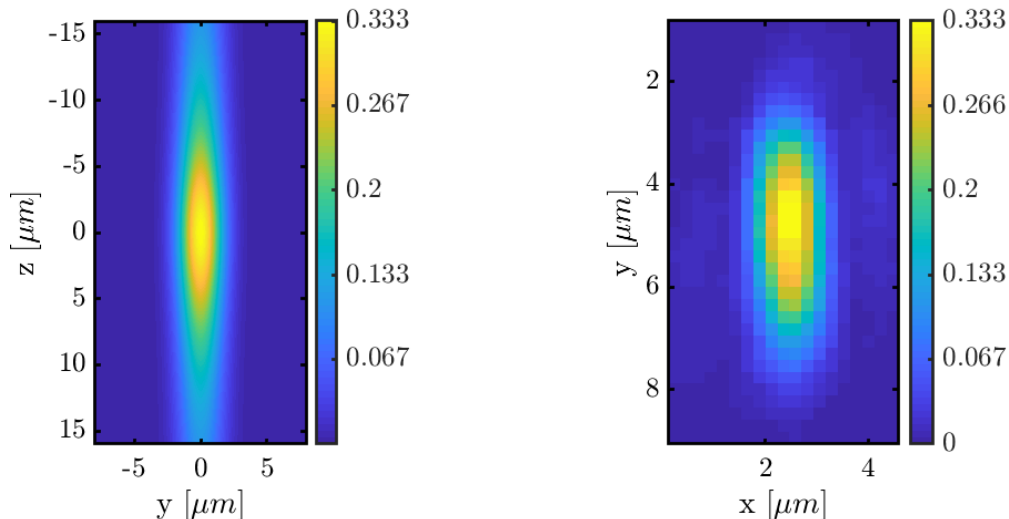
$$NA = \sin\left(\arctan\left(\frac{D}{2f}\right)\right) \approx \frac{D}{2f}. \quad (4.8)$$

4.3. WAVEGUIDE WRITING WITH ELLIPTICALLY SHAPED BEAMS

Thus, if the used aperture D is changed by a factor of f_{fill} , the numerical aperture will also change by this factor. The beam waist w_0 , which can be estimated in paraxial approximation using the numerical aperture via

$$w_0 \approx \frac{2\lambda}{\pi NA}, \quad (4.9)$$

will therefore approximately change by a factor of $1/f_{fill}$. By calculating the intensity distribution according to equation (4.4) whilst considering the reduced beam waist in one direction, a slightly different intensity distribution evolves, as illustrated in figure 4.4a, where a filling factor of $f_{fill} = 1$ in x-direction is assumed, and a filling factor of $f_{fill} = 1/3$ in y-direction.



(A) Calculated axial intensity distribution (y - z -plane). (B) Measured focal intensity distribution (x - y -plane).

FIGURE 4.4. Elliptically shaped Gaussian beam of wavelength $\lambda = 515$ nm focused with an NA of 0.4. The figures are normalized to the theoretical maximum value of figure 4.3a.

From figure 4.4a it becomes apparent that using elliptic beam shaping, the length difference between z - and y -direction of the focal volume can be reduced. The method was employed for the experiments described in section 5.3 by using a Galilean telescope made of cylindrical lenses with focal lengths of -50 mm and 150 mm, so with a ratio of 1:3. Therefore, the focal intensity distribution should correspond to the distribution given in figure 4.4a. The measured corresponding focal intensity cross-section in the x - y -plane is given in figure 4.4b, showing the corresponding elliptical shape. The $1/e^2$ focal width in x-direction is (1.9 ± 0.2) μm and in y-direction is (5.7 ± 0.2) μm . It should be noted that due to the stretching of the focus

in the y -direction also the peak intensity is reduced by a factor of 3. A study showing the obtainable waveguides with this setup is given in section 4.4.

For further experiments, the beam shaping method using the cylindrical Galilean telescope can still be improved. As can be clearly seen from figure 4.4a, the axial intensity distribution in the focal volume is still far from circular symmetric. The focal volume cross section can be shaped to be more circular symmetric by using an anamorphic zoom system. The idea is to not only expand one transverse dimension of the writing beam to fill the focusing objective (x -direction), but to simultaneously decrease the beam diameter in the other dimension (y -direction) by a continuously adjustable zoom factor. The anamorphic zoom system was designed by Prof. Herbert Gross (head of the optical design group at the Institute of Applied Physics, Jena). It consists of four lenses, the outer two lenses being spherical and the inner two lenses being cylindrical. The positions of the outer two lenses are fixed at a 50 cm distance, while the inner two cylindrical lenses can be moved. The positions of the movable lenses are coupled, meaning that when moving lens 2, lens 3 also has to be adjusted accordingly, to achieve the desired telescope output. Depending on the position of the inner two lenses, the diameter of the beam cross section in y -direction is varied. A sketch of the system is given in figure 4.5.

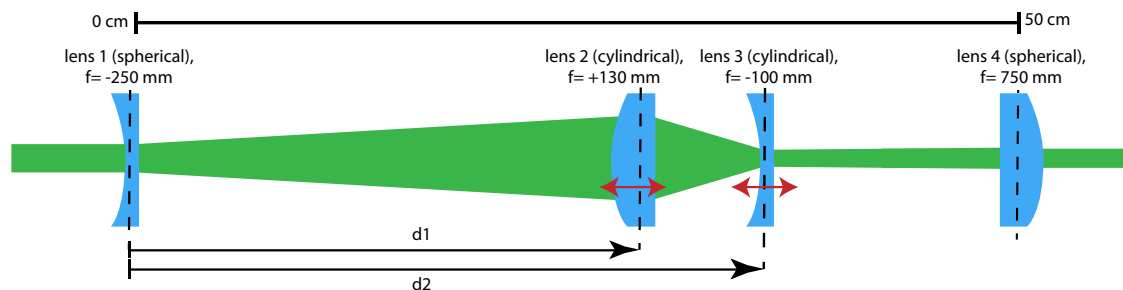


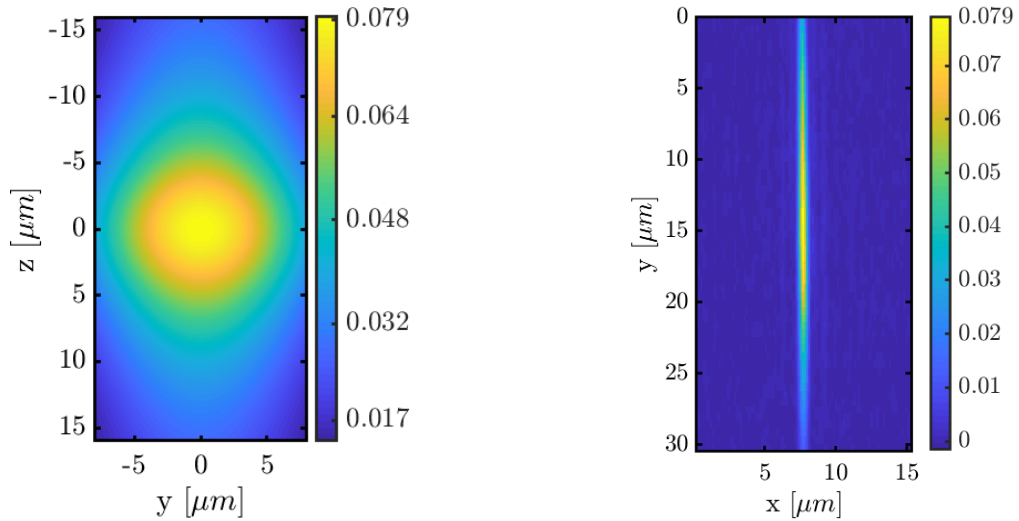
FIGURE 4.5. Sketch of the anamorphic zoom system used to shape the beam for low birefringence waveguides. The laser propagates from left to right.

Because of the beam parameter product ($w\theta = 4\lambda/\pi$, with w being the beam waist, θ the divergence and λ the wavelength [179]), a strongly decreased diameter of the laser beam in one direction will inevitably prevent the beam from staying collimated. The design of the telescope was based on ray-optics which did not account for this effect. Therefore, to choose suitable positions of the inner two lenses, a camera temporarily replaced the focussing objective in the writing setup (figure 3.1). Using this camera, the beam diameters in x - and y -direction were observed when changing the position of the inner two lenses of the anamorphic zoom system. The achievable beam ratios for some of the lens positions are listed in table 4.1.

4.3. WAVEGUIDE WRITING WITH ELLIPTICALLY SHAPED BEAMS

TABLE 4.1. Influence of lens positioning on laser beam cross-section in the objective lens plane. Distances d_1 and d_2 are defined in figure 4.5.

No.	distance d_1 [cm]	distance d_2 [cm]	measured cross section ratio
1	11.5	20	1:7.7
2	23.5	31	1:11.6
3	33.8	40	1:14.4
4	39	44.5	1:16.5



(A) Calculated axial intensity distribution (y - z -plane). (B) Measured focal intensity distribution (x - y -plane).

FIGURE 4.6. Gaussian beam of wavelength $\lambda = 515$ nm, reshaped with the anamorphic zoom system to an elliptical beam, focussed with an NA of 0.4. The figures are normalized to the theoretical maximum value of figure 4.3a.

When using the smallest measured cross section ratio of 1 : 16.5, the intensity distribution can be calculated to look as depicted in figure 4.6. The intensity distribution in figure 4.6a is clearly the most spherical symmetric when comparing it with figures 4.4a and 4.3a. At the same time, the maximum intensity is significantly decreased due to the larger spot area, indicating that higher pulse energies are required to obtain material modifications with this beam shape. An image of the focal intensity distribution is given in figure 4.6b. The measured $1/e^2$ focal diameters are $(1.9 \pm 0.3) \mu\text{m}$ in x - and $(18.6 \pm 0.3) \mu\text{m}$ in y -direction. How this setup improves the waveguide writing is described in section 4.5.

4.4. Suitable parameters for writing waveguides with a cylindrical Galilean telescope

In this section it will be studied to what extent it is possible to obtain low birefringent, high transmission FLDW waveguides using the cylindrical beam shaping described in section 4.3. Several dependencies will be investigated and the resulting waveguides will be analyzed in terms of birefringence and transmission.

4.4.1. Influence of pulse energy on waveguide losses and birefringence.

The initial parameter study is a pulse energy scan, where the fixed parameters are based on the results in section 4.2. The repetition rate was set to 1 MHz, the pulse duration to 300 fs, the scanning velocity to 100 mm min^{-1} and the writing depth was $150 \mu\text{m}$ below the surface. The inscription laser polarization was in writing direction. The modification threshold was found at $0.09 \mu\text{J}$ pulse energy, however, for the modification to guide light of wavelength 633 nm or 808 nm, a minimal pulse energy of $0.10 \mu\text{J}$ was required. All tested modifications with higher pulse energies did guide both wavelengths. Pulse energies up to $0.13 \mu\text{J}$ were tested. A transmission microscope image of the end facets of the waveguides is shown in figure 4.7. In this image it can be seen that with rising pulse energy (from left to right), the modifications become increasingly elongated. Assuming that this is caused by an elongated refractive index profile, this is an indicator for increasing birefringence of the modifications. The modifications created with $0.09 \mu\text{J}$ also look significantly less bright compared to all other modifications, which supports the observations that some wavelengths in the visible range are not guided by this modification. When comparing figure 4.7 to the facets of the modifications written with a spherical Galilean telescope in figure 4.1, it becomes apparent that the parameter window has increased significantly by changing to a cylindrical Galilean telescope.

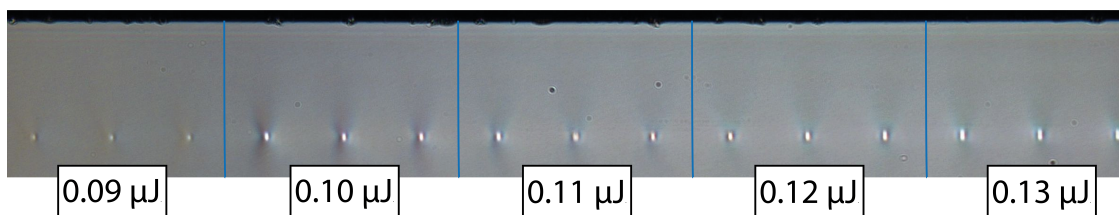


FIGURE 4.7. Microscope image of waveguide facets created with a 1:3 cylindrical telescope at 1 MHz repetition rate, 100 mm min^{-1} scanning speed and increasing pulse energy. The spacing between the waveguides is $100 \mu\text{m}$. The pulse energies range from $0.09 \mu\text{J}$ to $0.13 \mu\text{J}$.

To quantify the performance of the waveguides in figure 4.7, both their losses and their birefringence were determined using the characterization setup (figure 3.2)

4.4. SUITABLE PARAMETERS FOR WRITING WAVEGUIDES WITH A CYLINDRICAL GALILEAN TELESCOPE

with 808 nm characterization wavelength. The obtained values are plotted in figure 4.8. The left axes shows the measured losses (red) and the right axis gives the measured retardation (blue). All values are averages over three waveguides, with the measurement variation given by the error bar.

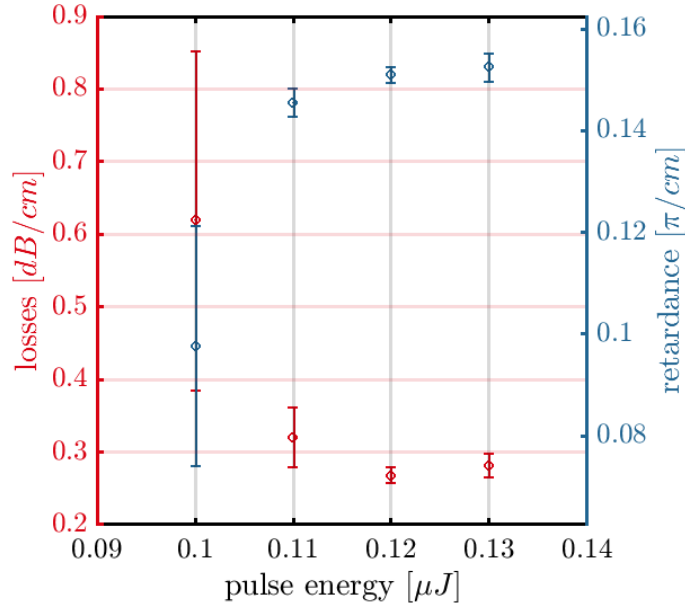


FIGURE 4.8. Losses and optical retardation of waveguides created with a 1:3 cylindrical telescope at 1 MHz repetition rate, 100 mm min^{-1} scanning speed and varying pulse energy for 808 nm characterization wavelength.

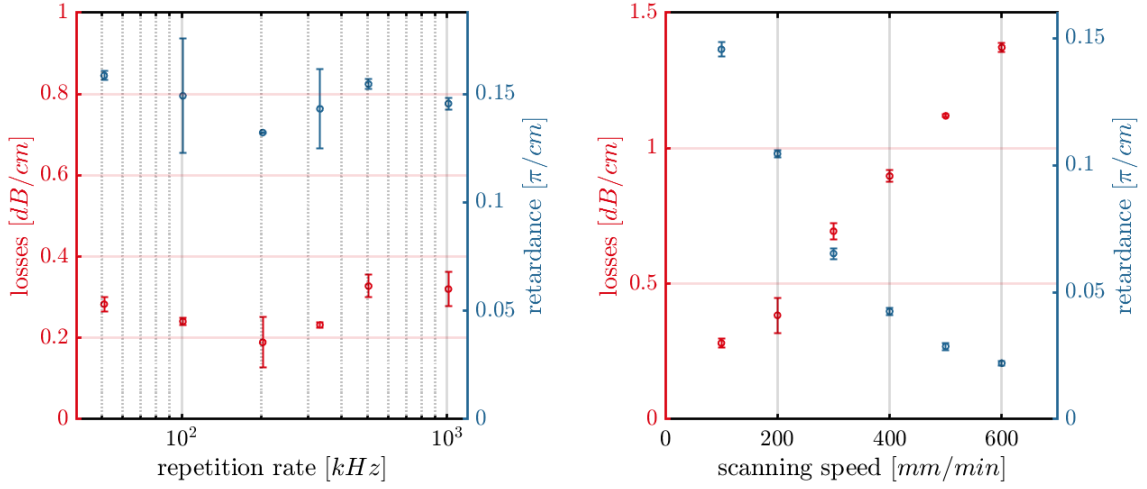
The first thing that becomes apparent when looking at the data points in figure 4.8 is that the error bars for the waveguides created with $0.10 \mu J$ are significantly larger than the error bars of the other waveguides, indicating that close to the modification threshold the properties of the waveguides fluctuate strongly. Therefore, this is not a convenient set of parameters when reliable, reproducible waveguide properties are desired. For higher pulse energies, the retardation slightly increases with the pulse energy, showing retardations around $0.15\pi \text{ cm}^{-1}$. The losses first decrease with increasing pulse energy, then stagnate for waveguides written with $0.12 \mu J$ and $0.13 \mu J$ at $(0.28 \pm 0.02) \text{ dB cm}^{-1}$. Therefore, the waveguides used in section 5.3 were written with $0.12 \mu J$ pulse energy. The measured losses are already significantly lower than the losses reported in figure 4.2, however, the measured retardations are still too high for application as polarization maintaining waveguides. Therefore, in the next section the influence of repetition rate and the pulses per spot will be investigated, to study whether with a more suitable repetition rate, the birefringence of the waveguides may be reduced.

4.4.2. Influence of repetition rate and pulses per spot on waveguide losses and birefringences. To investigate how birefringence and losses depend on repetition rate without changing the number of pulses per spot, the scanning velocity has to be adjusted along with the repetition rate. The analysis of the influence of the repetition rate was made at a constant pulse energy of $0.11 \mu\text{J}$, which has been proven in figure 4.8 to be far enough above the modification threshold to give reliable waveguide properties. The tested repetition rates ranged from 50 kHz to 1000 kHz. The pulse duration was set to 300 fs, the writing polarization was in scanning direction. The pulse number was fixed at 1140 pulses per spot by adjusting the writing velocity for every scan. This corresponds to a scanning speed of 100 mm min^{-1} at a repetition rate of 1 MHz, which is the setting that was used in section 4.4.1. All waveguides were measured with 808 nm wavelength laser light. A plot of the measured losses and birefringences is given in figure 4.9a. The measured retardations range around $0.15\pi \text{ cm}^{-1}$, while the losses range from 0.12 dB cm^{-1} to 0.36 dB cm^{-1} . Neither the losses nor the retardations show a clear dependency on the repetition rate, making it possible to freely choose a repetition rate as desired. For combining waveguides with nanogratings it is most useful to choose a repetition rate that is also beneficial for nanograting inscription, to minimize the likeliness of inscription mistakes when changing between writing waveguides and writing nanogratings. Therefore, most waveguides in this thesis will be written with 100 kHz repetition rate.

The final parameter to be investigated is the dependency of birefringence and loss properties of waveguides on the numbers of pulses per spot during inscription. For this purpose, waveguides were inscribed at $0.13 \mu\text{J}$ pulse energy with 1000 kHz repetition rate. The scanning speed was varied from 100 mm min^{-1} to 600 mm min^{-1} , corresponding to 1140 to 190 pulses per spot, respectively. The retrieved retardations and losses of the waveguides are plotted in figure 4.9b.

The retardations in figure 4.9b range from $0.02 \pi/\text{cm}$ to $0.16 \pi/\text{cm}$, decreasing with increasing scanning speed. This indicates, that for writing low birefringence waveguides, decreasing the pulses per spot during inscription might be a good strategy. However, when looking at the losses of these waveguides, which range from 0.28 dB cm^{-1} to 1.4 dB cm^{-1} , it becomes clear that these increase with the scanning speed, showing that the low birefringence of waveguides written at higher speeds comes at the cost of higher losses. Nevertheless, the waveguides used in section 5.3 were written with 600 mm min^{-1} to minimize the waveguide birefringence. In the original publication presenting the astigmatic beam shaping for waveguide writing [54], the authors claimed that by slightly defocusing the telescope, more circular symmetric waveguides with reduced birefringence can be achieved.

4.4. SUITABLE PARAMETERS FOR WRITING WAVEGUIDES WITH A CYLINDRICAL GALILEAN TELESCOPE



(A) Waveguides created with different repetition rates and a fixed number of pulses per spot.

(B) Waveguides created with different scanning speeds at 1 MHz repetition rate, corresponding to a change in pulses per spot.

FIGURE 4.9. Losses and optical retardation of 4 cm long waveguides measured with 808 nm laser light. All measurement values are averages over three waveguides written under the same conditions. Error bars indicate the variation between the waveguides. The inscription beam was shaped using a 1:3 cylindrical telescope.

To investigate this, the second lens of the cylindrical telescope was mounted on a positioning stage. The second lens was moved from -0.75 mm to 0.75 mm away from the original position in 0.25 mm increments. For each position, a waveguide was inscribed. The waveguide parameters were 1000 kHz repetition rate, 0.15 μ J pulse energy and 250 mm min^{-1} scanning speed, with the laser polarization in the scanning direction. A transmission microscope image of the end facet is given in figure 4.10. Whilst in the original publication, the authors claim to see a change of the morphology of the waveguides when the second telescope lens is moved by 300 μ m, no such change in morphology is visible in figure 4.10.

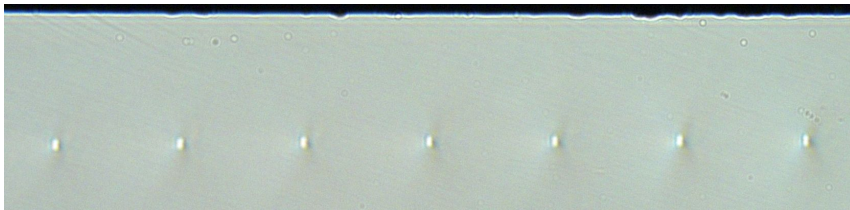


FIGURE 4.10. Facets of waveguides created with a 1:3 cylindrical telescope when the second lens was shifted by -750 μ m to 750 μ m. The spacing between the waveguides is 150 μ m.

To study whether any influence of the waveguide's birefringence on the shift of the second lens can be determined, the birefringence of all 7 waveguides was measured

in terms of optical retardation. The results are plotted in figure 4.11. The measured retardations all range between $0.11 \pi/\text{cm}$ and $0.14 \pi/\text{cm}$. The minimum retardation can be seen for a lens shift of -0.25 mm , however it is only 4% lower than the value obtained for a lens shift of 0. Any other shift only leads to an increase of the retardation compared to the case of 0 lens shift. When comparing figure 4.11 with figure 4.9b, it becomes apparent that the numbers of pulses per spot have a significantly higher influence on the overall retardation than the tested shift of the telescope lens. To conclude, the strategy of shifting the second lens of the cylindrical telescope does not yield satisfactory results for lowering the birefringence of the waveguides. Therefore, a new strategy is required if the birefringence of the waveguides is to be decreased. This new strategy is to further reduce the asymmetry of the induced refractive index modifications by using an anamorphic zoom system. The results obtained with this setup are presented in the following section 4.5.

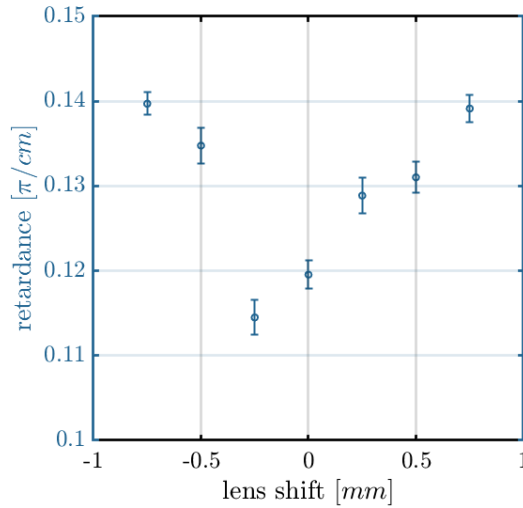


FIGURE 4.11. Retardations of waveguides created with a 1:3 cylindrical telescope at 1 MHz repetition rate, 250 mm min^{-1} scanning speed and $1.5 \mu\text{J}$ pulse energy when the second lens of the cylindrical telescope is shifted. The error bars represent the 95% confidence intervals of the fits

4.5. Improved waveguide performance using an anamorphic zoom system

To inspect the possible improvement in waveguide performance, waveguides were inscribed with a beam that was shaped according to setting number 4 in table 4.1 using the anamorphic zoom system, leading to a cross section ratio of 1:16.5. Since the goal is to compare the obtained performance with waveguides from section 4.4, comparable inscription parameters should be chosen. Low birefringence waveguides

4.5. IMPROVED WAVEGUIDE PERFORMANCE USING AN ANAMORPHIC ZOOM SYSTEM

were, for example, given in figure 4.9b at 600 mm min^{-1} , created with a repetition rate of 1000 kHz . To achieve comparable pulses per spot with the focus of the anamorphic zoom system, the same repetition rate and scanning speed can be chosen, because both foci were measured to have the same $1/e^2$ focal width in scanning direction within the measurement tolerance (see figure 4.4b and 4.6b), since both telescopes fill the inscription aperture in that direction. At the same time, due to the significantly decreased focal intensity due to the beam shaping with the anamorphic zoom system, the pulse energy was increased to $0.54 \mu\text{J}$. However, damage at the top surface was observed when inscribing waveguides under these conditions. Since ablation is increased by the thermal accumulation, one way to avoid this is to move to lower repetition rates [180]. Reducing the repetition rate to 100 kHz and at the same time reducing the writing speed to 60 mm min^{-1} (thus keeping the pulses per spot constant) enabled the fabrication of waveguides without ablating the sample's surface. Waveguides written with these parameters showed an optical retardation of $\phi_{norm} = (0.020 \pm 0.003) \pi/\text{cm}$ and losses of $(0.15 \pm 0.01) \text{ dB cm}^{-1}$. The retardation corresponds to a birefringence of $\Delta n = \frac{\phi_{norm} \cdot \lambda}{2\pi} = 8 \times 10^{-7}$. Compared to the values in figure 4.9b at 600 mm min^{-1} , this is a decrease of losses by 89% at comparable birefringence values. This displays the benefit of the anamorphic zoom system as a beam shaping technique for FLDW. A mode field of such a waveguide, along with an according refractive index change profile, is given in figure 4.12. The refractive

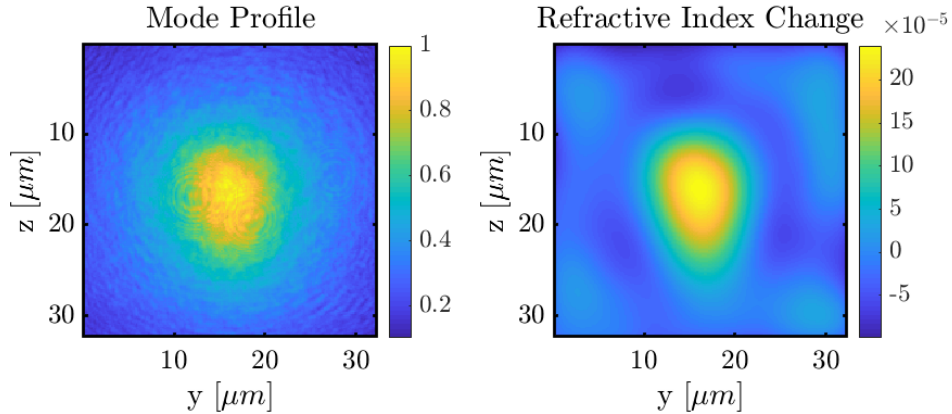


FIGURE 4.12. Mode field and refractive index change profile of a waveguide created with the anamorphic zoom system

index change profile was retrieved numerically by solving the inverse Helmholtz equation as presented in [181]. The full width half maximum size of the mode field is $(8.6 \pm 0.2) \mu\text{m}$ in y and $(9.8 \pm 0.2) \mu\text{m}$ in z .

To conclude, it was shown in this section that for the given writing laser, low birefringent waveguides with high transmission values can be achieved when using spatial beam shaping techniques. The best results were obtained with an anamorphic

zoom system that allowed a cross section ratio of the writing beam of 1 : 16.5. When comparing the birefringence and the losses of the best waveguides with results reported in literature of $\Delta n = 1 \times 10^{-6}$ [148, 152], it can be said that the birefringence was further reduced by approximately 20%. The lowest so far reported waveguide loss in fused silica of 0.1 dB cm^{-1} at a wavelength of $1.55 \mu\text{m}$ [170] has not quite been matched. It has to be taken into account, however, that one of the main loss mechanisms in waveguides is Rayleigh scattering [83], which increases for shorter wavelengths. Since the waveguides in this thesis were characterized with light of 808 nm wavelength, this justifies the difference.

Waveguides are only one of the modifications that can be created with FLDW. The next section will focus on the second modification type, namely nanogratings, which will be used to add integrated waveplates to the waveguides.

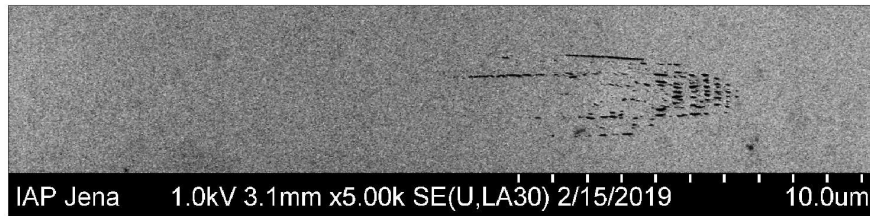
Polarization Control Based on Nanogratings

Nanogratings, also known as type II modifications, are a modification type that occur in FLDW at intermediate pulse energies when many pulses are applied onto one spot. In this thesis, the birefringence of nanogratings is exploited to add localized polarization manipulation elements to FLDW waveguides. To do this, firstly, the presence of nanogratings will be confirmed by showing according scanning electron microscope images. Secondly, the dependency of the nanograting properties on the inscription properties will be studied in detail. Nanogratings will then be combined with waveguides, where they will act as integrated waveplates. By choosing suitable parameters, these combinations can be used to perform quantum operations, which will be demonstrated by characterizing the structures using single photons. Finally, further tuning opportunities of nanogratings using novel beam shapes will be explored.

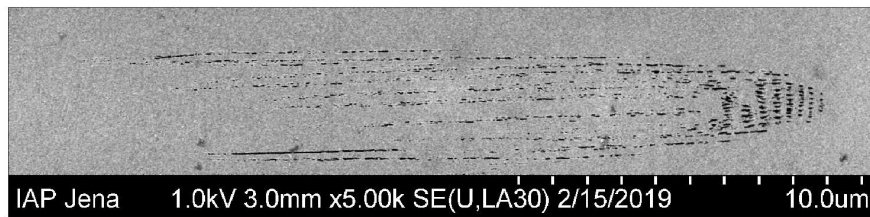
5.1. Scanning electron microscope images of modifications

If nanogratings are to be used in experiments, it has to be ensured that the structures under observation are in fact nanogratings. The first observations of nanogratings were due to their extraordinary properties, which is their scattering properties and their birefringence [72, 73, 93], with the amount of retardation increasing with pulse energy and the optical axis being given perpendicular to the polarization direction. Therefore, if highly birefringent modifications in fused silica can be achieved, and it can be seen that their optical axis rotates with the inscription polarization, it is very likely that these modifications are nanogratings. However, the naming of nanogratings is based on their nanoscopic structure. The only way to be sure that a given structure is a nanograting is to show its grating-like features. Due to their small feature sizes, nanogratings created by visible wavelengths cannot be resolved in an optical microscope. Other imaging techniques like the scanning electron microscope (SEM) have to be used. For this purpose, modification tracks were written with 5 mm min^{-1} , 100 kHz repetition rate, 300 fs pulse duration and three different inscription pulse energies (0.25 μJ , 0.5 μJ and 0.9 μJ). The focusing objective was a 20x plan apochromat Olympus objective and before entering the objective, the beam was shaped using the cylindrical telescope described in section 4.3. The glass samples were polished to bring the nanogratings to the surface and then etched

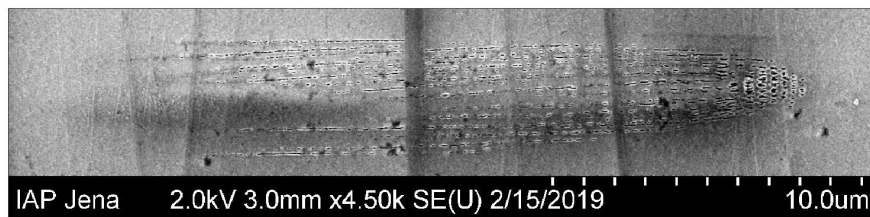
using 1% hydrofluoric acid (HF) for 90 s. The resulting SEM images are shown in figure 5.1, with each subfigure showing a different inscription pulse energy, rising from top to bottom. The laser travels from left to right. All displayed modifications show grating features, proving that they are nanograting modifications. The length of the modification increases with the inscription pulse energy. The typical nanograting structure exhibits two regions with different periodicities. The first region consists of smaller voids that form layers. With increasing pulse energy, a second region consisting of mainly elongated lines becomes apparent, with no layer formation along the propagation direction visible. The orientation of all grating planes is perpendicular to the writing polarization.



(A) Inscription pulse energy of 0.25 μJ .



(B) Inscription pulse energy of 0.5 μJ .



(C) Inscription pulse energy of 0.9 μJ .

FIGURE 5.1. Cross sections of nanogratings taken via SEM. The images were cropped to the region of interest, their contrast was improved using Matlab's `imadjust` function and they were filtered using a low-pass Wiener filter. The laser propagates from left to right; the writing direction is into the image plane and the laser polarization was parallel to the image plane.

For this thesis, this will be taken as the confirmation that the obtained structures are in fact nanogratings. Most nanogratings in this thesis were never examined

using SEM, since for this thesis the properties of interest are not the microscopic structure but rather the macroscopic optical properties. Instead, it was assumed that a produced structure is a nanograting, if it exhibits birefringence, of which the optical axis can be turned by rotating the inscription polarization.

5.2. Parameter dependencies

To make use of nanograting properties, their parameter dependencies have to be well controlled. For this purpose, the influence of various writing parameters, as well as various beam shapes on the nanograting properties were investigated. While the general dependencies of nanogratings on parameters have been studied before, the study in this thesis is nevertheless required to be able to achieve tailored birefringence properties for the desired waveplates. Additionally, previous studies have not paid attention to the parameter dependency of the dichroism of the nanogratings, which is included here.

5.2.1. Pulse energy and pulses per spot. Firstly, the influence of pulse energy and pulses per spot on the nanograting parameters is analyzed. For this purpose, various nanogratings were written with different pulse energies and writing velocities. Since the scanning velocity v is related to the number of pulses per spot N_p via

$$N_p = \frac{f_{rep} \cdot d}{v}, \quad (5.1)$$

changing the scanning velocity at a constant repetition rate f_{rep} means changing the number of pulses per spot. The focal spot size is denoted as d in the equation. In this experiment, the telescope of choice in the inscription setup (given in figure 3.1) was a spherical Galilean telescope, as described in section 3.1. The nanogratings were positioned approximately 150 μm below the surface and written line by line to form (0.5×0.5) mm squares. The line separation was set to 2.8 μm (corresponding to the $1/e^2$ -focal spot size), while the repetition rate during inscription was 100 kHz. The pulse energy was varied between 0.1 μJ to 0.8 μJ . By measuring the modified areas using the characterization setup described in section 3.2, the dependency of retardation, losses and dichroism on pulses per spot, as well as pulse energy can be mapped. This is given in figure 5.2. The probing laser of 808 nm was passing through the structure in the same direction that the writing laser inscribed the structures.

Figure 5.2a depicts the dependency of the optical path difference on the number of pulses per spot and the pulse energy. It can be seen that in agreement to the known properties of nanogratings given in section 2.3.2.2, the optical path difference of the structures increases mainly with the pulse energy. The number of pulses per spot also has some influence on the optical path difference, with more pulses per

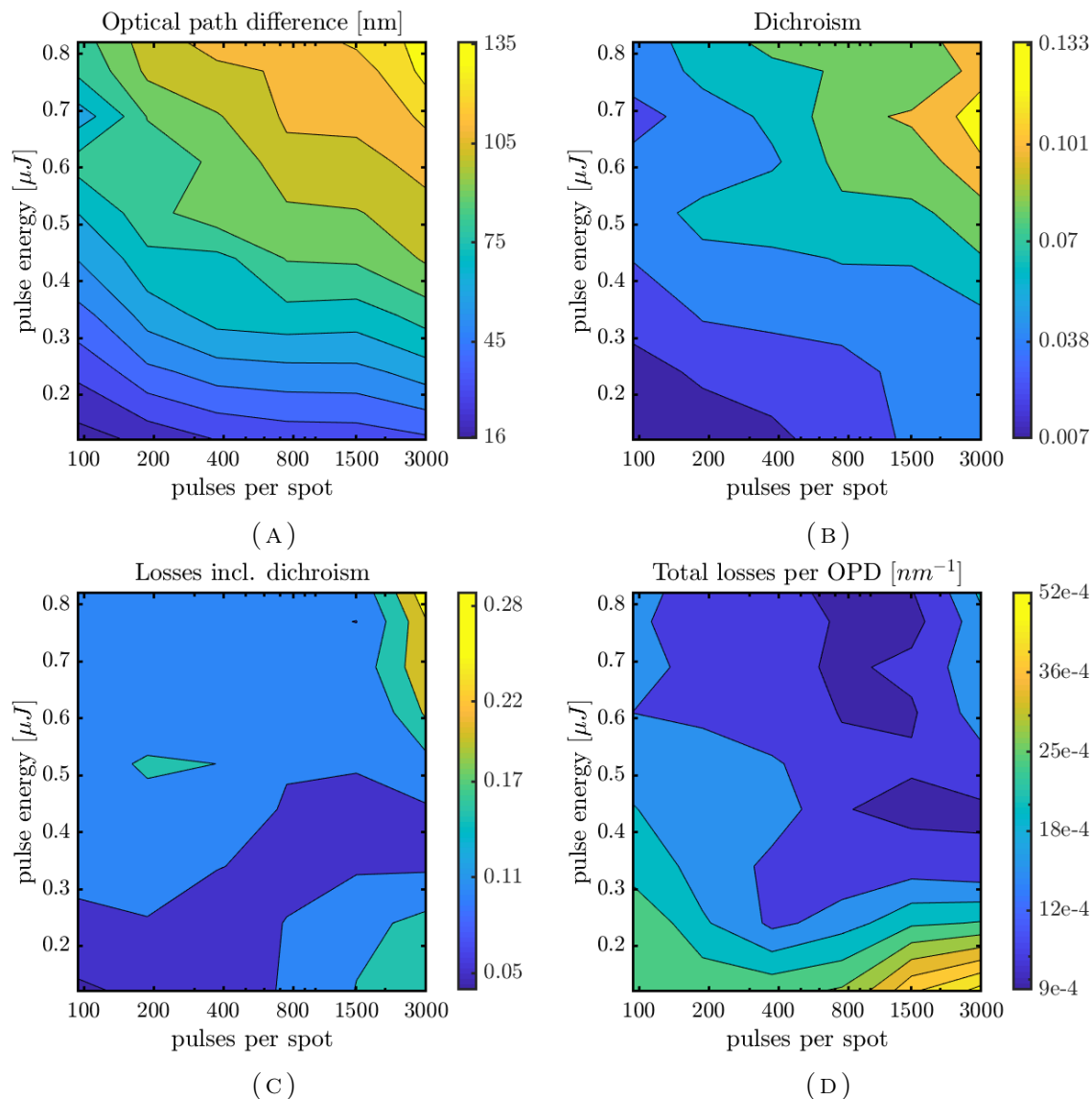


FIGURE 5.2. Properties of nanograting structures written with a spherical Galilean telescope, evaluated using the characterization setup.

spot leading to higher optical path differences. The maximal achievable optical path difference of the structures for the given parameters is 135 nm. Figure 5.2b shows the dependency of the nanogratings' dichroism on the number of pulses per spot and the pulse energy. It can be seen that the dichroism of the structures ranges up to 13%, with highest values of dichroism occurring at the highest number of pulses per spot (3000 pulses per spot) and around 0.6 μJ to 0.8 μJ .

The overall losses are given in figure 5.2c, showing a rather uniform distribution with most values ranging around 12%. The losses are retrieved by comparing the transmission of modified regions with the transmission through non-modified regions. Therefore, Fresnel losses have already been removed. The overall losses start to

5.2. PARAMETER DEPENDENCIES

increase for ≥ 1500 pulses per spot, rising up to 25% at 3000 pulses per spot and 0.8 μJ pulse energies. For many applications, it is desired to reach a certain phase retardation with minimal losses. For this, finding the minimal losses per retardation is of interest, which is why the total losses (including dichroism) per *OPD* in inverse nanometers is given in figure 5.2d as a figure of merit. They range on the order of $9 \times 10^{-4} \text{ nm}^{-1}$ to $4.8 \times 10^{-3} \text{ nm}^{-1}$. The lowest values are found at pulse energies of $\geq 0.4 \mu\text{J}$, especially for 800 to 1500 pulses per spot.

By selecting according values from figure 5.2, the Mueller matrix of a nanograting can be retrieved when modelling the nanogratings as diattenuating linear retarders. For example, a nanograting inscribed using 0.8 μJ pulse energy and 750 pulses per spot has an *OPD* of 116 nm, which for light of 808 nm wavelength corresponds to a phase delay of 0.29π , and a dichroism of 9%. The overall losses of the structure are given at 10%, making 1% the polarization independent losses. Thus, the resulting Mueller matrix $\overset{\leftrightarrow}{M}$ will be

$$\overset{\leftrightarrow}{M} = \begin{pmatrix} 0.945 & 0.045 & 0 & 0 \\ 0.045 & 0.945 & 0 & 0 \\ 0 & 0 & 0.585 & 0.634 \\ 0 & 0 & -0.634 & 0.585 \end{pmatrix}. \quad (5.2)$$

As mentioned in section 3.2, an alternative to the characterization setup is the commercial polarimeter. The structures were measured using this device. The results can be seen in figure 5.3. The optical path difference measured with the commercial polarimeter is given in figure 5.3a. It generally shows similar dependencies to the ones given in figure 5.2a: the optical path difference rises with increasing pulse energy and increasing pulses per spot. At the same time, the maximum optical path difference measured with the commercial polarimeter is slightly higher than the one measured with the characterization setup. The differences between the two measurements are plotted in 5.3b. The average difference between the two measurements is around 8 nm. Interestingly enough, the difference in *OPD* measurements is not highest for the cases where the highest dichroism was measured (which is not possible with the commercial polarimeter), but rather at low pulse energies of $\leq 0.4 \mu\text{J}$. This indicates that other factors, like dispersion due to the different probing wavelengths of the setups (587 nm and 808 nm), might weight more in this case than the error caused by neglecting dichroism. The transmission losses measured using the commercial polarimeter are given in figure 5.3c.

The losses measured using the commercial polarimeter seem to be higher than the losses measured with the characterization setup. The maximum loss value

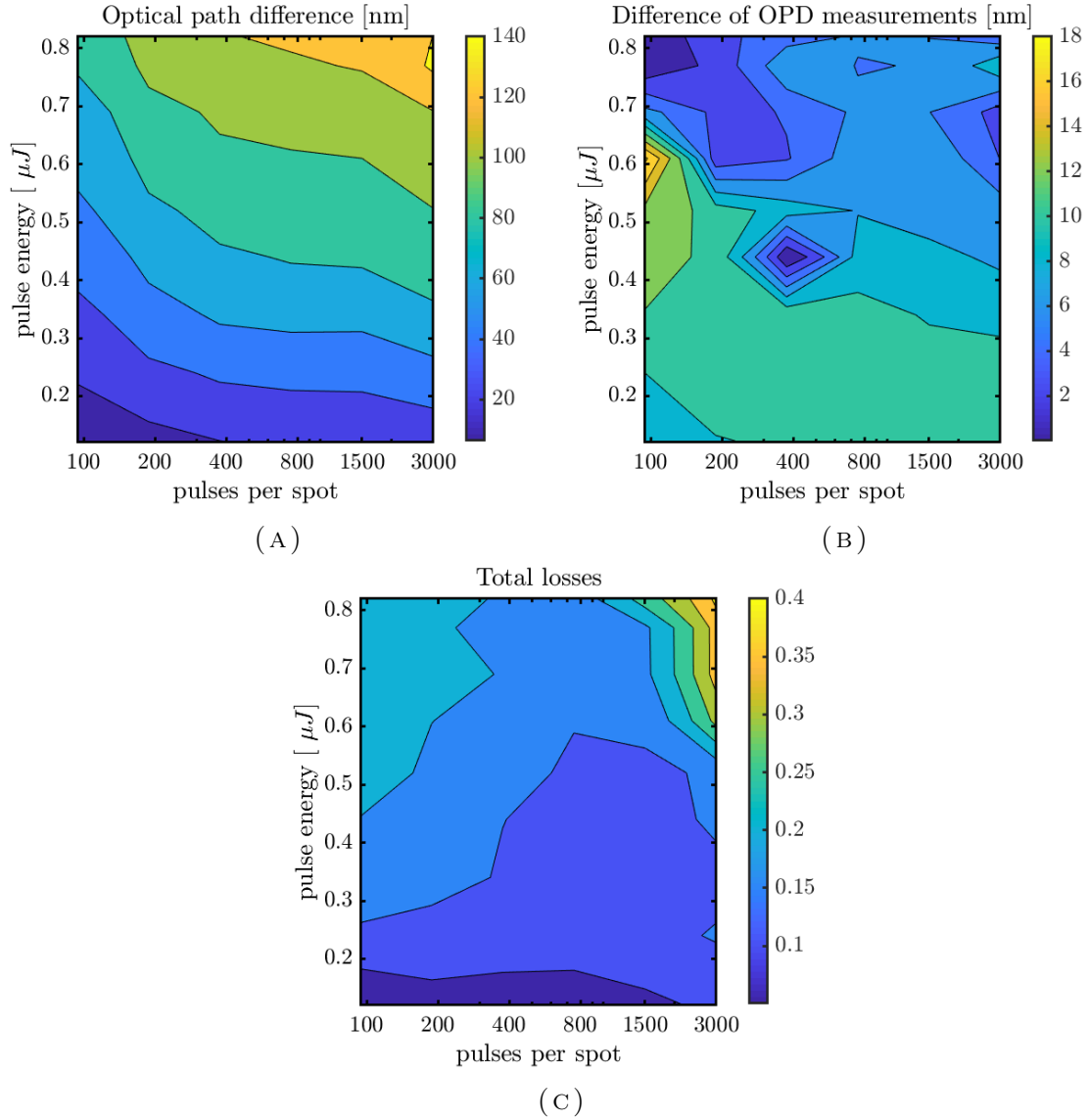


FIGURE 5.3. Measurement results acquired by the commercial polarimeter and difference to *OPD* measurement in figure 5.2a.

measured with the characterization setup at 808 nm was 28.8%, corresponding to losses of $-10 \cdot \log(1 - 0.288)\text{dB} = 1.5 \text{ dB}$. The maximum measured loss value was 41%, corresponding to $-10 \cdot \log(1 - 0.41)\text{dB} = 2.3 \text{ dB}$, which is 1.5 times higher than what was measured using the characterization setup. The reason for this might be wavelength dependant scattering. The scattering of light can be described using Mie theory (assuming spherical scattering particles), and categorized depending on the ratio between the scattered light's wavelength λ and the diameter of the scattering particle d_s [10]. For ratios $d_s/\lambda \gg 1$, scattering phenomena can be described by geometric optics, which is wavelength independent. On the other side, for ratios $d_s/\lambda \leq 0.1$, Rayleigh approximation can be used to describe the scattering phenomena [182]. The cross section of Rayleigh scattering is highly

5.2. PARAMETER DEPENDENCIES

wavelength-dependent, scaling with $1/\lambda^4$. In the regime between Rayleigh scattering and geometric optics, which is typically referred to as Mie scattering, the scattering cross sections become increasingly wavelength dependent, the smaller d_s/λ is [183]. The size of the nanogratings' period p can be roughly estimated by the refractive index of fused silica n and the inscription wavelength $\lambda = 515$ nm to amount to about $p \approx 180$ nm. The nanopores will be smaller than that, but not necessarily small enough to be classified as Rayleigh scattering. Typical nanopore diameters range around 75 nm [184]. The scattering processes therefore fall into the distinctly wavelength-dependent transition region between Mie and Rayleigh scattering.

5.2.2. Repetition rate. Not only the pulse energy and the pulses per spot can have an influence on the nanograting properties, also the temporal distance of the pulses can be of importance. To demonstrate this dependency, an investigation was made where the pulse energy and the number of pulses per spot were kept constant, while the repetition rate was changed. The pulse number per spot was kept at 500 by changing the writing velocity when changing the repetition rate, whilst the pulse energy was set to $0.8 \mu\text{J}$. The measured optical path difference and dichroism of the resulting nanograting structures are shown in figure 5.4. In the figure it can be clearly seen that as the repetition rate increases, both dichroism and optical path difference drop. This can be attributed to the fact that heat accumulation suppresses the formation of nanogratings [103].

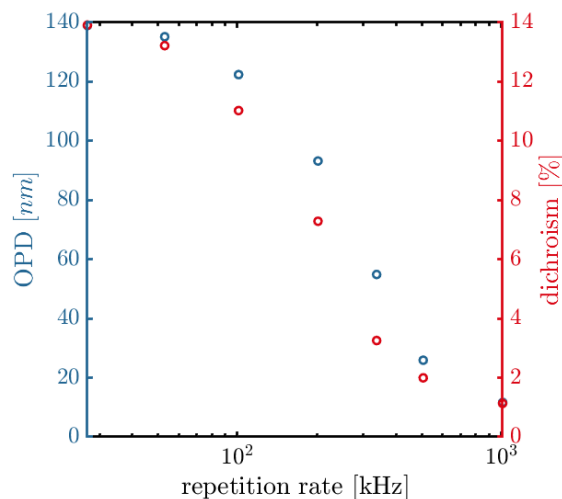


FIGURE 5.4. Optical path difference and dichroism of nanograting structures created with different repetition rates.

To reach the highest possible optical path difference for a certain number of pulses per spot and a given pulse energy, low repetition rates are to be preferred. However, lowering the repetition rate while keeping the number of pulses per spot constant

causes the processing time to increase. In this thesis, most of the time the repetition rate of choice was 100 kHz as a compromise between the retardation of the structures and the processing time.

5.2.3. Rotation of nanograting orientation. Another very important property of nanogratings is the orientation of the optical axis perpendicular to the polarization of the inscription beam. To investigate how readily the orientation of the optical axis can be controlled, nanogratings were inscribed with constant parameters, while only the orientation of the writing laser's polarization was changed. The parameters were set to 100 kHz repetition rate, 10 mm min^{-1} scanning speed, $0.94 \mu\text{J}$ pulse energy and $2.8 \mu\text{m}$ scanning line separation, leading to 1680 pulses per spot. It was confirmed that the inscription power of the laser beam remains the same for all polarization orientations. The nanograting field size was set to $0.4 \text{ mm} \times 0.4 \text{ mm}$. The measured optical path difference of these structures as determined with the characterization setup can be seen in figure 5.5. In figure 5.5a, the orientation of the optical axis of the structures is shown, which linearly follows the orientation of the laser's polarization. Figure 5.5b shows the dichroism and optical path difference of the structures when the laser's polarization is rotated. The graph shows that while the inscription polarization changes, the retardation oscillates, being lowest at around 170° and 350° inscription polarization orientation. The dichroism also oscillates, but its minima are shifted to 200° and 380° inscription polarization orientation. Both the demonstrations of the rotation of the optical axis and the dependency of the optical retardation on the inscription polarization are fundamental for creating waveplates with nanogratings, because they indicate two things: Firstly, the inscription polarization can be used to change the orientation of the gratings, secondly, other inscription parameters (for example, the pulse energy) have to be adjusted when changing the inscription polarization to keep the retardation of the waveplate the same for all waveplate orientations.

The reason why the optical retardation changes with polarization orientation remains unclear. Previous studies by Zimmermann et al. [94] indicated that an interplay between writing direction and polarization orientation might be the reason for such a behaviour. A possible explanation can be found, for example, in [185], where a dependency of the absorption process during inscription on the scanning direction is justified with an enhancement of the heat affected zone in the direction of the laser's electric field. To investigate this, the parameter scan for figure 5.5 was repeated with all parameters constant, except for the writing direction of the nanograting fields being rotated by 45° . The rotation of the optical axis with the polarization was also confirmed for this case, as shown in figure 5.6a. In figure 5.6b, the optical path difference was measured for these nanogratings and the results are compared to

5.2. PARAMETER DEPENDENCIES

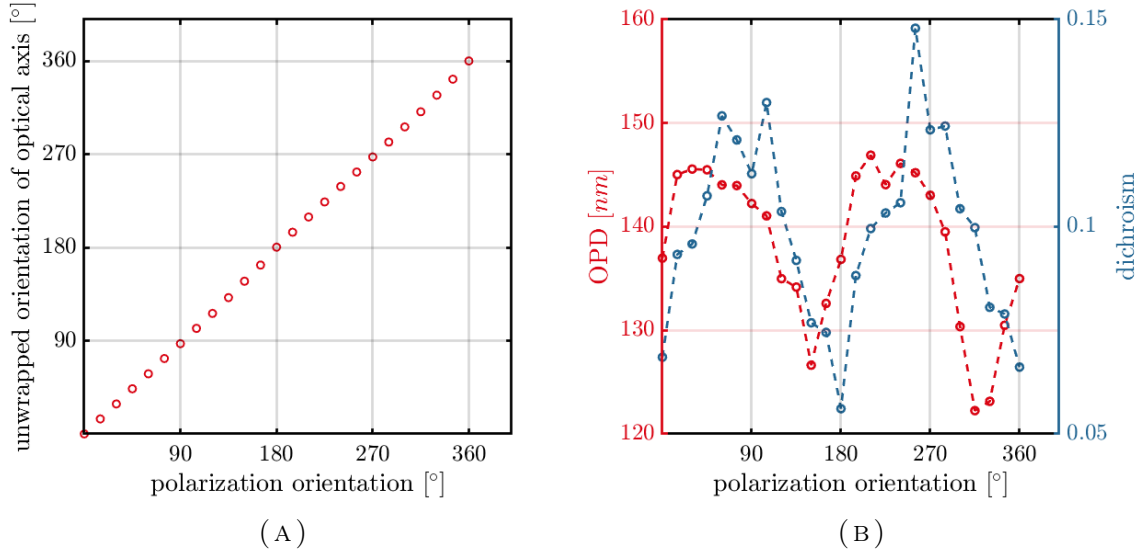
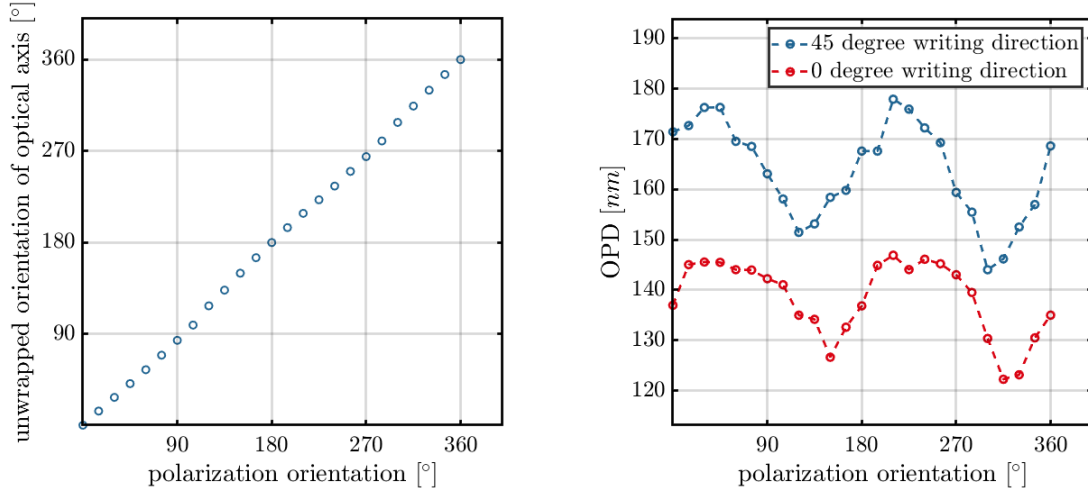


FIGURE 5.5. Optical properties of nanograting structures for different polarization orientations of the writing laser. The dashed line in subfigure 5.5b is a guide to the eye.

the optical path difference of nanogratings written with 0° writing orientation (same data as in figure 5.5).

As can be seen, both the optical path difference and dichroism values still oscillate with the change of polarization for this writing direction. However, the two graphs are not shifted by 45° , as one might expect, but instead by only 20° . This contradicts the hypothesis, that the writing direction in comparison to the polarization orientation is the only reason for the change in optical retardation. Additionally, one might notice that the optical retardation of the nanogratings written with 45° writing direction are 15% to 30% higher than the optical retardation of fields written with 0° writing direction. The reason for this remains unclear and needs to be part of further investigations outside of the scope of this thesis. One might speculate that apart from the electric field (as described in [185]), also strain from previously inscribed lines in the line-by-line inscription process influence the heat affected zone during laser inscription, thereby breaking the symmetry of the inscription process.

The nanogratings of figures 5.5 and 5.6 were then measured using the commercial polarimeter to confirm the results when the optical axis of the structures changes. The measured *OPD* is given in figure 5.7a. This figure shows that the *OPD* measured using the commercial polarimeter also oscillates. At the same time, the *OPD* values are slightly larger compared to figure 5.6b, with differences up to 20% occurring. Also, the shape of the curves as measured using the commercial polarimeter is significantly different to the shape of the curves given in figure 5.6b. To investigate whether the reason for this is that the polarimeter does not account for dichroism,



(A) Rotation of optical axis when the polarization of the inscription laser is rotated for a scanning direction of 45° .

(B) *OPD* of nanograting structures written with 0° vs. 45° writing direction. The dashed line is a guide to the eye.

FIGURE 5.6. Birefringence properties of nanograting structures written with 45° writing direction for various polarization orientations of the writing laser.

the raw data from the characterization setup (from which the results in figure 5.5 and 5.6 were derived) was fitted again, this time using a model that does not take into account dichroism. The fit equation for this case is [186]

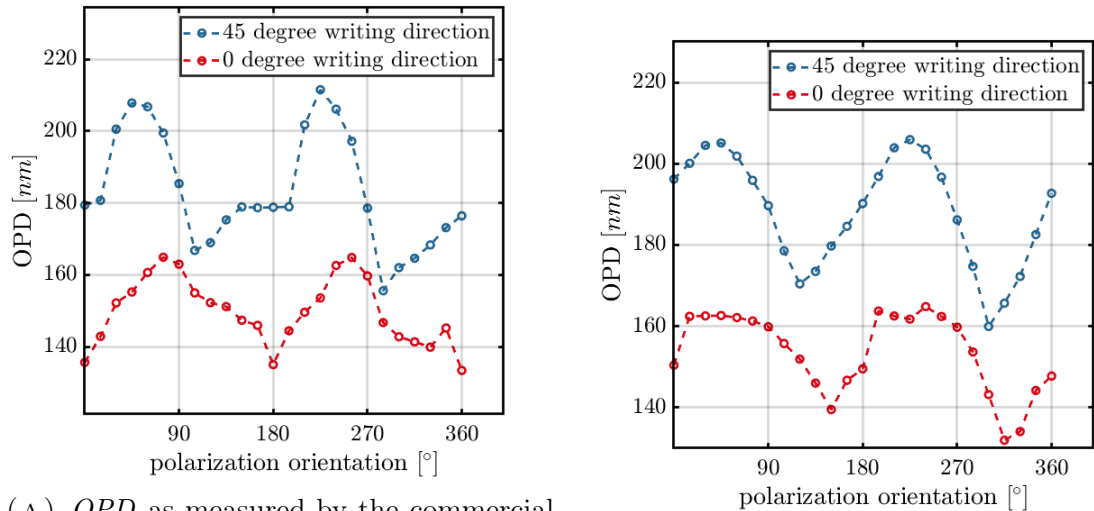
$$T_{cross}(\theta)/T_p(\theta) = (1 - \cos(\delta)) \sin^2(\theta). \quad (5.3)$$

Here $T_{cross}(\theta)$ is the transmitted power through crossed polarizers in the characterization setup (see section 3.2), $T_p(\theta)$ is the according transmitted power through parallel polarizers, θ is the input polarization orientation and δ is the optical retardance. The results are plotted in figure 5.7b.

The resulting *OPD* value ranges now match more closely, showing how neglecting dichroism can lead to an overestimation of the actual optical retardance. The shift of the minima positions still remains, indicating that this is a difference either caused by the different wavelengths used or due to other intrinsic differences of the setups. To sum things up, this shows that the commercial polarimeter can be used for a rough overview of the birefringence properties of modifications with rotated optical axes. For more precise results, however, the characterization setup has to be used.

To conclude, the results presented show that to control the properties of nanogratings, two parameters are essential: the pulse energy (as shown in figure 5.2), to control the optical path difference of the structure, and the inscription laser's polarization (as shown in figure 5.5), to change the optical axis of the nanogratings. When the

5.2. PARAMETER DEPENDENCIES



(A) *OPD* as measured by the commercial polarimeter, which does not account for dichroism.

(B) *OPD* as obtained by the characterization setup when dichroism is neglected.

FIGURE 5.7. *OPD* as measured by the commercial polarimeter compared to the retrieved *OPD* from the characterization setup when dichroism is neglected. The nanogratings were written with 0° vs. 45° writing direction, for various polarization orientations of the inscription laser. Dashed lines are a guide to the eye

polarization of the laser beam is rotated, the retardation of the nanograting is also slightly changed. Therefore, to achieve the same retardation at different optical axes of the nanograting, the pulse energy has to be adjusted. The measurement results were confirmed using the commercial polarimeter.

5.2.4. Writing nanogratings with elliptically shaped beams. It has been shown in the previous section about waveguide inscription, that elliptically shaped beams can improve the transmission and reduce the birefringence of waveguides. To be able to use one and the same setup for waveguide writing and nanograting inscription, it has to be investigated how changing to an elliptically shaped beam changes the nanograting properties. The two different telescopes to be evaluated are the cylindrical telescope and the anamorphic zoom system presented in section 4.3. Inscriptions were made using both telescopes with a repetition rate of 100 kHz, a pulse duration of 300 fs and pulse energies ranging from $0.14 \mu\text{J}$ up to $1 \mu\text{J}$. This range of pulse energy corresponds to the available pulse energies of the laser system. When the anamorphic zoom system was used, no nanogratings were formed for pulse energies below $0.32 \mu\text{J}$. This is due to the decreased maximal focal intensity occurring for this beam shape, as has been shown in figure 4.6b. Typically, this decreased focal intensity would have to be compensated by using higher pulse energies for writing nanogratings with the anamorphic zoom system. However, higher pulse energies

were not available with the laser system. Therefore, more pulses per spot had to be used, to obtain the same order of magnitude in optical path difference as was achieved with the cylindrical telescope. This is the first significant drawback of using an anamorphic zoom system for beam shaping in nanograting inscription: the processing time increases significantly, if the available pulse energy is limited. The measured optical path differences of the nanogratings created with either telescope are given in figure 5.8.

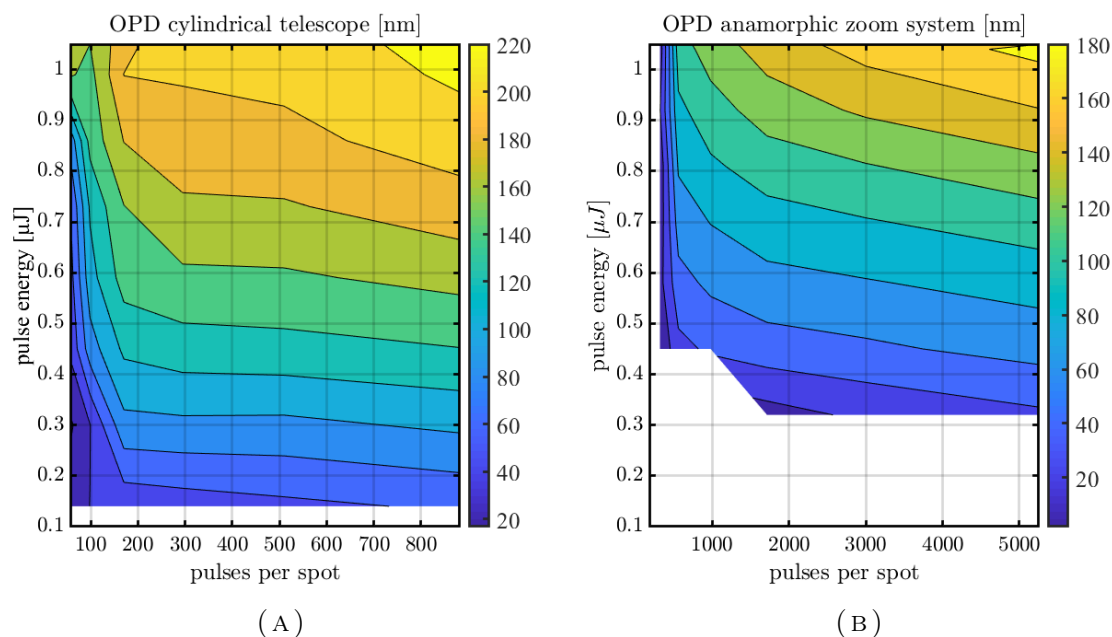


FIGURE 5.8. Optical path difference [nm] of nanogratings created when the inscription laser was shaped by either a) a cylindrical Galilean telescope or b) an anamorphic zoom system.

The general dependencies of the optical path difference on the laser inscription parameters are the same as in section 5.2.1: The optical path difference increases with increasing pulse energy and increasing pulses per spot. The maximum measured optical path difference was 220 nm for the structures inscribed with the cylindrical telescope and 180 nm for the structures inscribed with the anamorphic zoom system. To evaluate which telescope is better suitable for inscribing nanogratings, also the normalized losses divided by the optical path difference were measured. The results are given in figure 5.9.

The first thing which becomes apparent when comparing the results is that the range of losses per optical path difference are roughly 3x lower when the nanogratings were created with a cylindrical telescope compared to the nanogratings created with the anamorphic zoom system. The minimal normalized loss per optical path difference for the investigated parameter range was $2 \times 10^{-4} \text{ nm}^{-1}$ in the case of the

5.2. PARAMETER DEPENDENCIES

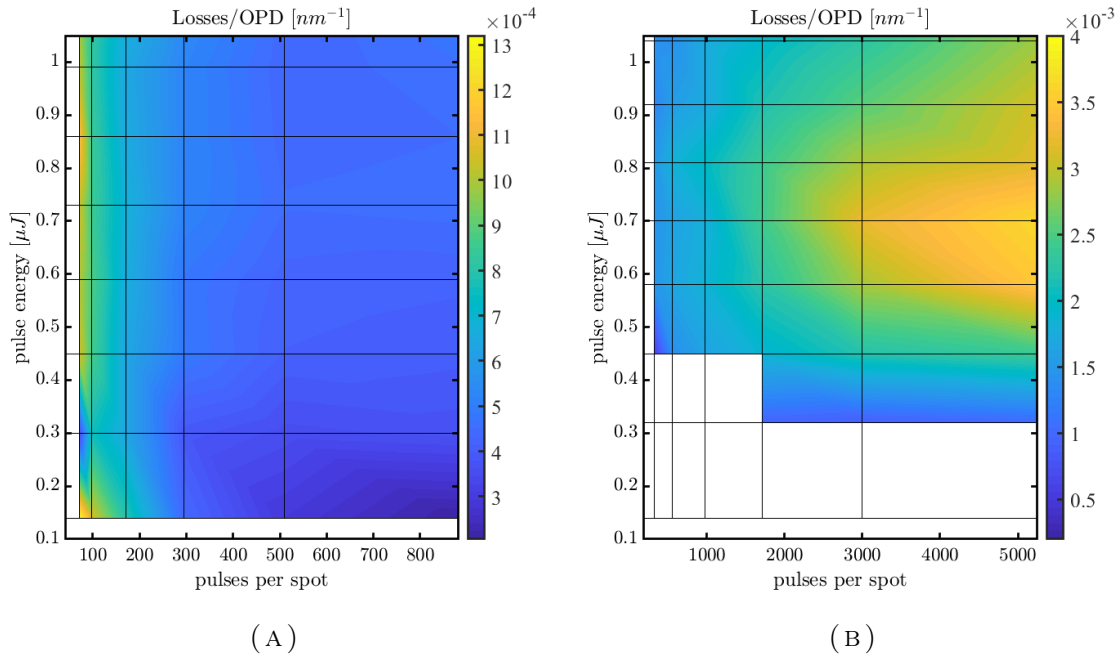


FIGURE 5.9. Normalized losses divided by optical path difference [nm^{-1}] of nanogratings created when the inscription laser was shaped by either a) a cylindrical Galilean telescope or b) an anamorphic zoom system.

cylindrical telescope and $6 \times 10^{-4} nm^{-1}$ in the case of the anamorphic zoom system. The maximum loss per optical path difference are $3.6 \times 10^{-3} nm^{-1}$ in the case of the anamorphic zoom system and $1.3 \times 10^{-3} nm^{-1}$ in the case of the cylindrical telescope. Additionally, the dependency of the losses per OPD on the inscription parameters varies strongly between the two telescopes. For the cylindrical telescope, the highest losses per OPD occurred for small number of pulses per spot, whilst for the anamorphic zoom system, this is where low losses occurred. The reason for this was not further studied in the scope of this thesis.

When comparing the results with the losses obtained with a spherical telescope in figure 5.2d, which showed values between $0.9 \times 10^{-3} nm^{-1}$ and $4.8 \times 10^{-3} nm^{-1}$, it can be seen that these losses are similar in magnitude to the ones obtained with the anamorphic zoom system. At the same time, the dependency of the losses per OPD on the laser parameters do not follow the same pattern as the nanogratings created with either the cylindrical telescope or the anamorphic zoom system.

So far, the influence of three different beamshaping techniques on nanograting properties have been tested: Firstly, a simple widening of the beam using the spherical Galilean telescope, with results shown in figure 5.2. Secondly, a cylindrical Galilean telescope was used, that only widened the beam in one direction, and thirdly, an anamorphic zoom system was tested, that not only widened the beam

in one direction, but narrowed it in the other. The properties of nanogratings created with the anamorphic zoom system, which has produced the best waveguides in chapter 4, were not convincing due to their high losses per *OPD* at low overall *OPD* and the long processing times it took to fabricate them. Both the spherical and the cylindrical Galilean telescope yielded nanogratings with higher optical path differences, that were produced in a shorter time. However, it became apparent that using a cylindrical telescope allows the creation of nanogratings with the lowest loss to *OPD* ratio. Therefore, at the tested laser system, it would be best to use two different beam lines with different telescopes for each of the inscription types: an anamorphic zoom system for waveguide writing and a cylindrical telescope for nanograting inscription. Without changing the optical system in between, the use of the cylindrical telescope is a compromise.

5.3. Single qubit quantum gates made of nanogratings

Now that both the properties of nanogratings and waveguides depending on the inscription parameters have been clarified, it is possible to combine both modification types, with the nanograting embedded in the waveguide. The purpose of the nanograting is to change the polarization state of light transmitted through the waveguide using its intrinsic form birefringence. The nanograting will therefore be treated as a waveplate inside the waveguide. The resulting structures can be used for both classical and quantum applications, which will be demonstrated using classical and quantum light sources.

5.3.1. Properties of the combination of waveguides with nanogratings.

Several nanograting-waveguide combinations were realized in fused silica samples of the size $0.15\text{ cm} \times 1\text{ cm} \times 4\text{ cm}$ using the writing setup introduced in section 3.1, given in figure 3.1, with a simple cylindrical telescope for beam shaping (the anamorphic zoom system was not designed yet at this point). The layout of a fused silica sample containing this combination is given in figure 5.10.

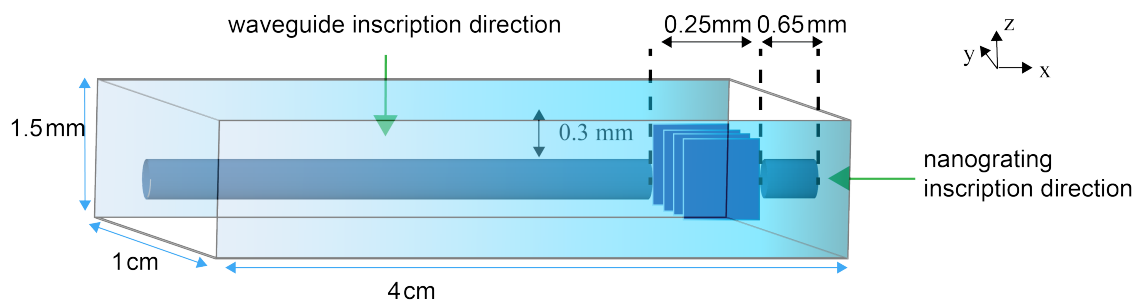


FIGURE 5.10. Layout of the nanograting and waveguide inscription inside a sample.

5.3. SINGLE QUBIT QUANTUM GATES MADE OF NANOGRATINGS

To inscribe nanogratings into the sample, laser light was focused through one of the end facets of the sample, so that the inscriptions were created in the y-z-plane. Then, the sample was rotated by 90° for inscribing the waveguides into the x-y-plane. This inscription configuration allows full use of the polarization control, because it enables a 360° rotation of the nanogratings optical axis in the plane perpendicular to the waveguide.

The orientation of the nanogratings was determined by the polarization of the writing laser beam during inscription, whereas the retardation of the nanogratings was varied mainly using the pulse energy and the amount of nanograting layers. All nanogratings were inscribed with 100 kHz repetition rate and 15 mm min^{-1} writing velocity. In this combination, the writing parameters of the waveguides were $0.12 \text{ } \mu\text{J}$ pulse energy, 600 mm min^{-1} writing velocity and 100 kHz repetition rate. When inscribed $240 \text{ } \mu\text{m}$ below the fused silica sample's surface, these waveguides typically showed losses of $(1.4 \pm 0.2) \text{ dB/cm}$ at $(0.031 \pm 0.007) \pi/\text{cm}$ birefringent phase retardation.

To demonstrate that by changing the optical path difference induced by the nanogratings one can control the polarization inside the waveguides, combinations of waveguides and nanogratings were characterized using the setup introduced in section 3.2, given in figure 3.2. The waveguides were all written with the same parameters, while for the nanogratings the inscription pulse energy was changed. The orientation of the nanogratings were kept the same for this investigation. The results are plotted in figure 5.11 and compared to measurements of only the nanogratings' optical path difference (as a measure of birefringence) using the commercial polarimeter described in the last paragraph of section 3.2.

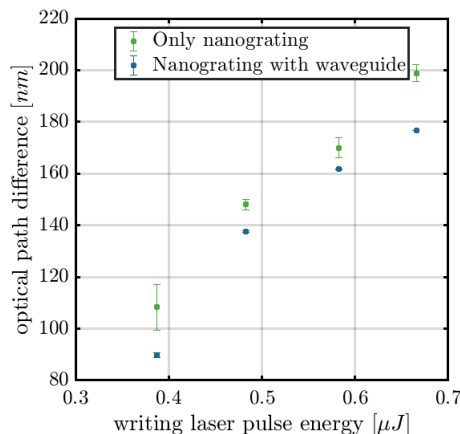


FIGURE 5.11. Measured optical path difference for nanogratings alone and nanograting-waveguide combinations. The parameters for the waveguides were kept the same for all measurement points, but the writing laser pulse energy was varied for the inscription of nanogratings.

As was to be expected from previous observations in section 5.2, the optical path difference induced by the nanogratings rises with the pulse energy used for inscribing the nanogratings. It can also be seen that when these nanogratings are combined with waveguides as given by the blue data in graph 5.11, the combined structure will follow the same trend, showing that the amount of birefringence in the combination is dominated by the nanograting birefringence and can thus be set by choosing an appropriate pulse energy for the nanograting inscription. An offset of 10 nm to 20 nm is visible between the optical path difference of only the nanograting and the optical path difference of the nanograting with a waveguide. Possible reasons for this offset could be the remaining waveguide birefringence, or differences between the two measurement methods, as discussed in sections 5.2.1 and 5.2.3.

Following this, it was demonstrated that by changing the optical axis of the nanogratings, also the optical axis of the nanograting-waveguide combination changes. This was demonstrated by creating several waveguide-nanograting combinations, where the polarization was rotated for each inscribed nanograting. The resulting optical axis and induced phase retardation was then evaluated using the characterization setup in figure 3.2 for nanograting-waveguide combinations. The results are plotted in figure 5.12.

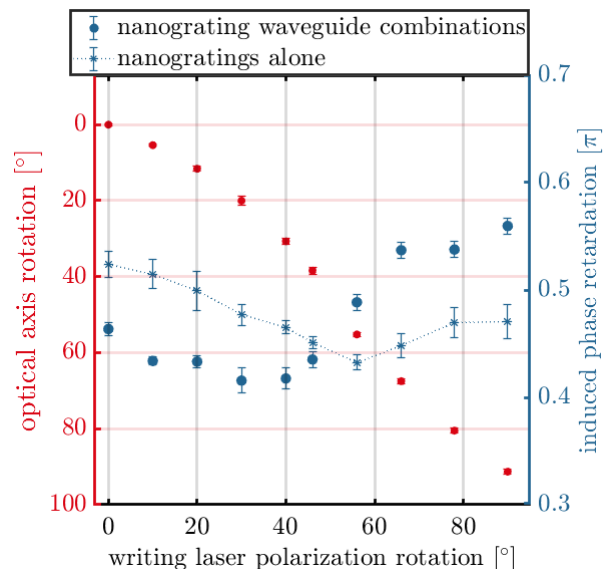


FIGURE 5.12. Effect of the rotation of the optical axis of nanogratings on the combination of nanograting and waveguide. The dotted line is a guide to the eye. The pulse energy for inscribing the nanogratings was $0.8 \mu\text{J}$.

The measured optical axis (plotted in red) spans a rotation of 90° . From previous experiments a linear relation between the writing laser polarization and the optical axis rotation of the system was to be expected (compare, for example, figure 5.6a).

Some small deviations from that linear trend are visible in figure 5.12, presumably caused by the remaining birefringence of the waveguide, which has an optical axis at 0° . Nevertheless, the whole range of optical axis orientations from 0° to 90° was accessible. Hereby it could be shown, that not only the strength of the birefringence of this system can be controlled (figure 5.11), but also the optical axis, which is a crucial degree of freedom for polarization control. Plotted in blue in figure 5.12 is the induced phase retardation by the nanogratings. As has been observed in section 5.2.3, this phase retardation changes when the orientation of the nanograting changes. Furthermore, depending on the optical axis orientation of the nanogratings, the overall induced phase delay of the waveguide-nanograting combination changes. At 0° polarization angle, it starts off as being smaller than the phase delay induced by nanogratings alone. At around 56° polarization angle, it becomes larger than the phase delay induced by nanogratings alone (figure 5.12). This also indicates the interplay of remaining waveguide birefringence with the nanograting birefringence.

5.3.2. Fabrication and characterization of quantum gates. The above presented approach of adding waveplates to an FLDW waveguide can generally be used in any integrated photonic chip where polarization control is desired. However, in recent years, pronounced efforts have been made to perform quantum optics experiments using FLDW circuits [143–145, 149–152]. Therefore, quantum optical applications have been chosen as an exemplary application demonstration.

In quantum optics, certain polarization transformations of single photons are known as specific quantum gates. In the following, it will be shown that specific quantum gates can be fabricated using a combination of nanogratings and waveguides. For this demonstration, the quantum gates Hadamard gate, Pi/8th gate, Pauli-x gate, and Pauli-z gate were fabricated (see section 2.4.2). The Pauli matrices are of special interest, because together with the 2×2 identity matrix they form a basis for the 2×2 vector space of hermitian matrices. Since the Pauli-y gate, however, can be created by combining a Pauli-x gate with a Pauli-z gate and a specific phase retardation [112], the focus here will lie on demonstrating the Pauli-x and the Pauli-z gate. The Hadamard gate and the Pi/8th gate were chosen because they can be part of a standard set for universal quantum computing [113].

5.3.2.1. *Classical characterization of quantum gate structures.* To create combinations of waveguides with nanogratings that are suitable for representing quantum gates, writing parameters suitable for creating specific birefringences were chosen. In table 5.1, the parameters used for writing these nanogratings are listed. Whenever the phase delay induced by a single layer was not sufficient, a second layer was added with a slight gap, as it is also indicated in table 5.1.

TABLE 5.1. Parameters for creating different gates.

Gate	Pulse energy [μJ]	Inscription polarization orientation	No. of Layers
Hadamard	0.8	112.5°	2
Pauli-x	0.7	135°	2
Pauli-z	0.8	90°	2
Pi/8th	0.4	90°	1

The birefringence of the structures listed in table 5.1 was characterized using the characterization setup in figure 3.2. A list of retrieved phase delays is given in table 5.2. It becomes clear that it was more difficult to obtain the desired phase delay if the nanogratings were inscribed with two layers. Here, deviations of up to 9% occurred. This might be due to the strain of the two layers also contributing to the birefringence.

TABLE 5.2. Measured properties of the created gates.

Gate	Retrieved phase delay [π]	Desired phase delay [π]
Hadamard	0.91	1
Pauli-x	0.93	1
Pauli-z	0.94	1
Pi/8th	0.24	0.25

For a full reconstruction of the Jones matrices of the quantum gates (which is the typical representation), a measurement using a $\lambda/4$ -plate is necessary. To retrieve these matrices, a generalized matrix $\overset{\leftrightarrow}{M}$ was assumed

$$\overset{\leftrightarrow}{M} = \begin{bmatrix} \tilde{A} & \tilde{B} \\ \tilde{C} & \tilde{D} \end{bmatrix}, \quad (5.4)$$

with $\tilde{A}, \tilde{B}, \tilde{C}, \tilde{D}$ being complex. These complex numbers consist of amplitude and phase, for example,

$$\tilde{A} = aA \cdot e^{i \cdot pA}. \quad (5.5)$$

The same structure applies for $\tilde{B}, \tilde{C}, \tilde{D}$, with the variable names adjusted correspondingly. The absolute values aA, aB, aC and aD can be measured by going into the sample with horizontally and vertically polarized light and measuring the output power for a horizontally or vertically positioned polarizer after the sample. Normalizing these power measurements to the overall output power and taking the

5.3. SINGLE QUBIT QUANTUM GATES MADE OF NANOGRATINGS

roots yields the desired values. The phase pA can be set to zero as a reference phase, because any overall phase can be omitted. To find the remaining phases pB , pC , and pD , the crossed polarizer setup in figure 3.2 was used again. Additionally, a quarter-waveplate was put after the first half-waveplate to diminish the sign ambiguity of the phases.

A formula based on Jones calculus was used to represent the normalized power P transmitted through a sample described by $\overset{\leftrightarrow}{M}$ in a crossed polarizer setup. A rotation by an angle α is described by the rotational matrix

$$\overset{\leftrightarrow}{R}(\alpha) = \begin{bmatrix} \cos(\alpha) & -\sin(\alpha) \\ \sin(\alpha) & \cos(\alpha) \end{bmatrix}. \quad (5.6)$$

The definitions of the matrices $\overset{\leftrightarrow}{P}(\phi)$ of a polarizer rotated by ϕ and $\overset{\leftrightarrow}{W}(\eta, \phi)$ of a waveplate with birefringence η and an angle ϕ (between the waveplate's fast axis and the reference system's x-axis) are

$$\overset{\leftrightarrow}{P}(\phi) = \overset{\leftrightarrow}{R}(\phi) \begin{bmatrix} 1 & 0 \\ 0 & 0 \end{bmatrix} \overset{\leftrightarrow}{R}(-\phi); \quad \overset{\leftrightarrow}{W}(\eta, \phi) = \overset{\leftrightarrow}{R}(\phi) \begin{bmatrix} e^{-i\eta/2} & 0 \\ 0 & i\eta/2 \end{bmatrix} \overset{\leftrightarrow}{R}(-\phi). \quad (5.7)$$

Using these matrices, the transmitted power P through the crossed polarizer setup in dependence of the matrix entries of $\overset{\leftrightarrow}{M}$ and a rotation of α can be calculated as

$$P = \left\| \overset{\leftrightarrow}{P}(\alpha + \pi/2) \cdot \overset{\leftrightarrow}{M} \cdot \overset{\leftrightarrow}{W}(\pi/2, -\pi/4) \cdot \overset{\leftrightarrow}{W}(\pi, \alpha/2) \cdot \begin{bmatrix} 1 \\ 0 \end{bmatrix} \right\|^2. \quad (5.8)$$

By fitting the data to equation (5.8) under the limit of the known values for aA , aB , aC , aD , all matrix phase entries were determined. The starting points for the fit algorithm were set to $pB = pC = 0$, while pD was chosen according to the birefringence results of the crossed polarizer setup. The results are shown in table 5.3. Here, the tolerances of the matrices' absolute values are based on measurement fluctuations. The phase tolerances are retrieved by changing the matrices' absolute values in the fit algorithm and observing, how much the fit result changes.

To fully characterize these structures as quantum gates it is more suitable to use quanta, i.e., single photons, instead of classical light. This will be presented in the following section.

TABLE 5.3. Classically reconstructed matrices of quantum gates.

Gate	Matrix
Hadamard	$\begin{bmatrix} (0.776 \pm 0.002) & (0.550 \pm 0.003) \cdot e^{i \cdot (0.070 \pm 0.002)\pi} \\ (0.631 \pm 0.003) \cdot e^{-i \cdot (0.011 \pm 0.001)\pi} & (0.835 \pm 0.002) \cdot e^{i \cdot (0.938 \pm 0.002)\pi} \end{bmatrix}$
Pauli-x	$\begin{bmatrix} (0.210 \pm 0.004) & (0.981 \pm 0.001) \cdot e^{i \cdot 0.013\pi} \\ (0.978 \pm 0.001) \cdot e^{i \cdot (0.031 \pm 0.001)\pi} & (0.195 \pm 0.006) \cdot e^{-i \cdot (0.023 \pm 0.002)\pi} \end{bmatrix}$
Pauli-z	$\begin{bmatrix} (0.991 \pm 0.001) & (0.131 \pm 0.008) \cdot e^{i \cdot (0.11 \pm 0.02)\pi} \\ (0.132 \pm 0.008) \cdot e^{i \cdot (0.01 \pm 0.01)\pi} & (0.991 \pm 0.001) \cdot e^{i \cdot (1.36 \pm 0.01)\pi} \end{bmatrix}$
Pi/8th	$\begin{bmatrix} (0.998 \pm 0.001) & (0.086 \pm 0.019) \cdot e^{-i \cdot (0.03 \pm 0.06)\pi} \\ (0.055 \pm 0.019) \cdot e^{-i \cdot (0.71 \pm 0.11)\pi} & (0.996 \pm 0.001) \cdot e^{i \cdot (0.25 \pm 0.02)\pi} \end{bmatrix}$

5.3.2.2. *Single photon characterization of quantum gates.* In this section the results of single photon characterization of the fabricated four quantum gates will be demonstrated. The goal was to reconstruct the matrices of the quantum gates with single photons instead of classical light. The experiments were performed and evaluated at the physics institute of the university of Rostock together with Max Ehrhardt. The experimental setup is shown in figure 5.13.

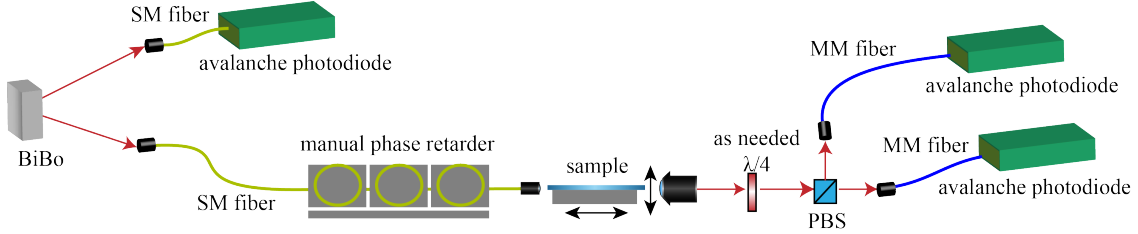


FIGURE 5.13. Single photon measurement setup.

Single photon pairs were produced by spontaneous parametric down conversion in a bismuth borate crystal, pumped by a laser diode of $\lambda = 407.5$ nm wavelength. The resulting single photons were then coupled into single mode fibers. The wavelength of the single photons was 815 nm, close to the wavelength of the classical characterization before. One of the two entangled photons was butt-coupled into the sample, whilst the other was directly detected. The directly detected photon served as a heralding photon, signaling the presence of a photon pair. Fiber polarization controllers were used to change the input polarization of the photon entering the sample. The input polarizations used were $|H\rangle$, $|V\rangle$, $|L\rangle$ and $|R\rangle$. At the output, a beam splitter and when needed a quarter-waveplate ($\lambda/4$) oriented at $\pm 45^\circ$ were used to measure the output in the ($|H\rangle/|V\rangle$) basis or ($|L\rangle/|R\rangle$) basis (see equations

5.3. SINGLE QUBIT QUANTUM GATES MADE OF NANOGRATINGS

2.33 and 2.34). The absolute values of the matrices were directly determined by the measurements of horizontally polarized and vertically polarized photons in the ($|H\rangle/|V\rangle$) basis. Afterwards, measurements of horizontally, vertically, left circularly, and right circularly polarized input photons in both the ($|H\rangle/|V\rangle$) and ($|L\rangle/|R\rangle$) were made.

The results of these measurements were used in a residual sum of square minimization to determine the phases of these matrices. To omit an overall phase, the phase of the first matrix entry was set to zero in all cases. Using Poissonian statistics and the statistics of multiple measurements, error bars were retrieved. A list of all the matrices can be found in table 5.4, with corresponding bar charts in figure 5.14. When comparing the results obtained using classical light measured in section 5.3.2 with the results obtained with single photons, most matrix values (amplitudes and phases) correspond to each other within the measurement tolerances, or only show small differences up to 5%. Nevertheless, some matrix entries show stronger deviations, for example, the amplitude aD of the Pauli-X matrix, was found to be (0.195 ± 0.006) in the classical case and (0.262 ± 0.007) for the quantum measurement, amounting to a difference of 0.067 ± 0.013 . Another notable difference can be seen for the phases pD of the Pauli-z gate, which deviate by up to 0.5π . These differences might be explainable by the fitting algorithm converging in local minima, combined with differences caused by the different setup used and the difference in characterization wavelength. The fidelities of the matrices retrieved using single photons were also calculated and can be found in table 5.5.

TABLE 5.4. Retrieved matrices using single photon measurements.

Gate	Matrix
Hadamard	$\begin{bmatrix} (0.738 \pm 0.002) & (0.579 \pm 0.003) \cdot e^{-i \cdot (0.01 \pm 0.04)\pi} \\ (0.674 \pm 0.003) \cdot e^{-i \cdot (0.09 \pm 0.06)\pi} & (0.816 \pm 0.002) \cdot e^{-i \cdot (0.92 \pm 0.05)\pi} \end{bmatrix}$
Pauli-x	$\begin{bmatrix} (0.201 \pm 0.005) & (0.965 \pm 0.002) \cdot e^{i \cdot (0.06 \pm 0.06)\pi} \\ (0.980 \pm 0.001) \cdot e^{i \cdot (0.01 \pm 0.12)\pi} & (0.262 \pm 0.007) \cdot e^{-i \cdot (0.04 \pm 0.05)\pi} \end{bmatrix}$
Pauli-z	$\begin{bmatrix} (0.993 \pm 0.001) & (0.168 \pm 0.003) \cdot e^{-i \cdot (0.09 \pm 0.03)\pi} \\ (0.119 \pm 0.003) \cdot e^{-i \cdot (0.05 \pm 0.08)\pi} & (0.986 \pm 0.001) \cdot e^{i \cdot (0.85 \pm 0.03)\pi} \end{bmatrix}$
Pi/8th	$\begin{bmatrix} (0.981 \pm 0.001) & (0.243 \pm 0.005) \cdot e^{-i \cdot (0.4 \pm 0.05)\pi} \\ (0.194 \pm 0.006) \cdot e^{i \cdot (0.2 \pm 0.1)\pi} & (0.970 \pm 0.001) \cdot e^{i \cdot (0.23 \pm 0.04)\pi} \end{bmatrix}$

With this experiment it was demonstrated that nanograting-waveguide combinations can be used to fabricate quantum gates. The achieved fidelities, listed in table 5.5,

TABLE 5.5. Calculated fidelities.

Gate	Fidelity $F^{(H\rangle, V\rangle)}$
Hadamard	0.966 ± 0.008
Pauli-x	0.930 ± 0.031
Pauli-z	0.979 ± 0.007
Pi/8th	0.952 ± 0.011

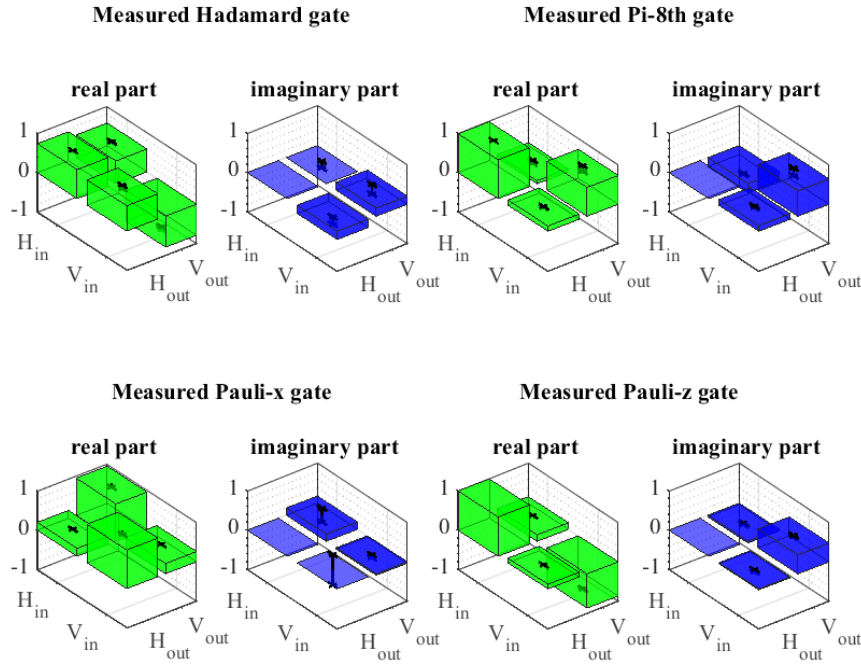


FIGURE 5.14. Visualization of the retrieved matrices using single photon measurements.

are all close to the desired fidelity of 1. Since none of the gates fully matched the desired phase delay (compare table 5.2), a deviation from a fidelity of 1 was expected. The losses of these structures were measured to lie between 13.2 dB and 14.8 dB, with the main loss contribution coming from the waveguide structures themselves (7.3 dB to 8.1 dB), 4.9 dB coming from a mode mismatch between the single mode fiber that is butt-coupled into the waveguide and the waveguide mode, and 0.3 dB coming from Fresnel reflection losses.

Former approaches of integrated polarization-encoded quantum gates (see section 2.6) relied on using stress fields of defects next to waveguides [152] or the birefringence of waveguides themselves [151]. Compared to the previous approach of using tilted waveguides as waveplates for quantum applications, nanogratings have two main advantages. On the one hand, tilts of more than 45° of the optical axis

of waveguides were not possible in [151], which limits the possible orientations of the retarders, whilst 360° rotations of nanogratings can be easily achieved just by altering the polarization of the inscription beam. Additionally, the approach of tilting waveguides to change their optical axis only works with high NA immersion objectives. In general, the objective's working distance decreases as the numerical aperture increases. Furthermore, immersion objectives are especially restricted in their working distance due to the requirement that the immersion liquid has to be in contact with both the objective and the sample. Since the focussing depth in the material is limited by the inscription objective's working distance, this also limits one of the key advantages of the direct writing technique, namely the three dimensional fabrication of structures. The nanogratings on the other hand were fabricated with a 20x inscription objective with a smaller numerical aperture ($NA = 0.4$) and a working distance of 1.2 mm. In principle, the nanograting approach could also be fabricated with a long working distance objective, extending the three dimensional fabrication ability even further, if required. On the other hand, another striking advantage of the quantum gates made of nanogratings is their compactness. Even when two layers of nanogratings were used to achieve the desired retardation, the thickness of the structures in propagation direction was less than $250\ \mu\text{m}$. In contrast, for the previously reported approaches based on waveguides or stress fields, the utilized birefringences ranged on the order of $\Delta n = 1 \times 10^{-5}$, which is orders of magnitude lower than the typical nanograting birefringence of $\Delta n = 1 \times 10^{-3}$. Therefore, the required length of the retarders for the existing approaches ranged on the order of centimeters. Hence, it can be concluded that the approach presented here for the generation of quantum gates using nanogratings contributes significantly to the reduction of the device size for quantum photonics.

5.4. Novel beam shapes for nanograting inscription

All the previously reported studies on inscribing nanogratings were solely based on circular or ellipsoid-shaped Gaussian beams. Lately, more elongated beam shapes like the Bessel-like beam have become popular in laser based glass machining [187], for example, for welding [188] and cutting [189, 190]. In this section it will be studied whether these kinds of beams can also be used to improve the properties of nanogratings. For this purpose, conical phase front beam shaping will be used. Therefore, a conical phase front is imposed onto a Gaussian beam by a spatial light modulator (SLM) before the beam is focused (using, for example, a lens) into the material to be modified (see figure 5.15). In the focal plane of the lens, the beam will have a doughnut-shaped intensity distribution, either followed by or preceded by a Bessel-like intensity profile, depending on the angle of the conical phase front. Recently, it was shown that, using these beam shapes, the length of filaments formed

by laser inscription can be varied [191]. Adjusting the conical phase front of an inscription beam can also be used to improve the guiding properties of waveguides written deep inside glass, which would otherwise suffer due to deformation of the intensity distribution caused by nonlinear propagation effects and aberrations [192]. In this section the possibility to inscribe nanogratings with this beam shape will be demonstrated, and the dependency of the nanograting properties on the inscription parameters will be discussed.

5.4.1. Inscription and characterization. The inscription of the nanogratings was made in Toronto by Ehsan Alimohammadian in the research group of Prof. Herman. The laser used for inscription is an Amplitude Satsuma system delivering pulses of 250 fs pulse duration and 515 nm wavelength at a repetition rate of 500 kHz. The pulse energy was varied from 78 nJ to 434 nJ. Conical phase front angles ranging from -0.69 mrad to 0.69 mrad were imposed on the beam using a Hamamatsu SLM (X10468-04). The SLM was imaged with a magnification of 2.4 onto the inscription asphere (Newport, $NA = 0.55$). This inscription asphere was underfilled, so that the effectively used NA was 0.2. A sketch of the setup is given in figure 5.15. The

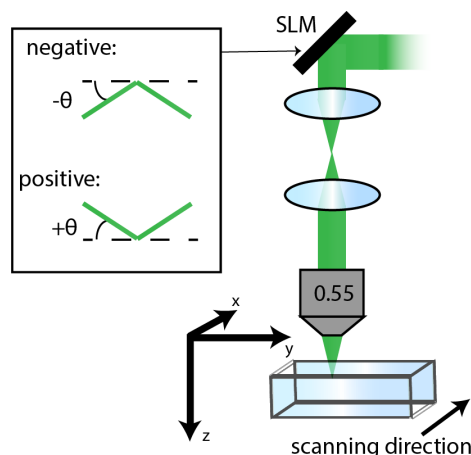


FIGURE 5.15. Setup sketch for inscription of nanogratings with Gaussian beams that have a negative or positive conical phase front θ (SLM = spatial light modulator). The sample material is fused silica.

focus of the lens was positioned $100 \mu\text{m}$ below the surface of the Nikon NIFS-S fused silica sample. The scanning speed was set to 0.4 mm min^{-1} . For a constant set of parameters, $60 \mu\text{m}$ long lines were inscribed 60 times next to each other with a $1 \mu\text{m}$ line separation to create modification squares. The created structures were characterized at a wavelength of 633 nm using the setup described in section 3.2 and given in figure 3.2. Furthermore, inspection by transmission microscopy and scanning electron microscopy (SEM) was made. To enable the SEM images, the sample was polished down to the modifications, then etched using 1% hydrofluoric acid for 90 s. Finally, the sample was carbon coated to reduce charge accumulation.

5.4. NOVEL BEAM SHAPES

5.4.2. Morphology inspection of the created structures. The cross section of the inscribed structures was inspected using transmission microscopy images to reveal the thickness of the modifications. An exemplary image for structures written with 332 nJ is given in figure 5.16.

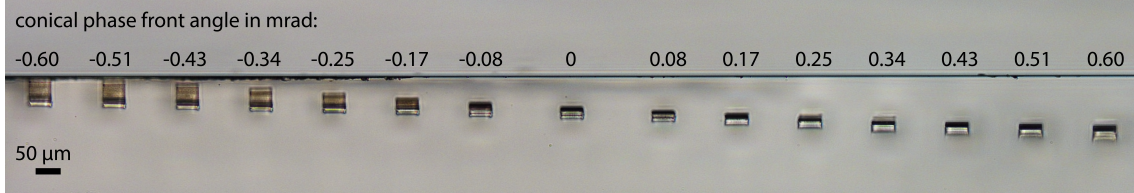


FIGURE 5.16. Microscope image of the x-z-plane of the modifications, left to right: negative to positive conical phase front angles. These modifications were inscribed with a pulse energy of 332 nJ.

In the microscope image it is visible that the modification position moves closer to the surface for negative conical phase front angles, and further away from the surface for positive conical phase front angles. Additionally, an asymmetry in the modification length in laser propagation direction (“thickness”) is found between structures that were created with negative or positive conical phase front angles. While the thicknesses of the modifications created with positive conical phase fronts only slightly changes, the modifications created with negative conical phase fronts become significantly thicker with decreasing angle. For the lowest conical phase front angles the thickness of the modifications reach the samples surface, which limits their further expansion.

In addition to the transmission microscopic images, scanning electron microscopic images were also taken, selected examples of which are shown in figure 5.17. On the one hand, the presence of nanogratings is confirmed by these images, as well as their orientation perpendicular to the laser inscription polarization, and on the other hand, these images also confirm the change in modification length as was already observed in the transmission microscopy images.

Numerical simulations for single pulse propagation made by Dr. Alessandro Alberucci, based on a code developed by Dr. Jisha Chandroth-Pannian (both from the Institute of Applied Physics Jena), can help understand this phenomenon. According to these simulations [193], filaments form above or below the doughnut shaped focal plane for negative or positive conical phase fronts. Highest intensities are reached inside of these filaments, whilst the intensity in the focal plane remains below the modification threshold. Simulated axial fluences along the propagation direction z for different conical phase front angles at different pulse energies are plotted in figure 5.18. For the lowest simulated pulse energy of 5 fJ, no non-linear propagation effects

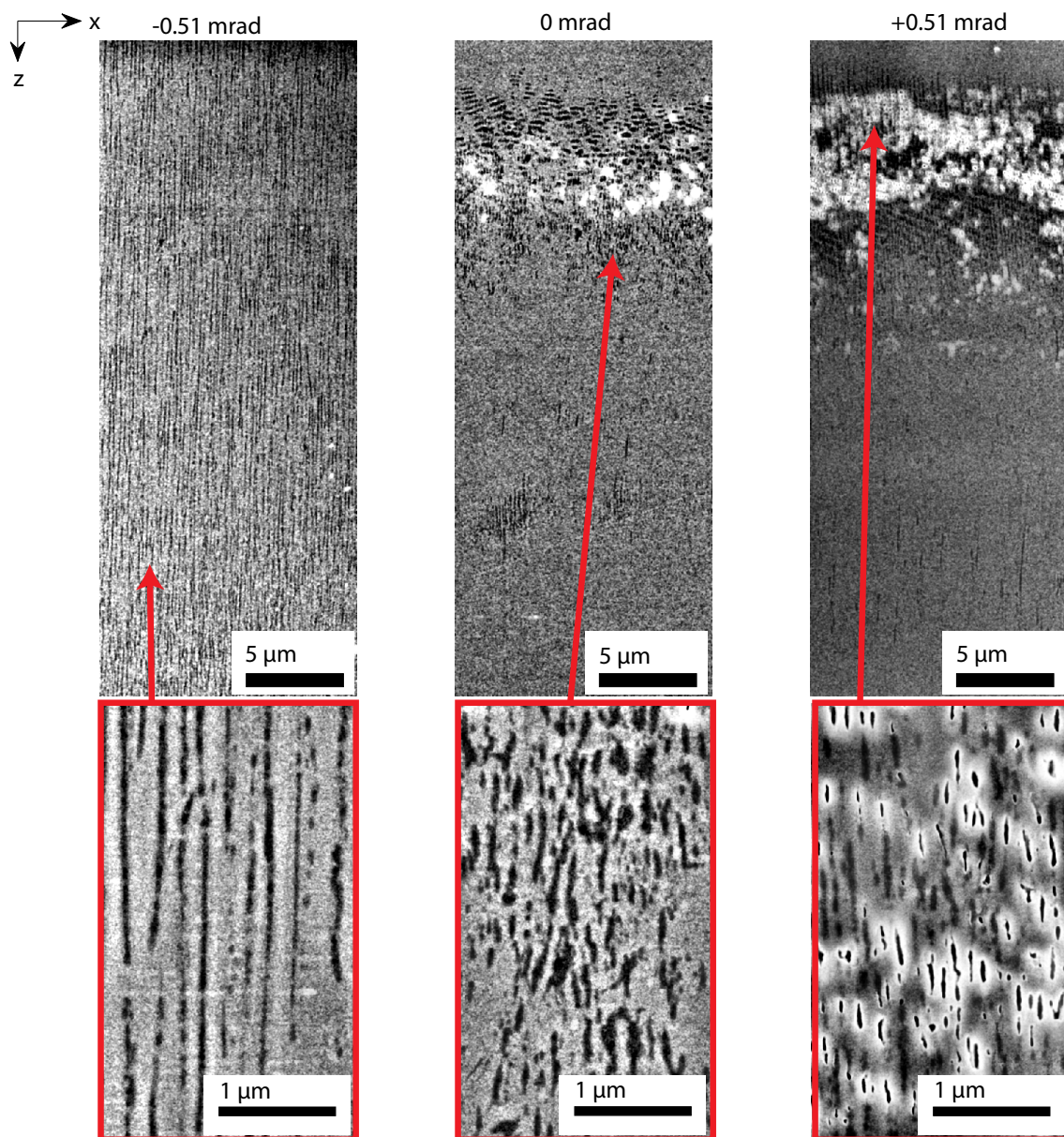


FIGURE 5.17. Exemplary SEM images of modifications written with positive and negative conical phase front angles. The inscription pulse energy is 332 nJ.

occur, resulting in symmetric axial fluences for both positive and negative conical phase front angles. With increasing pulse energy, however, nonlinear propagation effects distort the axial fluence, breaking the symmetry between positive and negative conical phase front angles.

For negative conical phase front angles, intensity clamping and other nonlinear propagation effects occur in the filament forming above the focal plane, which inhibit significant pulse energies to reach the focal volume and also cause the filament length to grow for high pulse energies. When the maximum intensity limited by intensity

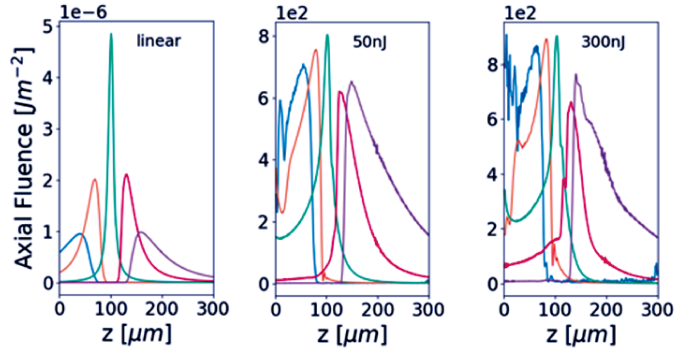


FIGURE 5.18. Simulated axial fluence of single pulse propagation with conical phase front beam shaping at different pulse energies (from left to right: 5 fJ (“linear”), 50 nJ and 300 nJ). The colors refer to the different conical phase front angles of $\theta = -0.7$ mrad in blue; $\theta = -0.35$ mrad in yellow, $\theta = 0$ mrad in green, $\theta = 0.35$ mrad in red and $\theta = 0.7$ mrad in purple.

clamping is reached, the excess energy spreads in the laser-irradiated volume above. The high intensities in the filament turn into modifications above the focal plane. For positive conical phase front angles, the filament is formed below the focus. Nonlinear effects in the focal plane and in the front part of the filament clamp the available maximum intensity below the focal plane. High intensities mainly occur in the front part of the filament, limiting the expansion of the filament and leading to thinner modification zones. Above the focal plane, due to the beam geometry, the excess energy is spread widely. The intensities reached above the focal plane are therefore too low to induce modifications.

5.4.3. Optical properties of nanogratings created with conical phase fronts. To understand how the different nanograting structures influence the optical properties, they were evaluated using the characterization setup given in figure 3.2 and explained in section 3.2. In addition, the thicknesses of the modifications was measured using calibrated camera images. The measured physical properties (thickness, optical path difference, losses, and dichroism) are given in figure 5.19.

In the figure, the thresholds for nanograting formation can be seen by the white space in the diagrams. For writing pulse energies of 168 nJ, no nanogratings developed at 0.69 mrad conical phase front angle. Likewise for 78 nJ pulse energy, nanogratings only developed for conical phase front angles of -0.26 mrad to 0.26 mrad.

The **thickness** plotted in figure 5.19a confirms the asymmetry between positive and negative angles, that had already become apparent in section 5.4.2. For positive conical phase front angles, no clear dependence of the modification thickness on the phase front angle is observed. For negative conical phase front angles, however, a

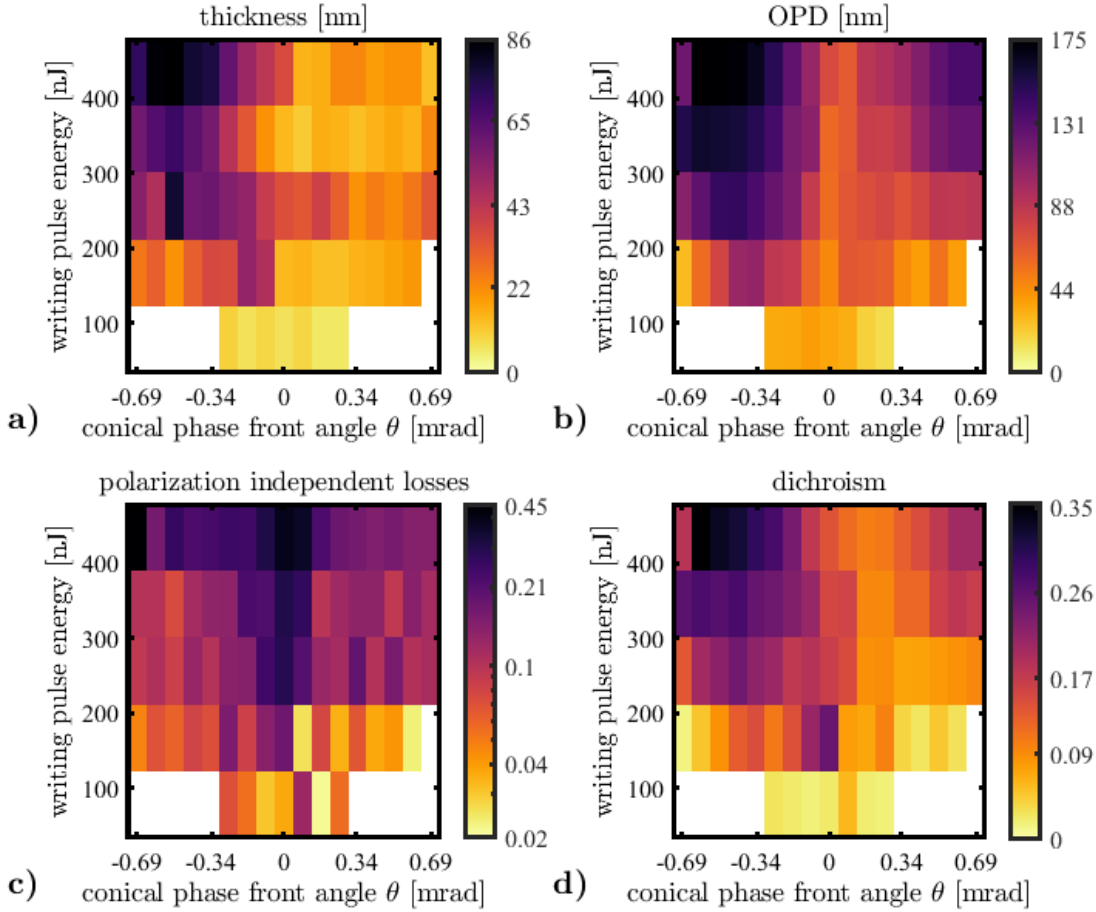


FIGURE 5.19. Measured physical properties of nanogratings created with different conical phase front angles. The subfigures show a) the thickness of the modifications [μm], b) the optical path difference [nm] induced by the modifications, c) the polarization independent losses normalized to 1, and d) the dichroism of the modifications normalized to 1. The colormap is inferno [194].

thickening of the structure is observed. The thickest modification, reaching $86 \mu\text{m}$, was created at a phase front angle of -0.51 mrad with a pulse energy 434 nJ .

Figure 5.19b shows the *OPD* of the modifications in nanometers. For all conical phase front angles, the *OPD* rises with increasing inscription pulse energy, similar to what had been observed for all other nanogratings in this thesis (i.e., figures 5.2a and 5.8). When moving from a conical phase front angle of zero (corresponding to the Gaussian beam) towards either positive or negative conical phase front angles, an increase in optical path difference is seen, albeit stronger for negative conical phase front angles than for positive. For negative phase front angles, a “sweet spot” around -0.51 mrad is observed. When further decreasing the phase front angle beyond the sweet spot, the optical path difference decreases again. The maximum measured

5.4. NOVEL BEAM SHAPES

OPD was 175 nm for modifications written with a phase front angle of -0.51 mrad and a pulse energy of 434 nJ.

The measured **polarization independent losses** of the modifications are given in figure 5.19c, plotted with a logarithmic colorbar and ranging from 2% to 45%. For conical phase front angles of -0.17 mrad to 0.17 mrad, the losses clearly increase with rising pulse energy. For other conical phase front angles, the losses also increase with rising pulse energy, but not as strongly. For most pulse energies, nanogratings written with conical phase front angles larger than 0.26 mrad, or smaller than -0.26 mrad show less losses than nanogratings written without conical phase front angles (i.e., at a conical phase front angle of 0). This changes at a pulse energy of 434 nJ, where the losses of negative conical phase front angles reach about half the losses at zero conical phase front angle.

The polarization dependent losses, in other words the **dichroism** values, are plotted in figure 5.19d. For negative conical phase front angles, the dichroism values follow a similar pattern to the thicknesses in figure 5.19a, with the maximum value of 35% occurring at the highest inscription pulse energy of 434 nJ and a conical phase front angle of -0.60 mrad. For positive conical phase front angles, the dichroism behaviour does not resemble the thickness behaviour. Instead, a clear rise in birefringence for large phase front angles starting at 332 nJ pulse energy can be seen. The maximum measured dichroism value for positive conical phase front angles was 20%, which was observed for a phase front angle of 0.69 mrad at 434 nJ pulse energy.

To evaluate, which of these properties are solely changing due to a change in the modified volume, the measured values in 5.19b–c were normalized to their thickness values as given in 5.19a. The results of this normalization are shown in figure 5.20a–c. From the data normalized in this way, it is possible to see for which parameters the strongest losses (either polarization-dependent or polarization-independent) and/or the strongest optical delay per volume occur.

Normalizing the *OPD* from figure 5.19b to the modification thickness in figure 5.19a yields the average **birefringence** Δn of the structure along the characterization lasers propagation direction. The results are plotted in figure 5.20a. For negative conical phase front angles of -0.17 mrad or lower, with pulse energies ranging from 168 nJ to 434 nJ, the birefringence is roughly constant, ranging from $\Delta n = 1.1 \times 10^{-3}$ to $\Delta n = 3.7 \times 10^{-3}$. This indicates, that the increased *OPD* for these values relies solely on the thickness of the modification, leading to an accumulated retardation along the propagation direction. For positive conical phase front angles, an enhancement of the birefringence can be observed, especially when inscription pulse energies higher than or equal to 332 nJ are used. Birefringence values up to

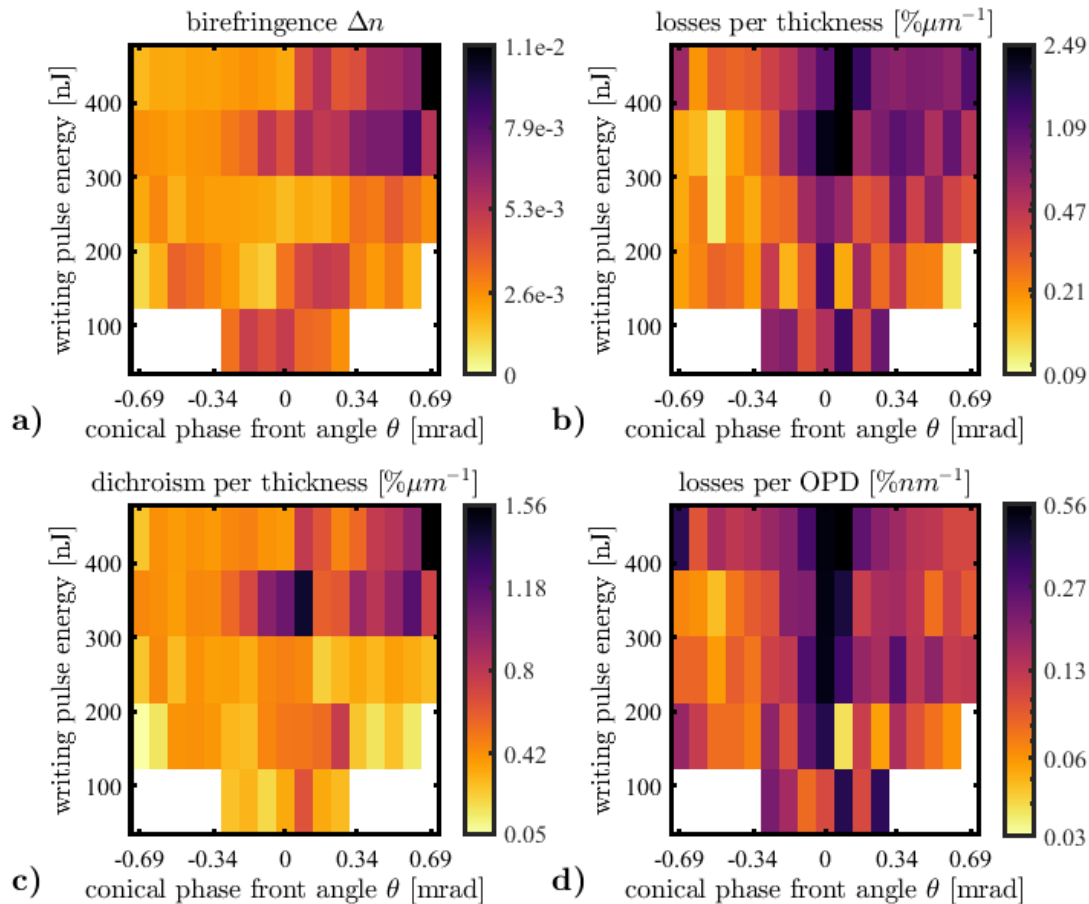


FIGURE 5.20. Normalized properties of the inscribed nanogratings. a) birefringence Δn , b) losses normalized to nanograting thickness [$\% \mu\text{m}^{-1}$], c) dichroism normalized to the nanograting thickness [$\% \mu\text{m}^{-1}$], d) losses normalized to the optical path difference [$\% \text{nm}^{-1}$].

$\Delta n = 1.1 \times 10^{-2}$ were measured for positive conical phase front angles, which is an increase by a factor of 3 compared to the maximum birefringence obtained with conical phase front angles of -0.69 mrad to -0.17 mrad.

When looking at the **losses normalized to the modification thicknesses**, which are plotted with a logarithmic colormap in figure 5.20b, it is possible to deduce for which laser writing parameters the morphology of the nanogratings itself becomes more lossy, and for which parameters an increase of loss is only related to the increased thickness of the structure. The maximum value of $6.6 \% \mu\text{m}^{-1}$ can be found for high pulse energies at zero conical phase front angles, indicating this is the case where the lossiest structures are formed. At the same time, when comparing negative to positive conical phase front angles, the normalized losses of the positive conical phase front angles tend to be higher than the normalized losses of the negative conical phase front angles written with the same writing pulse energy. Lowest values

5.4. NOVEL BEAM SHAPES

of $0.1\% \mu\text{m}^{-1}$ are found for conical phase front angles of -0.51 mrad at pulse energies of 256 nJ to 332 nJ.

In figure 5.20c, depicting the **dichroism normalized to thickness**, most parameters lead to the same value, indicating that any rise in dichroism given in figure 5.19d is only related to the thicker volume of the modification, with an average normalized dichroism for all measured values created with pulse energies up to 242 nJ being $0.3\% \mu\text{m}^{-1}$. An increase of dichroism up to $1.6\% \mu\text{m}^{-1}$ is seen for modifications created with positive conical phase front angles at pulse energies of 332 nJ and higher, coinciding with the increase of birefringence seen in figure 5.20a. This shows that the modifications written with negative conical phase front angles are not only more birefringent than the modifications written with negative conical phase front angles for a fixed writing pulse energy, but they are also more dichroic and more lossy.

Finally, to evaluate the lossiness of the structures for applications as phase retarders, the **losses normalized to the optical path difference** are given in figure 5.20d. This normalization can be used to evaluate how much losses can be expected if a certain amount of optical path difference shall be obtained. The values in figure 5.20d range up to $0.55\% \text{nm}^{-1}$. The average value lies at $0.15\% \text{nm}^{-1}$. The highest values can be found for modifications written with a conical phase front angle of 0 at pulse energies of at least 242 nJ. From this it can be seen that adding any conical phase front angle smaller or greater than zero can help reducing losses, but also, that modifications created with negative conical phase front angles show a more beneficial *OPD* to loss ratio than those created with positive conical phase front angles.

To conclude, this study has shown that negative conical phase front angles allow the creation of nanogratings exhibiting higher *OPD* per irradiation scan, caused by an increased thickness of the modification. The downside of using negative conical phase front angles is the increased dichroism of the nanograting. Higher birefringences on the other hand are achieved with positive conical phase fronts. By choosing to use either positive or negative conical phase front angles for inscription, it is thus possible to tune the thickness of the modification and its exhibited retardation individually. For example, one might write multiple layers of modification with a positive conical phase front angle at a pulse energy of 434 nJ, leading to a final thickness t , and a second modification with the same pulse energy by one irradiation scan with a negative conical phase front angle, leading to the same modification thickness t at different retardances. Based on the results reported in this section, it can be expected, that the accumulated values for retardation, dichroism, and losses of the multi-layer structure created with positive conical phase fronts is higher than the same values of the structure created with negative conical phase fronts. The observed

shift of the modifications (as seen in figure 5.16) when changing the conical phase front might be beneficial for altering the modification depth in a sample without mechanically translating it.

When comparing the properties of the nanogratings created with conical phase front angles to the properties of the nanogratings created with a Gaussian beam, and keeping other inscription parameters the same (pulse energy, scanning speed, and repetition rate), it was found that nanogratings that were created with suitable conical phase front angles exhibited less losses at higher optical path difference per irradiation scan. This is especially important when using nanogratings as retardation elements in applications that are sensitive to loss, for example, quantum applications. For further improvements, also alternative birefringent structures should be taken into account. One option could be the recently reported birefringent FLDW modification named “Type X”, which exhibits significantly lower losses than nanogratings, but at the same time also significantly lower optical retardation [195].

CHAPTER 6

Adaptive Polarization Control Using Liquid Crystals

In the previous chapter, the concept of nanogratings as embedded waveplates in FLDW waveguides was demonstrated. One downside of this methodology is, that once a nanograting has been inscribed, it is fixed and can only be changed by re-inscribing. For practical purposes, it would be great to be able to dynamically change the state of an embedded waveplate. In this chapter, this is achieved by embedding liquid crystals into waveguides. First, the details of the sample fabrication will be described, followed by a demonstration of electro-optical modulation of the output polarization of an FLDW waveguide.

6.1. Sample preparation and waveguide inscription

The sample of choice for these experiments is a commercially available liquid crystal cell with an $(8.0 \pm 0.8) \mu\text{m}$ gap (Thorlabs LCC1318-A). The cell is an ECB cell, consisting of two 3 mm thick glass slides made from UV grade fused silica. Each glass slide is coated with indium tin oxide, which serves as the electrode, and rubbed polyimide, which serves as the alignment layer. The pre-tilt angle of the cell is $(4.5 \pm 0.5)^\circ$. Waveguides were to be inscribed transversely into the cell, so that they cross the liquid crystal layer perpendicularly. A sketch of the inscription layout is given in figure 6.1. Longitudinal inscription would not have been possible without damaging the electrode and/or the alignment layer of the cell. To make transversal inscription possible, the top edge of the cell had to be optically polished. During this process, polishing fluid inevitably enters the cell due to capillary forces. The

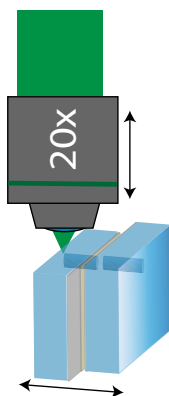


FIGURE 6.1. Layout for inscribing waveguides into the ECB cell.

areas that were left unaffected by polishing fluid were picked out as the locations for inscribing waveguides.

Waveguides were inscribed into the liquid crystal cell using the setup given in figure 3.1. The anamorphic zoom system presented in section 4.3 was used to shape the beam during the inscription process. Since the rim of the liquid crystal cell is blocked by the glue and spacer mixture holding the two glass slides together, the waveguides were inscribed 0.6 mm below the surface. This is significantly deeper inside the material than all the waveguides inscribed in this thesis to far. At this depth, nonlinear propagation effects and aberrations occur, which make it necessary to adjust the waveguide parameters to still allow good guiding properties of the waveguides. Therefore, the waveguides were inscribed with $0.66 \mu\text{J}$ pulse energy and 45 mm min^{-1} scanning velocity. Mode fields of the waveguides are shown in figure 6.2. The modefield at 633 nm has a width of $6.9 \mu\text{m}$ in x and $9.6 \mu\text{m}$ in y , while the modefield at 808 nm has widths of $9.7 \mu\text{m}$ and $11.1 \mu\text{m}$ in x and y , respectively. Microscope images of the resulting waveguide facets are given in figure 6.3a.

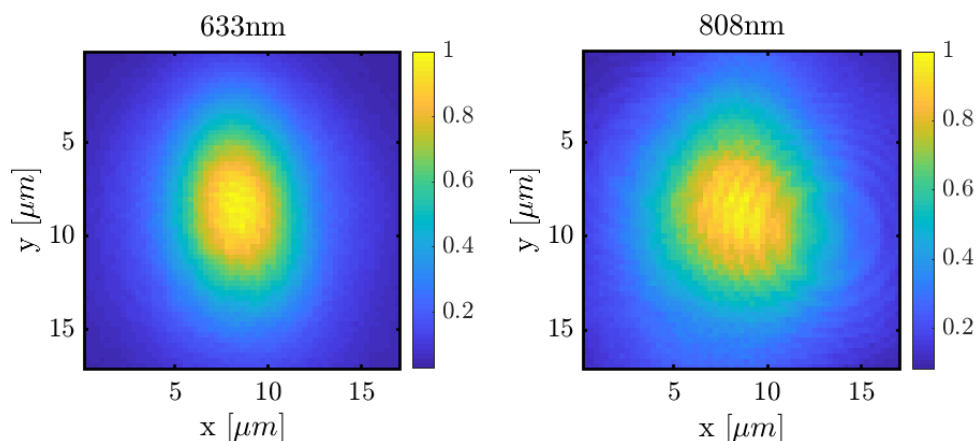


FIGURE 6.2. Modefields of the waveguides inscribed into the liquid crystal cell at 633 nm and 808 nm probing wavelength.

A gap of 0.1 mm was left in the waveguide, centered around the interface of the two glass substrates, to avoid damaging the electrodes and the alignment layer. This damage was clearly visible for slow inscription speeds when no gap was left during the inscription process. Microscopy images of the induced damage are given in figure 6.3b. The consequence of this gap on the losses can be estimated by taking the overlap integral (equation 2.29) of the waveguide mode field and the mode field after $92 \mu\text{m}$ propagation in fused silica and $8 \mu\text{m}$ propagation in the liquid crystal (for simplicity reasons neglecting the different refractive indices of the electrode and the alignment layer). It was found that the losses due to the gap amount to 0.03 dB at 808 nm and to 0.04 dB at 633 nm.

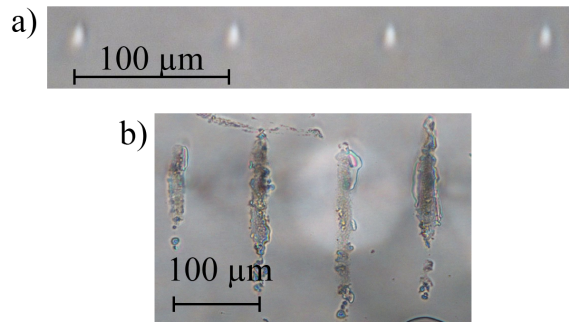


FIGURE 6.3. Transmission microscopy images of a) the inscribed waveguides in the liquid crystal cell, b) damage that can occur when inscribing through the electrodes and alignment layer.

The liquid crystal mixture used for the experiments is E7 (Synthon chemicals). The cell was filled after the waveguide inscription. For this purpose, the empty cell is placed into a puddle of liquid crystal in a Petri dish. The Petri dish is then sealed into a plastic bag under low pressure using a gastronomy vacuum sealer. When the bag is reopened, the pressure difference aids in sucking liquid crystal into the cell. Unfortunately, it was not possible to fill the cell without air bubbles using this procedure. Fortunately, however, the air bubbles did not occur where waveguides were inscribed.

6.2. Electro-optical modulation of the output polarization

Liquid crystals can be rotated by external electric fields. In this section, this properties of liquid crystals will be used to change the polarization state in a waveguide with different applied sinusoidal voltages at 1 kHz frequency. The characterization of the sample was done using setup 3.2b without the analyzer, with a helium-neon laser running at 633 nm as the light source and a polarimeter as the detector. The liquid crystal cell is positioned so that the rubbing of the polyimide is along y-direction, in line with the polarization direction of horizontal polarization, defining the optical axis of the liquid crystal layer. This means that the strongest birefringent response of the cell can be obtained with diagonal or antidiagonal input polarization.

In a first step, the functionality of the sample is investigated by measuring the polarization change for a section of the liquid crystal cell in which no waveguide has been inscribed. For this purpose the objectives in the characterization setup were removed, so that the characterization beam was collimated. The polarization of the beam before the cell was set to diagonal and the power was set to 0.5 mW. After applying a specific voltage, it was waited until the output polarization on the polarimeter did not change, before measuring the polarization, to ensure that the liquid crystals had completed their rotation. The duration of such a rotation was on

the order of seconds. The measured output polarization states (in terms of Stokes parameters), depending on the voltage applied to the cell, are shown in figure 6.4. A clear change of the output polarization with the applied voltage is visible, verifying that the liquid crystal cell is functional. The initial output polarization given at $0 V_{\text{rms}}$

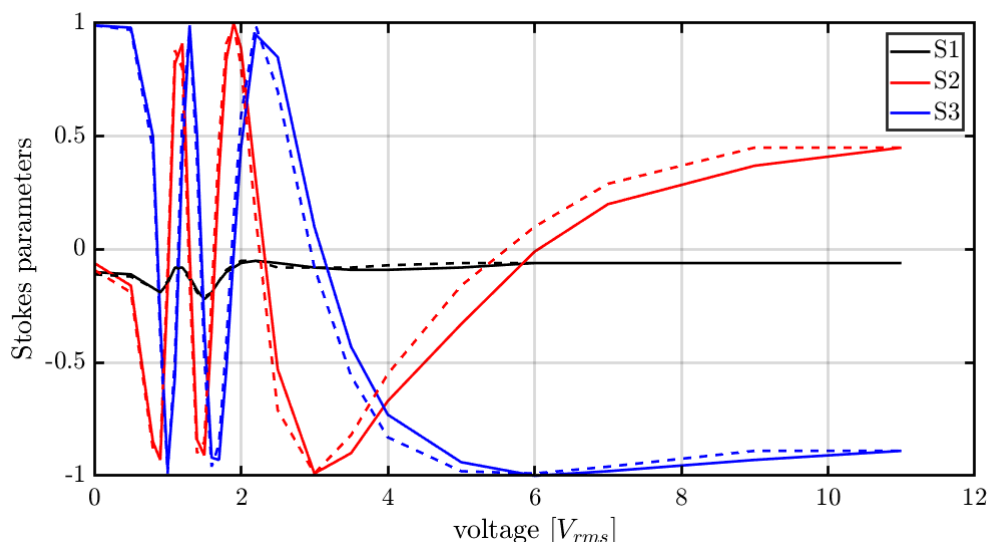


FIGURE 6.4. Change of Stokes parameters with applied voltage of the liquid crystal cell without a waveguide, using light of 633 nm wavelength. Solid lines correspond to the measured values when the voltage is increased, dashed lines show the Stokes parameters when the voltage was decreased.

is the result of the input polarization combined with the birefringence of the liquid crystals in their initial state. The Fréedericksz transition occurs at around $0.5 V_{\text{rms}}$. With increasing applied voltage, the output polarization changes. A rotation on the stokes sphere is observed, given by the strong variation of the Stokes parameters S_2 and S_3 . The strongest change is seen for voltages up to $3 V_{\text{rms}}$. After this, the ability of the applied voltage to further rotate the liquid crystals decreases, visible by a significant slower change of the output polarization. At around $10 V_{\text{rms}}$, the rotation of the liquid crystals stagnates. An overall rotation of around 5π is observed. The Stokes parameter S_1 changes slightly during the measurement. It is particularly not zero, as would be expected if we model the cell as a linear retarder with an optical axis at 0° to the horizontal axis. This may be caused by a slight tilt of the liquid crystal cell in the setup. To show the accuracy and reproducibility of the results, the voltage is first increased up to $11 V_{\text{rms}}$ and then decreased back to $0 V_{\text{rms}}$. The measured data during the increase of the voltage is given in figure 6.4 by the solid lines, the data acquired while lowering the voltage is given by the dashed lines. For low voltages, both measurements yield similar results. Only for voltages higher than

6.2. ELECTRO-OPTICAL MODULATION OF THE OUTPUT POLARIZATION

$3V_{\text{rms}}$ slight deviations can be seen, which might be due to misalignment, which can limit the polarimeter's measurement accuracy.

From the results in figure 6.4, we can retrieve the optical retardance of the liquid crystal layer for light of wavelength 633 nm. Based on Mueller calculus and the matrix definitions in table 2.2, the liquid crystal layer can be modeled as a waveplate of retardation δ , rotated by an angle θ . The value for δ will be larger than 5π , since a larger rotation was observed in figure 6.4. Knowing the output Stokes vector \vec{S}_{out} when no voltage is applied to the cell, the following equation can be written:

$$\begin{aligned} \vec{S}_{out} = \begin{pmatrix} 1 \\ -0.1 \\ -0.06 \\ 0.99 \end{pmatrix} &= \overset{\leftrightarrow}{R}(\theta) \begin{pmatrix} 1 & 0 & 0 & 0 \\ 0 & 1 & 0 & 0 \\ 0 & 0 & \cos(\delta) & \sin(\delta) \\ 0 & 0 & -\sin(\delta) & \cos(\delta) \end{pmatrix} R(-\theta) \begin{pmatrix} 1 \\ 0 \\ 1 \\ 0 \end{pmatrix} \\ &= \begin{pmatrix} 1 \\ \cos(2\theta) \sin(2\theta) - \cos(\delta) \cos(2\theta) \sin(2\theta) \\ \cos(\delta) \cos(2\theta)^2 + \sin(2\theta)^2 \\ -\cos(2\theta) \sin(\delta) \end{pmatrix} \end{aligned} \quad (6.1)$$

The resulting over-determined equation system was solved using a nonlinear system solver (MATLAB fsolve). The resulting values for the rotation and the retardation were found to be $\theta = -0.015\pi \approx -2.7^\circ$ and $\delta = 5.48\pi$. This optical retardation corresponds to an optical path difference of $1.73 \mu\text{m}$. Comparing this to the birefringence value $\Delta n = 0.225$ of the E7 liquid crystal mixture as given in section 2.5.4 (neglecting dispersion effects), this indicates that the liquid crystal cell has a thickness of $1.73 \mu\text{m}/0.225 \approx 7.69 \mu\text{m}$, which fits well to the $(8.0 \pm 0.8) \mu\text{m}$ gap specified by the manufacturer.

To investigate the performance of the liquid crystal cell in combination with the waveguides, the objectives were inserted back into the characterization setup and the light of the helium neon laser is coupled into an inscribed waveguide of the cell. The input power was kept at 0.5 mW and the input polarization remained diagonal. The polarization of the output mode field was then measured using the polarimeter. The results are plotted in figure 6.5. During this measurement, no significant difference between the measurements taken with increasing and decreasing voltage were measured, as can be seen in the figure 6.5 by comparing the dashed and the solid lines. The course of the rotation of the polarization state on the Stokes sphere for voltages up to $3V_{\text{rms}}$ is visualized in figure 6.6.

The initial output polarization of the waveguide without an applied external electric field is given at $0V_{\text{rms}}$ and visualized in figure 6.6a. This polarization differs from

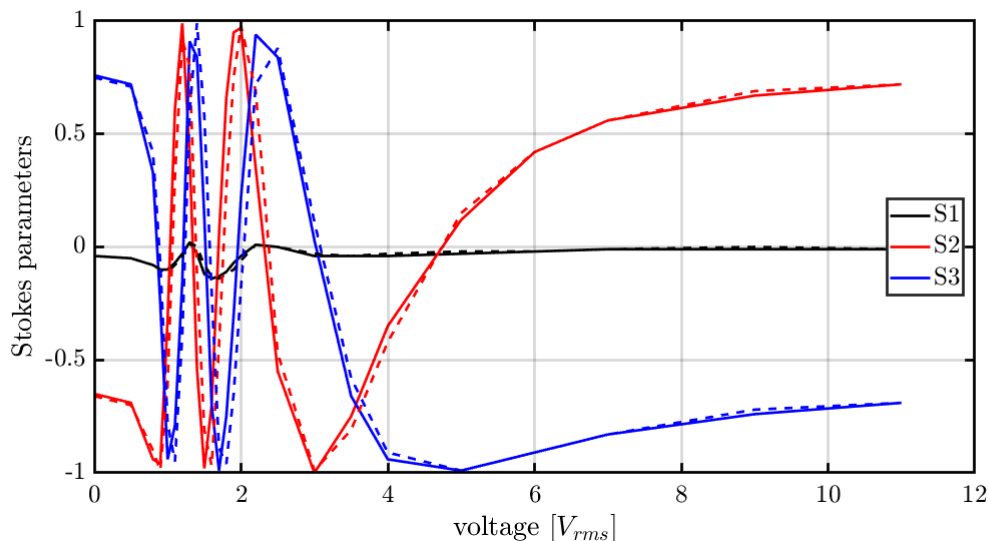


FIGURE 6.5. Change of output polarization of a waveguide with embedded liquid crystal layer when the applied voltage is changed. The wavelength used for this measurement was 633 nm and the input polarization was diagonal. Solid lines correspond to the measured values when the voltage is increased, dashed lines show the Stokes parameters when the voltage was decreased.

the polarization at $0 V_{rms}$ of figure 6.4 due to the birefringence of the waveguide. Apart from this offset, the qualitative rotation of the output polarization on the Stokes sphere resembles the rotation in the liquid crystal cell without the waveguide. The output polarization changes strongly with the voltage for voltages up to around $3 V_{rms}$. At around $0.9 V_{rms}$, antidiagonal output polarization is reached. Further increasing the voltage up to $1.2 V_{rms}$ allows a switch of the output polarization to diagonal polarization, as visualized in figure 6.6b. At $1.5 V_{rms}$, the output polarization returns back to antidiagonal polarization (see figure 6.6c), and then at $1.9 V_{rms}$ back to diagonal polarization (see figure 6.6d). With an applied voltage of $3.0 V_{rms}$, antidiagonal polarization is reached again (see figure 6.6e).

Based on what was shown for the measurement without a waveguide, the output polarization state of the waveguide can be used to retrieve the birefringence of the waveguide using Mueller calculus. To do this, an analogous equation system to equation 6.1 was set up, where the waveguide pieces were modelled as two additional identical waveplates, one before and one after the liquid crystal layer. The model revealed that the optical axis of the waveguides was at 97° with respect to horizontal polarization and that the retardation per waveguide piece was 0.1π . This corresponds to an optical path difference of 32 nm. Normalizing this to the waveguide length results in an optical path difference per centimeter of 107 nm. This is a significantly higher birefringence to what was observed for previous waveguides inscribed with

6.2. ELECTRO-OPTICAL MODULATION OF THE OUTPUT POLARIZATION

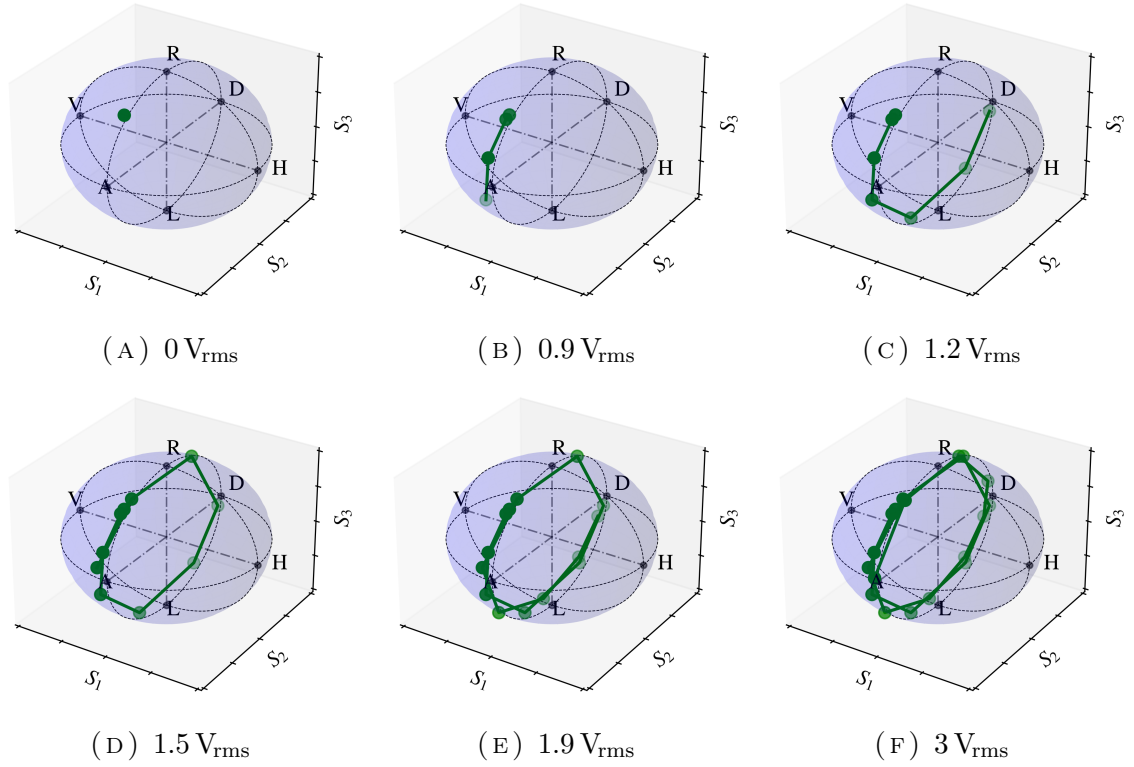


FIGURE 6.6. Rotation of the output polarization state of the waveguide with the applied voltage for light of 633 nm wavelength.

the anamorphic zoom system in this thesis. The reason for this is the changed inscription parameters, which were chosen to produce waveguides 0.6 mm below the surface (avoiding the edge of the cell where the glue and spacer mixture are positioned), whilst at the same time yielding strong modification, making it easy to find the waveguide in the sample. An increased birefringence was tolerated in this case. However, for further investigations, the writing parameters should be adapted to provide minimum birefringence.

The waveguide with embedded liquid crystals can also be operated at other wavelengths, for example, at 808 nm. A measurement showing the change of Stokes parameter with the applied voltage is given in figure 6.7. The input polarization for this measurement was antidiagonal polarization, and the input power was 0.5 mW. There are several similarities between figure 6.5, measured with 633 nm wavelength, and figure 6.7, measured with 808 nm wavelength. In both images, mainly the Stokes parameters S_2 and S_3 are modulated. This modulation is strong for voltages up to $3 V_{\text{rms}}$, and then stagnates. The initial output polarization is different though, and not just by the sign of the Stokes parameters, as would be expected by the change from diagonal to antidiagonal input polarization. Furthermore, the overall change in phase delay achieved with light of 808 nm wavelength is just under 4π , which is less

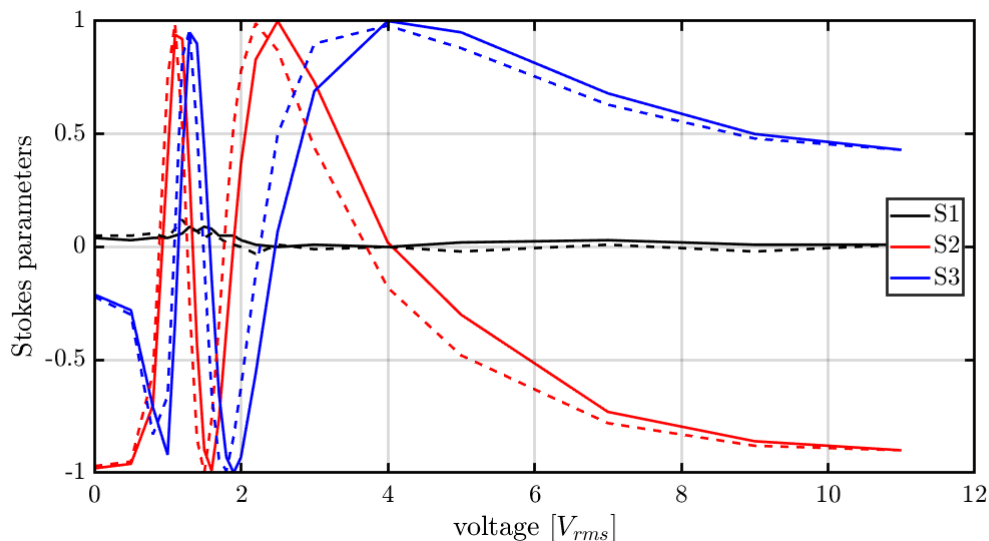


FIGURE 6.7. Change of output polarization depending on applied voltage for light of 808 nm wavelength and 0.5 mW input power. The input polarization was antidiagonal.

than the roughly 5π achieved with light of 633 nm wavelength. Both is because at a given optical path difference OPD , caused by the birefringence of the liquid crystal (neglecting dispersion effects), the phase delay δ of the light scales antiproportional to the wavelength: $\delta = 2\pi OPD/\lambda$.

For many practical purposes, achieving a single 2π rotation on the Stokes sphere is sufficient to allow arbitrary output polarization states of a waveguide. Choosing a liquid crystal cell with a thinner liquid crystal layer would therefore be a good idea for future devices, since this would help reduce the size of the device without any reduction in functionality. However, in general it is necessary to note that if the embedded liquid crystal layer is to be used for multiple wavelengths, the possible rotation of the output polarization on the Stokes sphere must be at least 2π for the longest wavelength, which means that for shorter wavelength rotations of more than 2π are necessary. To expand the here proposed approach further, future investigations should focus on how to change the alignment of the liquid crystals, so that not only the amount of retardation can be tuned, but also the optical axis of the retardation.

To conclude, in this section active electro-optical reconfiguration of the output polarization state of an FLDW waveguide by embedding an $8\ \mu\text{m}$ thin liquid crystal layer into the waveguide was demonstrated for the first time. Full rotations on the Stokes sphere were observed, proving that a strong modulation of the output polarization is possible using this approach. Currently existing approaches to add reconfigurable elements into FLDW circuits are based either on heat elements in

6.2. ELECTRO-OPTICAL MODULATION OF THE OUTPUT POLARIZATION

Mach-Zahnder interferometers [153, 154] or on a strong laser inducing the Kerr effect in a directional coupler [160, 161]. A downside of using thermal shifters as reconfigurable elements is that they suffer from thermal dissipation, which limits how many of these devices can be closely packed due to cross-talk. Furthermore, neither the approach using thermal effects nor the approach using the Kerr effect were used to change the polarization of the transmitted light. So far, the only tuneable element in glass-based FLDW circuits designed to change the polarization state of a waveguide is the liquid crystal based approach, which was presented in this thesis.

CHAPTER 7

Conclusion and Outlook

Polarization control in FLDW photonic devices is an important building block for integrated circuit design. Complete control over the polarization of the photon is critical for using as many degrees of freedom as possible to encode the information carried by a photon, thereby increasing the data rate per photon. The goal of this thesis was to achieve full control over the polarization in FLDW fused silica waveguides.

The first prerequisite for this goal is achieving waveguides with minimal birefringence and losses. It has been shown that parameter optimizations can improve the properties of the waveguide, but is not sufficient to yield the desired performance. Therefore, the opportunity of spatial beam shaping for reducing waveguide birefringence was investigated. Initially, a cylindrical telescope was used to achieve an elliptical inscription beam, which already improved the waveguide properties.

To take things further, this approach was optimized, resulting in the first use of an anamorphic zoom system for the laser inscription of waveguides in glass. Using this approach, waveguides with competitive loss values and at the same time significantly reduced birefringence compared to typical birefringences of FLDW waveguides were achieved.

The next step towards full control over the polarization state in FLDW waveguides is the targeted insertion of custom polarization manipulating structures into the waveguide. For this purpose, two innovative approaches were presented in this thesis, firstly the use of locally embedded nanogratings as retardation elements and secondly the usage of a tuneable liquid crystal layer within the FLDW waveguide.

The utilization of nanogratings as local retardation elements requires precise control over their linear optical retardance and the orientation of their optical axis. It was confirmed that by suitable choice of inscription parameters, the properties of nanogratings can be changed to produce structures that exhibit tailored linear retardation at any desired optical axis orientation. Within the framework of this study, the influence of the different elliptical beam shaping approaches –previously used to optimize waveguide parameters –on the nanograting properties were investigated. Nanogratings with highest birefringence at lowest losses were found with elliptical beam shaping using the cylindrical telescope. Based on these results,

quantum gates made of nanogratings embedded into waveguides were demonstrated for the first time and characterized using single photons. The key in this case, to enable a full rotation of the nanograting orientation with respect to the waveguide, is to inscribe the nanogratings from a direction perpendicular to the waveguide inscription. Compared to former approaches for single qubit quantum gates in FLDW waveguides, these nanograting-based quantum gates were two orders of magnitude more compact due to the high birefringence of the nanogratings. This is an important aspect for reducing the footprint of future glass-based integrated photonic quantum circuits.

Furthermore, it was investigated for the first time in this thesis how conical phase front beam shaping affects the optical properties of nanogratings. When changing the conical phase front angle, the depth of the modification in the glass sample changed without any mechanical translation of either the inscription lens or the sample. At the same time, the optical properties of the nanogratings, like birefringence, dichroism, and losses, were greatly influenced by the conical phase front angle of the inscription beam. It was observed that negative conical phase front angles resulted in a thickening of nanograting modifications in the beam inscription direction, which was not the case with positive conical phase front angles. Simulations revealed that this asymmetry was caused by nonlinear propagation effects.

The optical properties of the nanogratings produced with positive and negative conical phase front angles were also different from each other. The highest optical path differences and dichroism were seen for a single modification layer generated with a negative conical phase front angle. However, when the optical path difference and dichroism of nanogratings generated with negative conical phase fronts are normalized to their thickness, it becomes clear that this increase is solely due to accumulation by the thick modification and not due to a higher birefringence or dichroism per volume element. In fact, the highest birefringence (i.e., optical path difference normalized to modification thickness) and dichroism normalized to thickness were obtained with positive conical phase front angles. This means that by using conical phase front angles to shape the beam for nanograting inscription, the thickness and retardation of a structure can be chosen independently by creating either lower birefringent but thicker structures with negative conical phase front angles or multiple layers of higher birefringent but thinner structures with positive conical phase front angles, both resulting in the same total thickness, but having different optical retardations. The obtained results also reveal that using conical phase front beam shaping for nanograting inscription can help decrease transmission loss rates.

Finally, the first actively reconfigurable polarization control in glass-based FLDW waveguides was demonstrated in this thesis by embedding a thin liquid crystal layer into a waveguide. This approach allows changing the output polarization state of a waveguide by changing the voltage applied to the liquid crystal layer. A 5π -rotation of the output polarization state on the Poincaré sphere was observed for transmitted light of wavelength of 633 nm in an 8 μm thin liquid crystal layer.

Comparing both presented approaches of polarization control, it can be said that each one has its own advantages. The advantages of the approach of using nanogratings are, firstly, that the nanogratings can easily be rotated 360 degrees by changing the inscription polarization direction. Furthermore, they are well confined in the sample because they are a volume modification that cannot leak, unlike liquid crystals. In addition, nanogratings are much more temperature stable than liquid crystals. The obvious advantage of liquid crystals over nanogratings is their tuneability by external fields that can change the optical retardation of the liquid crystal layer. However, in a typical liquid crystal cell, the orientation of the optical axis is fixed by the alignment layer. One way to overcome this limitation for a given alignment layer is to use a pump-probe configuration, which should allow the liquid crystal director to be rearranged according to the electric field of the pump beam. This will have to be further investigated in the future. To further advance the integration of the pump-probe setup, the use of Bragg gratings within the waveguide piece following the liquid crystal layer could be an elegant way to remove the pump after the liquid crystal cell. Alternatively, other ways to reconfigure the alignment layer of the liquid crystal cell could be explored, such as reversible photoalignment of the liquid crystals.

The layout of the liquid crystal sample is not yet ideal for combining waveguides with liquid crystal layers. It would be advantageous if the cell could be fabricated in such a way that no polishing of the assembled cell is necessary, so that no polishing fluid gets into the volume intended for the liquid crystals. One option would be laser ablation of the cavity, but this would require new solutions for adding the alignment layer. In general, it would be interesting to change the materials for the alignment layers and electrodes to bring the waveguides closer to the liquid crystal layer without causing damage in these layers. One could also imagine completely different geometries, such as a waveguide extending just below the surface of a liquid crystal layer, so that the evanescent tails of the guided mode field could be modified by the liquid crystals.

In summary, different approaches of controlling polarization in FLDW circuits have been investigated in this work. First, the reduction of birefringence in FLDW waveguides was achieved, and second, novel approaches to fabricate embedded

waveplates using either nanogratings or liquid crystals were demonstrated. Based on the results of this work, new integrated photonic circuits can be developed that use polarization to encode the transmitted information. The approaches developed in this thesis allow the defined setting of polarization state in waveguides, while at the same time paving the way to achieving significantly more compact FLDW photonic circuits in glass. The results have a high relevance for application fields ranging from augmented reality devices to optical information technology and optical computing.

Bibliography

- [1] David D Nolte et al. *Mind at light speed: A new kind of intelligence*. Simon and Schuster, 2001.
- [2] Jeremy L O’Brien. “Optical quantum computing”. In: *Science* 318.5856 (2007), p. 1567.
- [3] Han-Sen Zhong et al. “Quantum computational advantage using photons”. In: *Science* 370.6523 (2020), pp. 1460–1463.
- [4] Robert G Hunsperger. *Integrated Optics: Theory and Technology*. Springer Science & Business Media, 2009.
- [5] Jerome Lapointe et al. “Making smart phones smarter with photonics”. In: *Optics express* 22.13 (2014), pp. 15473–15483.
- [6] Malcolm Homan. “The use of optical waveguides in head up display (HUD) applications”. In: *Display Technologies and Applications for Defense, Security, and Avionics VII*. Vol. 8736. International Society for Optics and Photonics. 2013, 87360E.
- [7] Vincent Brac de la Perrière. “Understanding waveguide-based architecture and ways to robust monolithic optical combiner for smart glasses”. In: *Digital Optics for Immersive Displays*. Vol. 10676. International Society for Optics and Photonics. 2018, p. 106761D.
- [8] Dezhi Tan et al. “Photonic circuits written by femtosecond laser in glass: improved fabrication and recent progress in photonic devices”. In: *Advanced Photonics* 3.2 (2021), p. 024002.
- [9] M Ciampini et al. “Path-polarization hyperentangled and cluster states of photons on a chip”. In: *Light: Science & Applications* 5.4 (2016), e16064.
- [10] Eugene Hecht. *Optics*. Pearson Education Limited, 2017.
- [11] Herbert Daniel. *Physik: Optik, Thermodynamik, Quanten*. Vol. 3. Walter de Gruyter, 1998.
- [12] Demtröder. *Experimentalphysik and Experimentalphysik, Band 2, Elektrizität und Optik*. Springer, 2017.
- [13] Max Born and Emil Wolf. *Principles of optics: electromagnetic theory of propagation, interference and diffraction of light*. Elsevier, 2013.
- [14] Bahaa E. A. Saleh and Malvin Carl Teich. “Fundamentals of photonics”. In: John Wiley & Sons, 1991. Chap. 18, p. 699.
- [15] John Kerr. “XL. A new relation between electricity and light: Dielectric media birefringent”. In: *The London, Edinburgh, and Dublin Philosophical Magazine and Journal of Science* 50.332 (1875), p. 337.
- [16] MI Freiser. “A survey of magneto-optic effects”. In: *IEEE Transactions on magnetics* 4.2 (1968), p. 152.
- [17] Philippe Lalanne and Dominique Lemerçier-Lalanne. “Depth dependence of the effective properties of subwavelength gratings”. In: *JOSA A* 14.2 (1997), pp. 450–459.

BIBLIOGRAPHY

- [18] Max Born and Emil Wolf. “Principles of optics”. In: *Pergamon Press* 6.188 (1980).
- [19] Michael Bass et al. *Handbook of optics, Volume II: Design, fabrication and testing, sources and detectors, radiometry and photometry, Second Edition*. McGraw-Hill, Inc., 1995.
- [20] R Clark Jones. “A new calculus for the treatment of optical systems: I Description and discussion of the calculus”. In: *J. Opt. Soc. Am.* 31 (1941), p. 488.
- [21] Henry Hurwitz and R Clark Jones. “A new calculus for the treatment of optical systemsii. proof of three general equivalence theorems”. In: *JOSA* 31.7 (1941), p. 493.
- [22] R Clark Jones. “A new calculus for the treatment of optical systemsiii. the sohncke theory of optical activity”. In: *Josa* 31.7 (1941), p. 500.
- [23] R Clark Jones. “A new calculus for the treatment of optical systems. IV.” In: *Josa* 32.8 (1942), p. 486.
- [24] R Clark Jones. “A New Calculus for the Treatment of Optical SystemsVI. Experimental Determination of the Matrix”. In: *JOSA* 37.2 (1947), p. 110.
- [25] R Clark Jones. “A new calculus for the treatment of optical systemsv. A more general formulation, and description of another calculus”. In: *JOSA* 37.2 (1947), p. 107.
- [26] R Clark Jones. “A new calculus for the treatment of optical systems. VII. Properties of the N-matrices”. In: *Josa* 38.8 (1948), p. 671.
- [27] R Clark Jones. “New calculus for the treatment of optical systems. VIII. Electromagnetic theory”. In: *Josa* 46.2 (1956), p. 126.
- [28] BJ Thompson, D Goldstein, and DH Goldstein. *Polarized Light, Revised and Expanded*. 2003.
- [29] George Gabriel Stokes. “On the composition and resolution of streams of polarized light from different sources”. In: *Transactions of the Cambridge Philosophical Society* 9 (1851), p. 399.
- [30] Henri Poincaré. *Théorie mathématique de la lumière II.: Nouvelles études sur la diffraction.—Théorie de la dispersion de Helmholtz. Leçons professées pendant le premier semestre 1891-1892*. Vol. 1. G. Carré, 1889.
- [31] G Deschamps and P Mast. “Poincaré sphere representation of partially polarized fields”. In: *IEEE Transactions on Antennas and Propagation* 21.4 (1973), p. 474.
- [32] A Satya Narayanan and Swapan K Saha. *Waves and oscillations in nature: an introduction*. CRC Press, 2015.
- [33] Nathan Grieb Parke III. “Optical algebra”. In: *Journal of Mathematics and Physics* 28.1-4 (1949), p. 131.
- [34] AW Snyder and J Love. *Optical Waveguide Theory*. Vol. 190. Springer Science & Business Media, 1983.
- [35] María L Calvo and Vasudevan Lakshminarayanan. *Optical waveguides: from theory to applied technologies*. CRC Press, 2018.
- [36] Jonathan Hu and Curtis R Menyuk. “Understanding leaky modes: slab waveguide revisited”. In: *Advances in Optics and Photonics* 1.1 (2009), pp. 58–106.
- [37] Jürgen Jahns and Stefan Helfert. *Introduction to micro- and nanooptics*. John Wiley & Sons, 2012.

- [38] Kenichi Iga and Yasuo Kokubun. “OPTICAL COUPLING OF LASER AND FIBER”. In: *Encyclopedic Handbook of Integrated Optics* (2005), p. 192.
- [39] C-A Bunge, M Beckers, and B Lustermann. “Basic principles of optical fibres”. In: *Polymer Optical Fibres*. Elsevier, 2017, pp. 47–118.
- [40] Matthias Lenzner et al. “Femtosecond optical breakdown in dielectrics”. In: *Physical review letters* 80.18 (1998), p. 4076.
- [41] SK Sundaram and Eric Mazur. “Inducing and probing non-thermal transitions in semiconductors using femtosecond laser pulses”. In: *Nature materials* 1.4 (2002), pp. 217–224.
- [42] Kazuyoshi Itoh et al. “Ultrafast processes for bulk modification of transparent materials”. In: *MRS bulletin* 31.8 (2006), p. 620.
- [43] Wolfgang Demtröder. *Experimentalphysik 3: Atome, Moleküle und Festkörper*. Springer-Verlag, 2010.
- [44] Kotaro Obata et al. “Enhance refractive index modification of fused silica by multiwavelength excitation process using F² and KrF excimer lasers”. In: *RIKEN REVIEW* (2003), pp. 42–46.
- [45] Rafael R Gattass and Eric Mazur. “Femtosecond laser micromachining in transparent materials”. In: *Nature photonics* 2.4 (2008), pp. 219–225.
- [46] Chris B Schaffer, Andre Brodeur, and Eric Mazur. “Laser-induced breakdown and damage in bulk transparent materials induced by tightly focused femtosecond laser pulses”. In: *Measurement Science and Technology* 12.11 (2001), p. 1784.
- [47] LV Keldysh et al. “Ionization in the field of a strong electromagnetic wave”. In: *Sov. Phys. JETP* 20.5 (1965), pp. 1307–1314.
- [48] SS Mao et al. “Dynamics of femtosecond laser interactions with dielectrics”. In: *Applied Physics A* 79.7 (2004), pp. 1695–1709.
- [49] Brent C Stuart et al. “Optical ablation by high-power short-pulse lasers”. In: *JOSA B* 13.2 (1996), p. 459.
- [50] B C Stuart et al. “Nanosecond-to-femtosecond laser-induced breakdown in dielectrics”. In: *Physical review B* 53.4 (1996), p. 1749.
- [51] Baoshan Guo et al. “Femtosecond laser micro/nano-manufacturing: theories, measurements, methods, and applications”. In: *Nanomanufacturing and Metrology* 3.1 (2020), pp. 26–67.
- [52] K Miura Davis et al. “Writing waveguides in glass with a femtosecond laser”. In: *Optics letters* 21.21 (1996), p. 1729.
- [53] Alexander M Streltsov and Nicholas F Borrelli. “Study of femtosecond-laser-written waveguides in glasses”. In: *JOSA B* 19.10 (2002), pp. 2496–2504.
- [54] Roberto Osellame et al. “Femtosecond writing of active optical waveguides with astigmatically shaped beams”. In: *JOSA B* 20.7 (2003), p. 1559.
- [55] Roberto Osellame et al. “Optical waveguide writing with a diode-pumped femtosecond oscillator”. In: *Optics letters* 29.16 (2004), pp. 1900–1902.
- [56] Feng Chen and JR Vázquez de Aldana. “Optical waveguides in crystalline dielectric materials produced by femtosecond-laser micromachining”. In: *Laser & Photonics Reviews* 8.2 (2014), pp. 251–275.
- [57] Yuechen Jia, Shixiang Wang, and Feng Chen. “Femtosecond laser direct writing of flexibly configured waveguide geometries in optical crystals: fabrication and application”. In: *Opto-Electronic Advances* 3.10 (2020), pp. 190042–1.

- [58] Roberto Osellame et al. “Femtosecond laser writing of waveguides in periodically poled lithium niobate preserving the nonlinear coefficient”. In: *Applied physics letters* 90.24 (2007), p. 241107.
- [59] Henry T Bookey et al. “Femtosecond Laser Inscription of Low Insertion Loss Waveguides in Z-Cut Lithium Niobate”. In: *IEEE Photonics Technology Letters* 19.12 (2007), pp. 892–894.
- [60] Belén Sotillo et al. “Diamond photonics platform enabled by femtosecond laser writing”. In: *Scientific reports* 6.1 (2016), pp. 1–9.
- [61] Dmitrii Perevoznik et al. “Writing 3D Waveguides with Femtosecond Pulses in Polymers.” In: *Journal of Lightwave Technology* (2021).
- [62] Welm M Pätzold et al. “Cascaded-focus laser writing of low-loss waveguides in polymers”. In: *Optics letters* 41.6 (2016), pp. 1269–1272.
- [63] Arnaud Zoubir et al. “Femtosecond laser fabrication of tubular waveguides in poly (methyl methacrylate)”. In: *Optics letters* 29.16 (2004), pp. 1840–1842.
- [64] Matthias Pospiech et al. “Single-sweep laser writing of 3D-waveguide devices”. In: *Optics express* 18.7 (2010), pp. 6994–7001.
- [65] Stefan Nolte et al. “Femtosecond waveguide writing: a new avenue to three-dimensional integrated optics”. In: *Applied Physics A* 77.1 (2003), pp. 109–111.
- [66] Jiaren Liu et al. “Directly writing of 1-to-N optical waveguide power splitters in fused silica glass using a femtosecond laser”. In: *Optics communications* 253.4-6 (2005), pp. 315–319.
- [67] Masaaki Sakakura et al. “Fabrication of three-dimensional 1×4 splitter waveguides inside a glass substrate with spatially phase modulated laser beam”. In: *Optics express* 18.12 (2010), pp. 12136–12143.
- [68] Robert R Thomson et al. “Ultrafast-laser inscription of a three dimensional fan-out device for multicore fiber coupling applications”. In: *Optics express* 15.18 (2007), pp. 11691–11697.
- [69] Yang Liao et al. “Rapid prototyping of three-dimensional microfluidic mixers in glass by femtosecond laser direct writing”. In: *Lab on a Chip* 12.4 (2012), pp. 746–749.
- [70] Yasuhiko Shimotsuma et al. “Application of femtosecond-laser induced nanostructures in optical memory”. In: *Journal of nanoscience and nanotechnology* 7.1 (2007), pp. 94–104.
- [71] EN Glezer et al. “Three-dimensional optical storage inside transparent materials”. In: *Optics letters* 21.24 (1996), p. 2023.
- [72] Lionel Sudrie et al. “Writing of permanent birefringent microlayers in bulk fused silica with femtosecond laser pulses”. In: *Optics Communications* 171.4-6 (1999), p. 279.
- [73] John D Mills et al. “Embedded anisotropic microreflectors by femtosecond-laser nanomachining”. In: *Applied physics letters* 81.2 (2002), pp. 196–198.
- [74] James W Chan et al. “Structural changes in fused silica after exposure to focused femtosecond laser pulses”. In: *Optics letters* 26.21 (2001), p. 1726.
- [75] James W Chan et al. “Modification of the fused silica glass network associated with waveguide fabrication using femtosecond laser pulses”. In: *Applied Physics A* 76.3 (2003), p. 367.
- [76] Frank L Galeener. “Raman and ESR studies of the thermal history of amorphous SiO₂”. In: *Journal of Non-Crystalline Solids* 71.1-3 (1985), p. 373.

- [77] Linards Skuja, Hideo Hosono, and Masahiro Hirano. “Laser-induced color centers in silica”. In: *Laser-Induced Damage in Optical Materials: 2000*. Vol. 4347. International Society for Optics and Photonics. 2001, pp. 155–168.
- [78] Jean-Philippe Bérubé and Réal Vallée. “Femtosecond laser direct inscription of surface skimming waveguides in bulk glass”. In: *Optics letters* 41.13 (2016), p. 3074.
- [79] C Hnatovsky et al. “Pulse duration dependence of femtosecond-laser-fabricated nanogratings in fused silica”. In: *Applied Physics Letters* 87.1 (2005), p. 014104.
- [80] Dominik Blömer et al. “Nonlinear refractive index of fs-laser-written waveguides in fused silica”. In: *Optics express* 14.6 (2006), p. 2151.
- [81] Lawrence Shah et al. “Waveguide writing in fused silica with a femtosecond fiber laser at 522 nm and 1 MHz repetition rate”. In: *Optics express* 13.6 (2005), p. 1999.
- [82] Uri Levy, Yaron Silberberg, and Nir Davidson. “Mathematics of vectorial Gaussian beams”. In: *Advances in Optics and Photonics* 11.4 (2019), pp. 828–891.
- [83] Vítor A Amorim et al. “Loss mechanisms of optical waveguides inscribed in fused silica by femtosecond laser direct writing”. In: *Journal of Lightwave Technology* 37.10 (2019), pp. 2240–2245.
- [84] Wilbur J Reichman et al. “Spectroscopic characterization of different femtosecond laser modification regimes in fused silica”. In: *JOSA B* 24.7 (2007), p. 1627.
- [85] Shane M Eaton et al. “Heat accumulation effects in femtosecond laser-written waveguides with variable repetition rate”. In: *Optics Express* 13.12 (2005), p. 4708.
- [86] Shane Eaton et al. “Thermal heating effects in writing optical waveguides with 0.1-5 MHz repetition rate”. In: *Photon Processing in Microelectronics and Photonics IV*. Vol. 5713. International Society for Optics and Photonics. 2005, p. 35.
- [87] VR Bhardwaj et al. “Stress in femtosecond-laser-written waveguides in fused silica”. In: *Optics letters* 29.12 (2004), p. 1312.
- [88] Jonathan J Witcher et al. “Thermal annealing of femtosecond laser written structures in silica glass”. In: *Optical Materials Express* 3.4 (2013), p. 502.
- [89] A Saliminia et al. “Writing optical waveguides in fused silica using 1 kHz femtosecond infrared pulses”. In: *Journal of Applied Physics* 93.7 (2003), p. 3724.
- [90] Martin Ams et al. “Slit beam shaping method for femtosecond laser direct-write fabrication of symmetric waveguides in bulk glasses”. In: *Optics express* 13.15 (2005), p. 5676.
- [91] Robert R Thomson et al. “Shaping ultrafast laser inscribed optical waveguides using a deformable mirror”. In: *Optics express* 16.17 (2008), pp. 12786–12793.
- [92] Yasuhiko Shimotsuma et al. “Self-organized nanogratings in glass irradiated by ultrashort light pulses”. In: *Physical review letters* 91.24 (2003), p. 247405.
- [93] PG Kazansky et al. “Anomalous anisotropic light scattering in Ge-doped silica glass”. In: *Physical Review Letters* 82.10 (1999), p. 2199.
- [94] Felix Zimmermann et al. “The onset of ultrashort pulse-induced nanogratings”. In: *Laser & Photonics Reviews* 10.2 (2016), p. 327.

BIBLIOGRAPHY

- [95] V Bhardwaj et al. “Optically produced arrays of planar nanostructures inside fused silica”. In: *Physical review letters* 96.5 (2006), p. 057404.
- [96] R Taylor, C Hnatovsky, and E Simova. “Applications of femtosecond laser induced self-organized planar nanocracks inside fused silica glass”. In: *Laser & Photonics Reviews* 2.1-2 (2008), p. 26.
- [97] S Richter et al. “Formation of femtosecond laser-induced nanogratings at high repetition rates”. In: *Applied Physics A* 104.2 (2011), p. 503.
- [98] Anton Rudenko et al. “Spontaneous periodic ordering on the surface and in the bulk of dielectrics irradiated by ultrafast laser: a shared electromagnetic origin”. In: *Scientific reports* 7.1 (2017), pp. 1–14.
- [99] M Lancry et al. “Nanogratings and molecular oxygen formation during femtosecond laser irradiation in silica”. In: *Conference on Lasers and Electro-Optics/Pacific Rim*. Optical Society of America. 2011, p. C229.
- [100] Sören Richter et al. “Nanogratings in fused silica: Formation, control, and applications”. In: *Journal of Laser Applications* 24.4 (2012), p. 042008.
- [101] Weijia Yang et al. “Self-assembled periodic sub-wavelength structures by femtosecond laser direct writing”. In: *Optics Express* 14.21 (2006), p. 10117.
- [102] Lourdes Patricia R Ramirez et al. “Tuning the structural properties of femtosecond-laser-induced nanogratings”. In: *Applied Physics A* 100.1 (2010), p. 1.
- [103] Felix Zimmermann. “Ultrashort pulse induced nanostructures in transparent materials”. PhD thesis. Friedrich Schiller University Jena, 2017.
- [104] Jianzhao Li et al. “Nanograting Bragg responses of femtosecond laser written optical waveguides in fused silica glass”. In: *Optical Materials Express* 2.11 (2012), p. 1562.
- [105] Wenqiang Wan et al. “Efficient fabrication method of nano-grating for 3D holographic display with full parallax views”. In: *Optics express* 24.6 (2016), p. 6203.
- [106] Jiafeng Lu et al. “Fiber nanogratings induced by femtosecond pulse laser direct writing for in-line polarizer”. In: *Nanoscale* 11.3 (2019), p. 908.
- [107] Valeria Maselli et al. “Femtosecond laser written optofluidic sensor: Bragg grating waveguide evanescent probing of microfluidic channel”. In: *Optics Express* 17.14 (2009), p. 11719.
- [108] Patrick J Coles et al. “Quantum algorithm implementations for beginners”. In: *arXiv preprint arXiv:1804.03719* (2018).
- [109] David Deutsch. “Quantum theory, the Church–Turing principle and the universal quantum computer”. In: *Proceedings of the Royal Society of London. A. Mathematical and Physical Sciences* 400.1818 (1985), p. 97.
- [110] J O’Brien, A Furusawa, and J Vučković. “Photonic quantum technologies”. In: *Nature Photonics* 3.12 (2009), p. 687.
- [111] Michael A Nielsen and Isaac L Chuang. *Quantum Computation and Quantum Information*. Cambridge University Press, 2010.
- [112] J Dodd, T Ralph, and G Milburn. “Experimental requirements for Grover’s algorithm in optical quantum computation”. In: *Physical Review A* 68.4 (2003), p. 042328.
- [113] P Boykin et al. “On universal and fault-tolerant quantum computing”. In: *arXiv preprint quant-ph/9906054* (1999).

- [114] Stefanie Barz. “Quantum computing with photons: introduction to the circuit model, the one-way quantum computer, and the fundamental principles of photonic experiments”. In: *Journal of Physics B: Atomic, Molecular and Optical Physics* 48.8 (2015), p. 083001.
- [115] Werner Martienssen and Hans Warlimont. *Springer handbook of condensed matter and materials data*. Springer Science & Business Media, 2006.
- [116] Jerneja Pavlin, Nataša Vaupotič, and Mojca Čepič. “Liquid crystals: a new topic in physics for undergraduates”. In: *European journal of physics* 34.3 (2013), p. 745.
- [117] K Hiltrop. “Lyotropic liquid crystals”. In: *Liquid Crystals*. Springer, 1994, pp. 143–171.
- [118] Louis A Madsen et al. “Thermotropic biaxial nematic liquid crystals”. In: *Physical review letters* 92.14 (2004), p. 145505.
- [119] H. Zeng. “Light Driven Microscopic Robot”. PhD thesis. Mar. 2015.
- [120] Birendra Bahadur. “Liquid crystal displays”. In: *Molecular Crystals and Liquid Crystals* 109.1 (1984), pp. 3–93.
- [121] Pochi Yeh and Claire Gu. *Optics of liquid crystal displays*. Vol. 67. John Wiley & Sons, 2009.
- [122] Birendra Bahadur. *Liquid crystals: applications and uses*. Vol. 1. World scientific, 1990.
- [123] Denis Andrienko. “Introduction to liquid crystals”. In: *Journal of Molecular Liquids* 267 (2018), pp. 520–541.
- [124] Lesley Parry Jones. “Alignment Properties of Liquid Crystals.” In: *Handbook of Visual Display Technology* 3 (2012), pp. 1387–1402.
- [125] J Stöhr and MG Samant. “Liquid crystal alignment by rubbed polymer surfaces: a microscopic bond orientation model”. In: *Journal of electron spectroscopy and related phenomena* 98 (1999), pp. 189–207.
- [126] Deng-Ke Yang. *Fundamentals of liquid crystal devices*. John Wiley & Sons, 2014.
- [127] Young-Ki Kim et al. “Surface alignment, anchoring transitions, optical properties, and topological defects in the thermotropic nematic phase of organo-siloxane tetrapodes”. In: *Soft Matter* 10.3 (2014), pp. 500–509.
- [128] Frederic J Kahn. “Orientation of liquid crystals by surface coupling agents”. In: *Applied Physics Letters* 22.8 (1973), pp. 386–388.
- [129] V Reiffenrath et al. “New liquid-crystalline compounds with negative dielectric anisotropy”. In: *Liquid Crystals* 5.1 (1989), pp. 159–170.
- [130] Dietrich Demus et al. *Handbook of liquid crystals, volume 2A: low molecular weight liquid crystals I: calamitic liquid crystals*. John Wiley & Sons, 2011.
- [131] Hai-Wei Chen et al. “Liquid crystal display and organic light-emitting diode display: present status and future perspectives”. In: *Light: Science & Applications* 7.3 (2018), pp. 17168–17168.
- [132] VYoshio Koike VKenji Okamoto. “Super high quality MVA-TFT liquid crystal displays”. In: *Fujitsu Sci. Tech. J* 35.2 (1999), pp. 221–228.
- [133] Rolf R Hainich and Oliver Bimber. *Displays: fundamentals & applications*. AK Peters/CRC Press, 2016.
- [134] Zichen Zhang, Zheng You, and Daping Chu. “Fundamentals of phase-only liquid crystal on silicon (LCOS) devices”. In: *Light: Science & Applications* 3.10 (2014), e213–e213.

BIBLIOGRAPHY

- [135] Rujia Li and Liangcai Cao. “Progress in phase calibration for liquid crystal spatial light modulators”. In: *Applied Sciences* 9.10 (2019), p. 2012.
- [136] Iam-Choon Khoo. *Liquid crystals*. Vol. 64. John Wiley & Sons, 2007.
- [137] Lev Mikhailovich Blinov and Vladimir G Chigrinov. *Electrooptic effects in liquid crystal materials*. Springer Science & Business Media, 1996.
- [138] Synthron Chemicals. *Webkatalog*. <https://www.synthron-chemicals.com/Webkatalog.pdf>. Online; retrieved July 25, 2019.
- [139] Ming Gao, Liran Ma, and Jianbin Luo. “Effect of alkyl chain length on the orientational behavior of liquid crystals nano-film”. In: *Tribology Letters* 62.2 (2016), p. 24.
- [140] B Jérme, A Bosseboeuf, and P Pieranski. “Anchoring of nematic liquid crystals on terraced silicon surfaces”. In: *Physical Review A* 42.10 (1990), p. 6032.
- [141] Giuseppe Della Valle, Roberto Osellame, and Paolo Laporta. “Micromachining of photonic devices by femtosecond laser pulses”. In: *Journal of Optics A: Pure and Applied Optics* 11.1 (2008), p. 013001.
- [142] Martin Ams et al. “Ultrafast laser written active devices”. In: *Laser & Photonics Reviews* 3.6 (2009), pp. 535–544.
- [143] Graham D Marshall et al. “Laser written waveguide photonic quantum circuits”. In: *Optics express* 17.15 (2009), p. 12546.
- [144] Thomas Meany et al. “Engineering integrated photonics for heralded quantum gates”. In: *Scientific reports* 6.1 (2016), p. 1.
- [145] Qian Zhang et al. “Femtosecond laser direct writing of an integrated path-encoded CNOT quantum gate”. In: *Optical Materials Express* 9.5 (2019), p. 2318.
- [146] Chao-Yang Lu et al. “Experimental quantum coding against qubit loss error”. In: *Proceedings of the National Academy of Sciences* 105.32 (2008), p. 11050.
- [147] Luís A Fernandes et al. “Femtosecond laser writing of waveguide retarders in fused silica for polarization control in optical circuits”. In: *Optics express* 19.19 (2011), pp. 18294–18301.
- [148] Luís A Fernandes et al. “Stress induced birefringence tuning in femtosecond laser fabricated waveguides in fused silica”. In: *Optics express* 20.22 (2012), pp. 24103–24114.
- [149] Andrea Crespi et al. “Integrated photonic quantum gates for polarization qubits”. In: *Nature communications* 2.1 (2011), p. 1.
- [150] Jonas Zeuner et al. “Integrated-optics heralded controlled-NOT gate for polarization-encoded qubits”. In: *npj Quantum Information* 4.1 (2018), p. 1.
- [151] Giacomo Corrielli et al. “Rotated waveplates in integrated waveguide optics”. In: *Nature communications* 5.1 (2014), p. 1.
- [152] René Heilmann et al. “Arbitrary photonic wave plate operations on chip: Realizing Hadamard, Pauli-X, and rotation gates for polarisation qubits”. In: *Scientific reports* 4 (2014), p. 4118.
- [153] Fulvio Flamini et al. “Thermally reconfigurable quantum photonic circuits at telecom wavelength by femtosecond laser micromachining”. In: *Light: Science & Applications* 4.11 (2015), e354–e354.
- [154] Zachary Chaboyer et al. “Tunable quantum interference in a 3D integrated circuit”. In: *Scientific reports* 5.1 (2015), pp. 1–5.
- [155] IV Dyakonov et al. “Reconfigurable photonics on a glass chip”. In: *Physical Review Applied* 10.4 (2018), p. 044048.

BIBLIOGRAPHY

- [156] Francesco Ceccarelli et al. “Thermal Phase Shifters for Femtosecond Laser Written Photonic Integrated Circuits”. In: *Journal of Lightwave Technology* 37.17 (2019), pp. 4275–4281.
- [157] Panagiotis Vergyris et al. “On-chip generation of heralded photon-number states”. In: *Scientific reports* 6.1 (2016), pp. 1–6.
- [158] Zachary Chaboyer et al. “Design and fabrication of reconfigurable laser-written waveguide circuits”. In: *Optics Express* 25.26 (2017), pp. 33056–33065.
- [159] Francesco Ceccarelli et al. “Femtosecond Laser Writing: Low Power Reconfigurability and Reduced Crosstalk in Integrated Photonic Circuits Fabricated by Femtosecond Laser Micromachining”. In: *Laser & Photonics Reviews* 14.10 (2020), p. 2070056.
- [160] Sebabrata Mukherjee and Mikael C Rechtsman. “Observation of Floquet solitons in a topological bandgap”. In: *Science* 368.6493 (2020), pp. 856–859.
- [161] Lukas J Maczewsky et al. “Nonlinearity-induced photonic topological insulator”. In: *Science* 370.6517 (2020), pp. 701–704.
- [162] Linda Sansoni et al. “Polarization entangled state measurement on a chip”. In: *Physical review letters* 105.20 (2010), p. 200503.
- [163] Erica Bricchi, Bruce G Klappauf, and Peter G Kazansky. “Form birefringence and negative index change created by femtosecond direct writing in transparent materials”. In: *Optics letters* 29.1 (2004), p. 119.
- [164] G Cheng et al. “Ultrafast laser photoinscription of polarization sensitive devices in bulk silica glass”. In: *Optics express* 17.12 (2009), p. 9515.
- [165] Cyril Hnatovsky et al. “Fabrication of microchannels in glass using focused femtosecond laser radiation and selective chemical etching”. In: *Applied Physics A* 84.1-2 (2006), p. 47.
- [166] Simone Piacentini et al. “Space Qualification of Ultrafast Laser-Written Integrated Waveguide Optics”. In: *Laser & Photonics Reviews* 15.2 (2021), p. 2000167.
- [167] Thomas Allsop et al. “Inscription and characterization of waveguides written into borosilicate glass by a high-repetition-rate femtosecond laser at 800 nm”. In: *Applied optics* 49.10 (2010), pp. 1938–1950.
- [168] Yusuke Nasu, Masaki Kohtoku, and Yoshinori Hibino. “Low-loss waveguides written with a femtosecond laser for flexible interconnection in a planar light-wave circuit”. In: *Optics letters* 30.7 (2005), pp. 723–725.
- [169] Jun Guan et al. “Hybrid laser written waveguides in fused silica for low loss and polarization independence”. In: *Optics express* 25.5 (2017), pp. 4845–4859.
- [170] Takeshi Fukuda et al. “Improvement on asymmetry of low-loss waveguides written in pure silica glass by femtosecond laser pulses”. In: *Optical Fibers and Passive Components*. Vol. 5279. International Society for Optics and Photonics. 2004, pp. 21–28.
- [171] Giacomo Corrielli et al. “Symmetric polarization-insensitive directional couplers fabricated by femtosecond laser writing”. In: *Optics express* 26.12 (2018), pp. 15101–15109.
- [172] Ian H Malitson. “Interspecimen comparison of the refractive index of fused silica”. In: *Josa* 55.10 (1965), pp. 1205–1209.
- [173] Philip E Ciddor. “Refractive index of air: new equations for the visible and near infrared”. In: *Applied optics* 35.9 (1996), pp. 1566–1573.

BIBLIOGRAPHY

- [174] Somenath Sarkar, K Thyagarajan, and Arun Kumar. “Gaussian approximation of the fundamental mode in single mode elliptic core fibers”. In: *Optics communications* 49.3 (1984), pp. 178–183.
- [175] Eugene Hecht. *Optics*. Pearson Education, Inc., 2017.
- [176] Robert W Boyd, Svetlana G Lukishova, and Yuen Ron Shen. *Self-focusing: Past and Present: Fundamentals and Prospects*. Vol. 114. Springer Science & Business Media, 2008.
- [177] M Ams, GD Marshall, and MJ Withford. “Study of the influence of femtosecond laser polarisation on direct writing of waveguides”. In: *Optics Express* 14.26 (2006), pp. 13158–13163.
- [178] George Smith, Smith George, and David A Atchison. *THE EYE AND VISUAL OPTICAL INSTRUMENTS. Edition en anglais*. Cambridge University Press, 1997.
- [179] Jürgen Eichler, Lothar Dünkel, and Bernd Eppich. “Die Strahlqualitaet von Lasern–Wie bestimmt man Beugungsmasszahl und Strahldurchmesser in der Praxis?” In: *Laser Technik Journal* 1.2 (2004), pp. 63–66.
- [180] Xiao Jia and Xin Zhao. “Thermal accumulation at kilohertz repetition rates inside fused silica under ultrafast laser irradiation”. In: *Optics Letters* 45.13 (2020), pp. 3390–3393.
- [181] I Mansour and F Caccavale. “An improved procedure to calculate the refractive index profile from the measured near-field intensity”. In: *Journal of lightwave technology* 14.3 (1996), pp. 423–428.
- [182] David J Lockwood. “Rayleigh and Mie scattering”. In: *Encyclopedia of Color Science and Technology*, Springer, New York, NY (2016), pp. 1–12.
- [183] Raphaela Weiß et al. “Rayleigh–Mie scattering ellipsometry as an in situ diagnostic for the production of “smart nanoparticles””. In: *physica status solidi (a)* 205.4 (2008), pp. 802–805.
- [184] F Zimmermann et al. “Structural evolution of nanopores and cracks as fundamental constituents of ultrashort pulse-induced nanogratings”. In: *Applied Physics A* 114.1 (2014), pp. 75–79.
- [185] Valdemar Stankevič et al. “Laser printed nano-gratings: orientation and period peculiarities”. In: *Scientific reports* 7.1 (2017), pp. 1–8.
- [186] John H Burnett, Zachary H Levine, and Eric L Shirley. “Intrinsic birefringence in calcium fluoride and barium fluoride”. In: *Physical Review B* 64.24 (2001), p. 241102.
- [187] Marti Duocastella and Craig B Arnold. “Bessel and annular beams for materials processing”. In: *Laser & Photonics Reviews* 6.5 (2012), pp. 607–621.
- [188] Guodong Zhang et al. “Femtosecond laser Bessel beam welding of transparent to non-transparent materials with large focal-position tolerant zone”. In: *Optics express* 26.2 (2018), pp. 917–926.
- [189] Wu-Jung Tsai et al. “Internal modification for cutting transparent glass using femtosecond Bessel beams”. In: *Optical Engineering* 53.5 (2013), p. 051503.
- [190] M Jenne et al. “Glass cutting optimization with pump-probe microscopy and Bessel beam profiles”. In: *Frontiers in Ultrafast Optics: Biomedical, Scientific, and Industrial Applications XVIII*. Vol. 10522. International Society for Optics and Photonics. 2018, p. 1052216.

- [191] Ehsan Alimohammadian et al. “Inhibition and enhancement of linear and nonlinear optical effects by conical phase front shaping for femtosecond laser material processing”. In: *Scientific reports* 10.1 (2020), pp. 1–13.
- [192] Ehsan Alimohammadian et al. “Compensating deep focusing distortion for femtosecond laser inscription of low-loss optical waveguides”. In: *Optics Letters* 45.22 (2020), pp. 6306–6309.
- [193] Ehsan Alimohammadian et al. “Manipulating geometric and optical properties of laser-inscribed nanogratings with conical phase front”. submitted to *Optics Materials Express*.
- [194] Ander Biguri. *Perceptually uniform colormaps*. MATLAB Central File Exchange, <https://www.mathworks.com/matlabcentral/fileexchange/51986-perceptually-uniform-colormaps>. Online; accessed July 25, 2019. 2020.
- [195] Masaaki Sakakura et al. “Ultralow-loss geometric phase and polarization shaping by ultrafast laser writing in silica glass”. In: *Light: Science & Applications* 9.1 (2020), pp. 1–10.

Zusammenfassung

Polarisationskontrolle in photonischen Schaltkreisen leistet einen entscheidenden Beitrag, um möglichst viele Freiheitsgrade des Photons bei der Codierung von Informationen auszunutzen. Jeder zusätzlich verwendete Freiheitsgrad in der optischen Informationsübertragung erlaubt eine Erhöhung der Datenrate und somit einen schnelleren Datenfluss. Ziel dieser Arbeit war es, Polarisationskontrolle in femtosekundenlaser-geschriebenen Wellenleitern zu erreichen.

Die erste Voraussetzung hierfür sind doppelbrechungsarme und verlustarme Wellenleiter, die in dieser Arbeit durch geschickte Strahlformung erzielt werden konnten. Solche doppelbrechungsarmen Wellenleiter sind die Grundvoraussetzung für die polarisationscodierte Informationsübertragung. Zunächst wurde untersucht, wie weit sich Wellenleiter durch die Strahlformung mittels zylindrischem Teleskop verbessern ließen. Infolge dessen wurde die Strahlformung weiter optimiert, indem zum ersten Mal ein anamorphotisches Zoom-System für die Wellenleitererzeugung eingesetzt wurde, das eine variable Einstellung der Strahlelliptizität ermöglichte. Die besten Wellenleitereigenschaften im Sinne von geringen Verlusten bei geringer Doppelbrechung wurden mit dem anamorphotischen Zoom-System erzielt. So konnten Wellenleiter erzielt werden, deren Verluste nahe an die bisher niedrigsten veröffentlichten Verluste kommen, bei gleichzeitig deutlicher Reduktion der typischen Wellenleiter-Doppelbrechung.

Der zweite Aspekt der Polarisationskontrolle ist das gezielte Einbetten doppelbrechender Strukturen in die Wellenleiter. Hierzu wurden im Rahmen dieser Arbeit zwei innovative Ansätze vorgestellt, einerseits basierend auf femtosekundenlaser-geschriebenen Nanogittern, und andererseits basierend auf schaltbaren Flüssigkristallen. Die Verwendung von Nanogittern als Verzögerungselemente erfordert die präzise Kontrolle über den Winkel ihrer optischen Achse und die Stärke ihrer linearen optischen Verzögerung, was durch die gezielte Wahl an Laserschreibparametern möglich ist. Im Rahmen dieser Studie wurde zudem der Einfluss der verschiedenen für die Wellenleitererzeugung verwendeten Strahlformungsansätze auf die Nanogitter untersucht. Die günstigsten Nanogittereigenschaften im Sinne von hoher Doppelbrechung bei geringen Verlusten wurden dabei durch das zylindrische Teleskop erreicht, welches daraufhin für die Kombination von Wellenleitern mit Nanogittern verwendet

wurde. Auf diese Weise konnten zum ersten Mal Quantengatter aus Nanogittern erzeugt und mittels Einzelphotonen charakterisiert werden. Sie wiesen Fidelitäten von größer-gleich 0.93 auf. Der entscheidende Punkt, um hierbei alle Freiheitsgrade der Nanogitter ausnutzen zu können, ist eine Einschreibrichtung der Nanogitter senkrecht zur Einschreibrichtung der Wellenleiter. Im Vergleich zu bisherigen Ansätzen für polarisationscodierte Einzelqubitquantengatter in lasergeschriebenen Glaswellenleitern stechen die so erzeugten Quantengatter durch ihre um zwei Größenordnungen verbesserte Kompaktheit hervor. Dies ist ein wichtiger Schritt in Richtung Miniaturisierung glasbasierter, integrierter photonischer Quantenschaltkreise.

Weiterhin wurde in dieser Arbeit erstmalig untersucht, wie sich Strahlformung mit konischen Phasenfronten auf die Eigenschaften von Nanogittern auswirkt. Durch die Veränderung des Winkels der konischen Phasenfront konnte die Einschreibtiefe der Modifikation ohne Bewegung der Probe oder der Einschreiblinse verändert werden. Außerdem hatte die Veränderung des konischen Phasenfrontwinkels einen erheblichen Einfluss auf die optischen Eigenschaften, wie die optische Verzögerung der Strukturen, die Doppelbrechung, den Dichroismus und die Verluste. Dies ermöglicht eine deutliche Verbesserung der Nanogittereigenschaften für Anwendungen als Wellenplatten.

Desweiteren wurde in dieser Arbeit erstmals eine schaltbare Polarisationskontrolle in einem lasergeschriebenem Quarzglaswellenleiter demonstriert. Hierzu wurde eine dünne Schicht Flüssigkristalle in einen Wellenleiter eingebettet. Durch das Anlegen elektrischer Spannungen konnte die Ausrichtung der Flüssigkristalle so weit manipuliert werden, dass mehrere vollständige Drehungen der Ausgangspolarisation des Wellenleiters auf der Poincaré-Sphäre erreicht wurden.

Zusammenfassend ist festzuhalten, dass die Polarisationskontrolle in femtosekundenlaser-direktgeschriebenen Schaltkreisen in dieser Arbeit in zwei wesentlichen Aspekten weiterentwickelt und optimiert wurde. Der erste Aspekt ist die Erzeugung von niedrigdoppelbrechenden Wellenleitern, die durch einen verbesserten Strahlformungs-Ansatz ermöglicht wurde. Der zweite Aspekt sind neue Ansätze, um gezielt Verzögerungselemente in die Wellenleiter einzubringen, bestehend aus Nanogittern und Flüssigkristallen. Die hier vorgestellten Ansätze und Einschreibmethoden tragen zukunftsweisend dazu bei, photonische Schaltkreise, in denen polarisationskodiert Information übertragen wird, kompakter und zudem dynamisch schaltbar zu gestalten. Die Ergebnisse haben eine hohe Relevanz für eine Vielzahl von Anwendungen, wie zum Beispiel Augmented Reality, den optischen Computer oder die optische Datenübertragung.

Ehrenwörtliche Erklärung

Ich erkläre hiermit ehrenwörtlich, dass ich die vorliegende Arbeit selbständig und ohne unzulässige Hilfe Dritter sowie ohne Benutzung anderer als der angegebenen Hilfsmittel und Literatur angefertigt habe. Es wurden insbesondere keine Textabschnitte eines Dritten oder eigene Prüfungsarbeiten ohne Kennzeichnung übernommen. Alle benutzten Hilfsmittel, persönliche Mitteilungen und Quellen wurden angegeben. Die aus anderen Quellen direkt oder indirekt übernommenen Daten und Konzepte sind unter Angabe der Quellen gekennzeichnet.

Bei der Auswahl und Auswertung des vorliegenden Materials haben mir die nachstehend aufgeführten Personen in der jeweils beschriebenen Weise unentgeltlich geholfen:

- Die Glasproben in dieser Arbeit wurden von Christiane Otto am Institut für Angewandte Physik Jena geschnitten und poliert. Alle laser-geschriebenen Strukturen, die für die REM-Aufnahme an die Oberfläche gebracht werden mussten, sind von ihr freigelegt worden.
- Prof. Herbert Gross vom Institut für Angewandte Physik Jena hat das in Abschnitt 4.3 beschriebene anamorphotische Zoom-System entworfen.
- Detlef Schelle vom Institut für Angewandte Physik Jena hat die REM-Bilder in Abbildung 5.1 aufgenommen.
- Die Einzelphotonencharakterisierung aus Abschnitt 5.3 wurde in Zusammenarbeit mit Max Ehrhardt durchgeführt, der den Großteil des Aufbaus zur Charakterisieren mit Einzelphotonen vorbereitet hat (Abbildung 5.13) und basierend auf den Einzelphotonenmessungen die Quantenmatrizen rekonstruiert hat.
- Die durch Strahlen mit konischen Phasenwinkeln erzeugten Nanogitter in Abschnitt 5.4 sind von Dr. Ehsan Alimohammadian von der Universität Toronto unter der Leitung von Prof. Herman erzeugt worden.
- Yuliya Shyk von der EAH Jena hat das Ätzen der Proben in dieser Arbeit ausgeführt.
- Michael Steinert vom Institut für Angewandte Physik Jena hat die REM-Bilder in Abschnitt 5.4 aufgenommen, sowie die Proben durch Kohlenstoff-Beschichtung auf die Aufnahmen vorbereitet.

- Die Simulationen zur Einzelpulsausbreitung von Strahlen mit konischen Phasenwinkeln in Quarzglas, von denen die Ergebnisse qualitativ in Abschnitt 5.4.2 wiedergegeben wurden, wurden von Dr. Alessandro Alberucci durchgeführt und basieren auf einem Quellcode von Dr. Jisha Chandroth-Pannian.

Weitere Personen waren an der inhaltlich-materiellen Erstellung der vorliegenden Arbeit nicht beteiligt. Die Hilfe einer kommerziellen Promotionsvermittlerin/eines kommerziellen Promotionsvermittlers wurde nicht in Anspruch genommen. Niemand hat von mir unmittelbar oder mittelbar geldwerte Leistungen für Arbeiten erhalten, die im Zusammenhang mit dem Inhalt der vorgelegten Dissertation stehen.

Die Arbeit wurde bisher weder im In- noch im Ausland in gleicher oder ähnlicher Form als Prüfungsarbeit einer anderen Prüfungsbehörde vorgelegt. Teile dieser Arbeit wurden aus Prioritätsgründen bereits veröffentlicht bzw. zur Veröffentlichung eingereicht.

Die geltende Promotionsordnung der Physikalisch-Astronomischen Fakultät ist mir bekannt. Ich versichere ehrenwörtlich, dass ich nach bestem Wissen die reine Wahrheit gesagt und nichts verschwiegen habe.

List of publications and conference contributions

Publications (realized and planned):

- Bergner, et al., Applied optics 57.16 (2018): 4618.
- Matthäus, et al., Optics express 26.18 (2018): 24089.
- Kämmer, et al., Laser & Photonics Reviews 13.2 (2019): 1800268.
- Lammers, et al., Optical Materials Express 9.6 (2019): 2560.
- Alimohammadian, et al., Optics Express 30.4 (2022): 5360.
- Lammers, et al., (Hybridization of femtosecond-laser written waveguides with liquid crystals, in prep.)

Conferences & meetings:

- Lammers, et al. "Manipulating Polarization States in Waveguides for Quantum Computational Applications", DokDok 2017
- Matthäus, et al. "Femtosecond written buried waveguides in silicon", Photonics West 2018
- Nolte, et al. "Inscription of silicon waveguides using ultrashort laser pulses [10519-0K]", Workshop on Short Pulse Laser Solid Interaction 2018, Lyon
- Lammers, et al. "Embedded Nanogratings for polarization control in femtosecond laser direct written nanogratings", Photonics North 2018
- Matthäus, et al., "Inscription of silicon waveguides using ultrashort laser pulses [10908-26]", Photonics West 2019
- Lammers, et al., "Compact Femtosecond Laser Direct Written Integrated Retarders Based On Embedded Nanogratings", CLEO Munich 2019
- Lammers, et al., "Nanograting based birefringent retardation elements in integrated photonic circuits [11268-46]", Photonics West 2020
- Lammers, et al., "Liquid crystal based tuneable waveplates embedded in femtosecond laser direct written waveguides" EMRS Spring Meeting 2021
- Lammers, et al., "Using liquid crystals as tuneable waveplates in femtosecond laser direct written waveguides" CLEO Europe 2021
- Lammers, et al., "Optical Properties of Nanogratings Inscribed with Conical Phase Fronts" CLEO Europe 2021

Acknowledgements

I would like to thank all those who supported and motivated me during the preparation of this thesis. First of all, I would like to thank Prof. Stefan Nolte, who enabled me to do my PhD within the frameworks of the GRK 2101 and the Max Planck School of Photonics (MPSP). I would like to thank him for his time of mentoring, his supervision, his helpful suggestions, and his constructive criticism during the preparation of this thesis. Thank you, for trusting in my work and in my abilities. Thank you to Prof. Thomas Pertsch for agreeing to be part of my thesis advisory committee of the MPSP and offering helpful suggestions in the final phase of my PhD.

I would also like to thank my colleagues, especially my lab and office mates Dr. Alessandro Alberucci, Dr. Qingfeng Li and Dr. Jisha Chandroth-Pannian, who supported me with a lot of interest and helpfulness. Thank you for all your feedback, suggestions and advice. Many thanks to all members of the Ultrafast Optics Group at the Institute of Applied Physics Jena for the numerous interesting debates and ideas, which have contributed significantly to the fact that this thesis is available in this form. Many thanks to Mrs. Otto for her outstanding glass preparation and to Detlef Schelle and Yuliya Shyk for etching my samples. Many thanks to Michael Steinert for the pleasant and constructive SEM sessions.

Furthermore, I would like to thank Prof. Herbert Gross for the good collaboration and the design of the anamorphic zoom system. It has been a pleasure working with you. Many thanks to Prof. Alexander Szameit and Max Ehrhardt for enabling the single photon characterizations of the nanograting-waveguide combinations. Many thanks for the pleasant cooperation and the friendly reception in Rostock. Thanks also to Prof. Herman and Dr. Ehsan Alimohammadian for trustingly turning to me to evaluate their nanogratings. Thank you for this opportunity to work together. Thank you for Prof. Réal Vallée and Dr. Jean-Phillippe Bérubé for the invitation to COPL Quebec and the support during my research stay there. Finally, I would like to thank my husband for your unlimited support in all circumstances, for covering my back in all these years. Thank you to my parents, who made my studies possible and are always ready to lend an ear.